



UNIVERSITY OF ILLINOIS
URBANA

AERONOMY REPORT NO. 77

A ROCKET-BORNE AIRGLOW PHOTOMETER

{NASA-CR-155327} A ROCKET-BORNE AIRGLOW PHOTOMETER {Illinois Univ.} 161 p HC A08/MF
A01 CSCI 04A

N78-12585

Unclas
G3/46 53571

by
L. D. Paarmann
L. G. Smith

May 1, 1977

Library of Congress ISSN 0568-0581



Supported by
National Aeronautics and Space Administration
Grant NGR 14-005-181

Aeronomy Laboratory
Department of Electrical Engineering
University of Illinois
Urbana, Illinois

CITATION POLICY

The material contained in this report is preliminary information circulated rapidly in the interest of prompt interchange of scientific information and may be later revised on publication in accepted aeronomic journals. It would therefore be appreciated if persons wishing to cite work contained herein would first contact the authors to ascertain if the relevant material is part of a paper published or in process.

A E R O N O M Y R E P O R T
N O. 77

A ROCKET-BORNE AIRGLOW PHOTOMETER

by
L. D. Paarmann
L. G. Smith

May 1, 1977

Supported by
National Aeronautics and
Space Administration
Grant NGR 14-005-181

Aeronomy Laboratory
Department of Electrical Engineering
University of Illinois
Urbana, Illinois

ABSTRACT

This paper presents the design of a rocket-borne photometer to measure the airglow emission of ionized molecular nitrogen in the 391.4 nm band. This airglow is a well-known and often observed phenomenon of auroras, where the principal source of ionization is energetic electrons. It is believed that at some midlatitude locations energetic electrons are also a source of nighttime ionization in the E region of the ionosphere. If this is so, then significant levels of 391.4 nm airglow should be present. The intensity of this airglow will be measured in a rocket payload which also contains instrumentation to measure energetic electron differential flux and the ambient electron density. An intercomparison of the three experiments in a nighttime launch from Wallops Island will allow a test of the importance of energetic electrons as a nighttime source of ionization in the upper E region.

PRECEDING PAGE BLANK NOT FILMED

TABLE OF CONTENTS

ABSTRACT	iii
TABLE OF CONTENTS.	v
LIST OF TABLES	viii
LIST OF FIGURES.	ix
1. INTRODUCTION	1
2. AIRGLOW AND PHOTOMETRY	6
2.1 <i>Nighttime Airglow at 391.4 nm and its Excitation.</i>	6
2.1.1 <i>Height distribution.</i>	6
2.1.2 <i>Photon sources of ionization</i>	6
2.1.3 <i>Energetic charged particle sources of ionization</i> . . .	8
2.1.4 <i>Spectral characteristics</i>	10
2.1.5 <i>Intensity variations</i>	10
2.2 <i>Problems Associated with the Measurements</i>	12
2.2.1 <i>Other ionization sources</i>	12
2.2.2 <i>Vibrational and rotational temperatures</i>	12
2.2.3 <i>Extraterrestrial light</i>	13
2.2.4 <i>Other airglows</i>	13
2.3 <i>Rocket Photometry</i>	17
2.4 <i>Technological Advances in Photometry.</i>	19
3. GENERAL DESCRIPTION.	21
3.1 <i>Detector.</i>	21
3.2 <i>Pulse Preamplifier.</i>	25
3.3 <i>Pulse Processor</i>	26
3.4 <i>Temperature Monitors and System Check</i>	27
3.5 <i>Rocket-borne Instrumentation System</i>	30
3.6 <i>Ground-based Instrumentation Systems.</i>	33

4.	DETECTOR	38
4.1	<i>Channel Multiplier.</i>	38
4.1.1	<i>Selection considerations</i>	38
4.1.2	<i>The multiplier and accompanying high voltage power supply</i>	40
4.2	<i>Optical Filter.</i>	46
4.2.1	<i>Theoretical introduction</i>	46
4.2.2	<i>Determination of specifications.</i>	57
4.3	<i>Lens.</i>	63
4.4	<i>Window.</i>	65
4.5	<i>Detector Assembly</i>	65
4.6	<i>Adjustments</i>	71
5.	ELECTRONIC CIRCUITS.	72
5.1	<i>Detector Electronics.</i>	72
5.2	<i>Pulse Preamplifier.</i>	75
5.2.1	<i>Circuit description.</i>	75
5.2.2	<i>Characteristics.</i>	78
5.3	<i>Pulse Processor</i>	83
5.3.1	<i>Circuit description.</i>	83
5.3.2	<i>Characteristics.</i>	85
5.4	<i>Temperature Monitors.</i>	89
5.4.1	<i>Monitor electronics.</i>	89
5.4.2	<i>Calibration.</i>	93
5.5	<i>Other Circuits.</i>	98
5.5.1	<i>Low-voltage regulators</i>	98
5.5.2	<i>System check</i>	98
5.5.3	<i>Instrument interconnections</i>	104

5.6	<i>Adjustments</i>	104
5.6.1	<i>Negative converter</i>	104
5.6.2	<i>High-voltage adjust.</i>	104
5.6.3	<i>Pulse preamplifier threshold adjust.</i>	107
6.	ANALYSIS OF INSTRUMENT SENSITIVITY	109
6.1	<i>Introduction.</i>	109
6.2	<i>Incident Radiation Independent of Layer Height.</i>	110
6.3	<i>Incident Radiation Dependent upon Angle with Respect to Zenith.</i>	115
6.4	<i>Channel Multiplier Input as a Function of Filter Temperature</i>	125
6.5	<i>Instrument Sensitivity.</i>	130
7.	SUGGESTIONS FOR FUTURE WORK.	133
	REFERENCES	136
	APPENDIX I. NIKE APACHE PAYLOAD VIBRATION AND SHOCK TESTS.	139
	APPENDIX II. COMPUTER PROGRAMS.	140
	II.1 FOLDING OF GAUSSIAN-WINDOW FILTERS WITH DISCRETE LINE SPECTRUM.	141
	II.2 FOLDING OF FILTER TRANSMISSION FUNCTIONS WITH DISCRETE LINE SPECTRUM AT VARIOUS TEMPERATURES	144
	II.3 ANALYSIS OF INCIDENT RADIATION DEPENDENCE UPON ANGLE WITH RESPECT TO ZENITH	148

LIST OF TABLES

Table		Page
4.1	Important Characteristics of the 521N-01-CM Channel Multiplier	41
4.2	Summary of Measured Characteristics of 521N-01-CM Channel Multipliers	42
4.3	Specifications of the Optical Filter	64
4.4	Important Characteristics of the Lens	66
4.5	Important Characteristics of the Window	67
5.1	Pulse Preamplifier Measured Characteristics	79
5.2	Pulse Preamplifier DC Measurements	81
5.3	Pulse Processor Measured Characteristics	87
5.4	Pulse Processor DC Measurements	88
5.5	Calibration Chart for Temperature Monitor Circuits (serial number 1 unit)	99
6.1	Incident Radiation as a Function of ψ	123

LIST OF FIGURES

Figure		Page
1.1	The photometer mounted in the payload of a Nike Apache rocket.	4
2.1	Geographic distribution of the observations of 100 keV electrons at altitudes between 240 and 410 km made by a low-altitude satellite [<i>Seward</i> , 1973]	9
2.2	Model of 391.4 nm spectrum excited by electron impact at several vibrational and rotational temperatures, and smoothed by a 4 Å triangular halfwidth. For each curve, the vibrational temperature equals the rotational temperature [<i>V. Degen</i> , University of Alaska, private communication].	11
2.3	Measured night sky spectrum in the range 3050 Å to 3980 Å. Below, the locations of Herzberg bands of the O ₂ molecule for the given vibrational level transitions [<i>Krassovsky et al.</i> , 1962]	14
2.4	The photometer mounted in the frame of the rocket payload	18
3.1	A side view of the photometer	22
3.2	Photometer block diagram.	23
3.3	Output #1 of Figure 3.2. Individual steps can be seen in the low count-rate waveform but not in the high count-rate waveform.	28
3.4	Rocket-borne instrumentation system block diagram	31
3.5	The photometer seen through the open door of the rocket payload	32

Figure	Page	
3.6	Ground-based instrumentation system block diagram, method 1.	34
3.7	Ground-based instrumentation system block diagram, method 2.	36
3.8	Ground-based instrumentation system block diagram, method 3.	37
4.1	The channel multiplier tube, potted on the left and unpotted on the right	43
4.2	Operation of a channel multiplier	45
4.3	Multiple internal reflections in a Fabry-Perot inter- ferometer or filter. The angle of incidence is nearly normal; it is exaggerated here for clarity.	48
4.4	The sharpness of Fabry-Perot filter transmission bands as a function of reflectance, R [<i>Lipson and Lipson, 1969</i>] .	50
4.5	Transmittance versus wavelength response of a dielectric layer bounded by two metallic reflecting layers (curve a). Curve b is the transmittance of an absorption filter used to suppress the shorter wavelength responses [<i>Barr &</i> <i>Stroud Ltd., in Macleod, 1969</i>]	51
4.6	A multilayer reflector.	53
4.7	A typical reflectance versus wavelength curve for a multilayer reflector [after <i>Macleod, 1969</i>].	54
4.8	A Fabry-Perot filter using all-dielectric multilayer reflectors.	55
4.9	A typical transmittance versus wavelength response of a Fabry-Perot filter using all-dielectric multilayer	

Figure	Page
	reflectors [<i>Gray</i> , 1957] 56
4.10	Gaussian-shaped filter transmission functions folded with the 1000 K discrete line spectrum. Filter peak transmittance = 1.0. Filter half-peak-transmittance bandwidth: V = 0.5 nm, W = 1.0 nm, X = 2.0 nm, Y = 3.0 nm, Z = 4.0 nm. 59
4.11	Optimum filter center wavelength versus bandwidth, and maximum possible total transmittance versus bandwidth . . . 60
4.12	Detector assembly 69
4.13	Optical assembly parts breakdown. 70
5.1	Detector electronics schematic diagram. 73
5.2	High-voltage power supply associated circuitry physical construction. 74
5.3	Rear view of the completed instrument 76
5.4	Pulse preamplifier schematic diagram. 77
5.5	Pulse preamplifier input and output waveforms: (a) input: 20 ns/cm; (b) output: 1 V/cm, 20 ns/cm (input: 500 mv); (c) output: 1 V/cm, 50 ns/cm (input: 5 mV); (d) output: 0.5 V/cm, 50 ns/cm (input: 1.25 mV) 80
5.6	Pulse preamplifier physical construction. 82
5.7	Pulse processor schematic diagram 84
5.8	Pulse processor output waveforms: (a) pulse output: 1 V/cm, 50 ns/cm; (b) staircase output: 1 V/cm, 0.2 ms/cm . 86
5.9	Pulse processor physical construction 90
5.10	Typical characteristics of the thermistor (Fenwal GB32P2) . 91
5.11	Temperature monitor schematic diagram 92

Figure	Page
5.12	Test set-up for calibrating the temperature monitors. 96
5.13	Thermistors-thermocouple assembly for calibrating the temperature monitors. 97
5.14	Calibration curve for filter temperature monitor (serial number 1 unit). 100
5.15	Calibration curve for frame temperature monitor (serial number 1 unit). 101
5.16	Low-voltage regulators schematic diagram. 102
5.17	System-check schematic diagram. 103
5.18	System-check staircase waveforms: (a) single trace, 1 V/cm, 0.2 ms/cm; (b) multiple traces, 1 V/cm; 0.2 ms/cm . 105
5.19	Instrument interconnections 106
5.20	Pulse preamplifier threshold adjustment set-up. 108
6.1	Geometry of the photometer directed normal to the emitting layer 111
6.2	The intersection of the angle-of-view cone and the emitting layer. 114
6.3	Look-angle of the photometer oblique to the emitting layer: two-dimensional geometry. 116
6.4	Look-angle of the photometer oblique to the emitting layer: three-dimensional geometry. 117
6.5	Illustration aiding the development of an expression for the center of the ellipse 119
6.6	Incident radiation as a function of ψ 124
6.7	An optical filter transmittance versus wavelength curve (graph of equation (6.12)). 127

Figure		Page
6.8	Convolution of equation (6.12) with discrete line spectra	129

1. INTRODUCTION

In February of 1962, astronaut John Glenn, inside a Mercury space capsule, rocketed from the earth's surface to an orbit approximately 130 miles high; the first U. S. manned orbital flight. During the flight, on the nightside of the earth, Glenn reported seeing a luminous layer above the horizon [*Glenn and O'Keefe*, 1962], which was later attributed to airglow.

In May of 1963, astronaut Gordon Cooper, while in orbit, took photographs of the airglow layer. Orbiting astronauts can easily see the layer (which is difficult to see from the surface) because they view it in profile from above; a gain in brightness of approximately 35 is realized, compared with viewing it vertically from below [*Gillett et al.*, 1964].

The above-mentioned observations of airglow were not the first. The phenomenon of airglow has been known for a long time; there are observations on record as early as 1788 of bright airglow at night. [*Chamberlain*, 1961].

Airglow also exists during the day, in fact it is generally brighter then, but is less visible due to the very bright radiation from the sun and its scattering in the atmosphere (which causes the sky to be blue).

The airglow discussed so far serves to indicate that, at least at night, it is observable with the human eye, can be photographed, and has been known for a long time. Airglow, however, is made up of many wavelengths and intensities, due to many different reactions taking place in the ionosphere. Many airglow wavelengths are invisible to the human eye, being outside the human eye response passband, and many

airglow wavelengths within the human eye passband are also invisible because the emissions are extremely weak.

Airglow is not the only source of light in the night sky. Other sources include zodiacal light (sunlight reflected from interplanetary dust), integrated starlight, and in the polar regions, aurora (which is essentially intense airglow). Background information on sources of light in the night sky, including airglow, is available in a number of references [Mitra, 1952; Bates, 1960; Chamberlain, 1961; Roach, 1964].

The airglow of interest here consists of a band of wavelengths with a bandhead at 391.4 nm, i.e., the peak emission rate in the band occurs at approximately 391.4 nm. This airglow is not observable by the human eye because the wavelengths are near ultraviolet, just outside the human eye response.

The emission in the 391.4 nm band is associated with the process of ionization of molecular nitrogen by energetic electrons. The N_2^+ is formed in excited states, which return to the ground state with the emission of radiation. It is estimated that radiation in the 391.4 nm band is produced at the rate of one photon for 50 ions formed [Whitten and Poppoff, 1971]. Thus a measurement of the intensity of the airglow at 391.4 nm can be interpreted as a measurement of ionization rate. Since ionization of N_2 requires about 35 eV of energy, the ionization rate can be used to estimate the rate of deposition of energy by the energetic electrons. The need for these measurements is due to the paucity of energetic electron flux information at midlatitudes. It is believed that energetic electrons are a significant source of nighttime midlatitude E-region ionization, and it is hoped that data received from this experiment will help substantiate that hypothesis. Direct energetic electron particle

measurements have been made on several occasions [*Smith, Geller and Voss, 1974; Voss and Smith, 1974; Smith and Voss, 1976*]; this airglow experiment provides an independent measurement of energetic electron flux.

The photometer is shown, in Figure 1.1, mounted in the payload of a Nike Apache rocket. The payload is 6.5 inches in diameter. The apogee of the rocket will be approximately 180 km.

In Chapter 2 airglow and photometry will be discussed. Background information on the nighttime airglow at 391.4 nm and its excitation is presented, together with some of the natural problems associated with its measurement. Then a brief discussion on rocket photometry is included in this chapter.

In Chapter 3 a general description of the operation of the photometer, as well as its use, is given. A basic understanding of the photometer is conveyed; the technical details are presented in later chapters. The chapter also presents a discussion of complete instrumentation systems, ground-based as well as rocket-borne, so that the use of the photometer is understood.

Chapter 4 presents the technical details of the photometer detector. Selection considerations and the theory of operation of the channel multiplier are presented. A rather detailed section on the theory of Fabry-Perot interference optical filters is included, as well as the determination of the desired specifications of such a filter. The other optical components are also discussed.

In Chapter 5 the technical details of the photometer electronic circuits are presented. These include the pulse preamplifier, the pulse processor, and the temperature monitors. Measured characteristics

ORIGINAL PAGE IS
OF POOR QUALITY

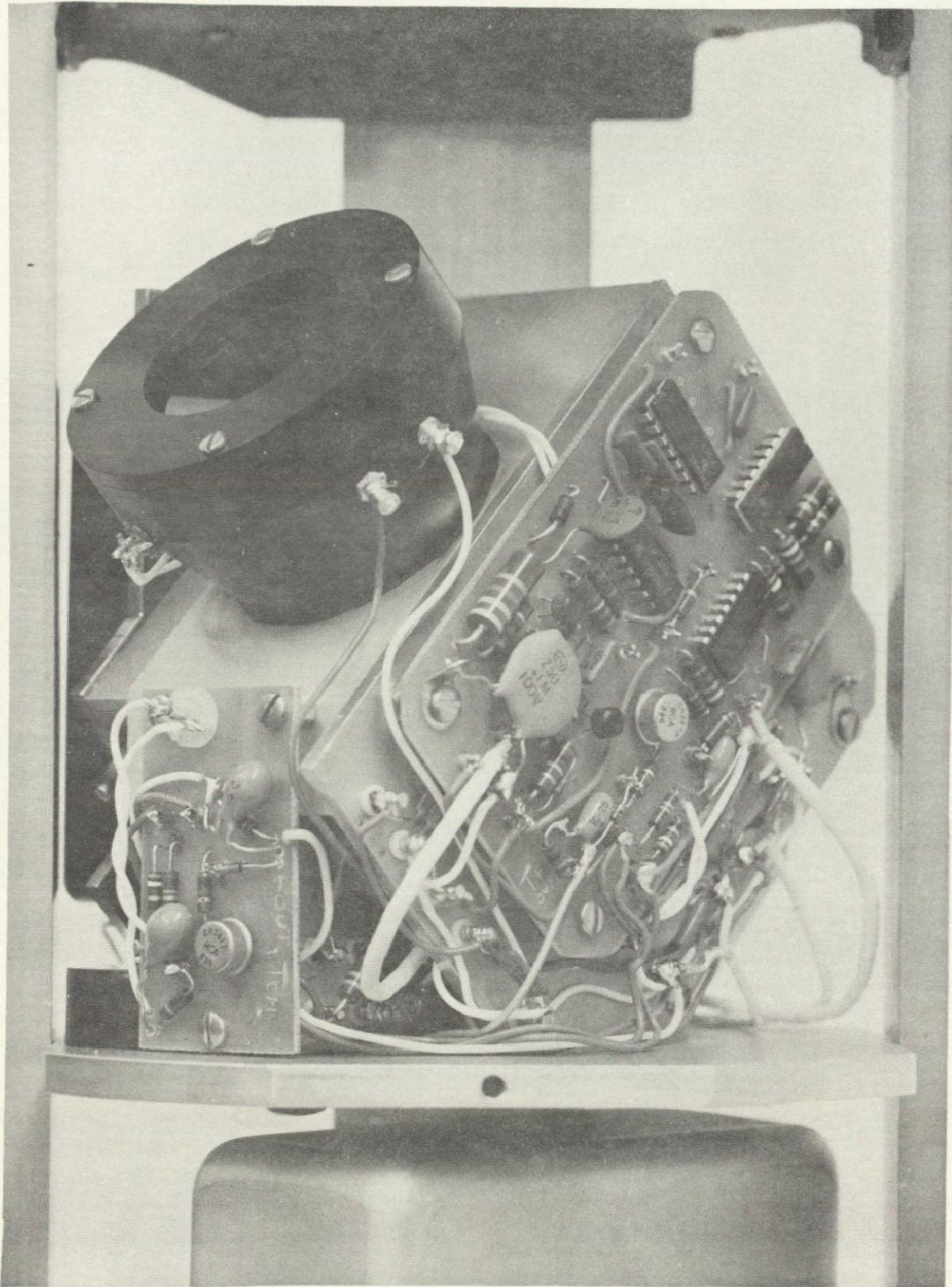


Figure 1.1 The photometer mounted in the payload of a Nike Apache rocket.

are given in addition to circuit descriptions. The calibration procedure for the temperature monitors is described; temperature calibration curves for the serial number 1 unit are included. Adjustment procedures are also given.

Chapter 6 presents an analysis of the instrument sensitivity, i.e., the theoretical output of the instrument is determined for a given 391.4 nm airglow emission rate.

The concluding chapter contains suggestions for future work. These include the calibration of the instrument using sources of known intensity.

2. AIRGLOW AND PHOTOMETRY

The purpose of this chapter is to provide background information to facilitate better understanding of a) general characteristics of nighttime midlatitude airglow at 391.4 nm, b) problems associated with its measurement, and c) basic concepts involved in photometric measurements.

2.1 *Nighttime Airglow at 391.4 nm and its Excitation*

2.1.1 *Height distribution.* Sources of ionization (energetic particles and photons) do not generally penetrate into the earth's atmosphere; very little ionization takes place near the earth's surface. At high altitudes the intensity of sources of ionization is greater but the density of N_2 is correspondingly smaller. Therefore a layer of N_2^+ is formed--high enough so that the sources of ionization are abundant, but low enough so that an adequate supply of N_2 is available. Some knowledge of the height distribution of N_2^+ during the daytime exists, for example see *Strobel et al.* [1970]. However, very little has been done to determine height distributions during the nighttime; an attempt was made by *O'Brien et al.* [1965].

2.1.2 *Photon sources of ionization.* Possible sources of ionization of molecular nitrogen can be grouped into two categories: photons and energetic charged particles. Photons will be considered in this section and energetic charged particles will be considered in the next.

The ionization potential of N_2 is 15.6 eV. The energy, in eV, of a photon is given by the following expression:

$$E = \frac{hc}{k\lambda}$$

where

$$h = \text{Planck's constant} = 6.6 \times 10^{-34} \text{ Js}$$

$$c = \text{speed of light} = 3 \times 10^8 \text{ m s}^{-1}$$

$$\lambda = \text{wavelength associated with the photon, in meters}$$

$$k = \text{electronic charge} = 1.6 \times 10^{-19} \text{ C}$$

From the above expression we observe that in order for a photon to have sufficient energy to ionize N_2 , the following inequality must be satisfied:

$$\lambda \leq 79.3 \text{ nm}$$

The major sources of photon flux in the nighttime E region at midlatitudes are Lyman α (121.6 nm) and Lyman β (102.6 nm). Lyman α and Lyman β result from the scattering of solar radiation by hydrogen in the geocorona. It has been suggested that Lyman α and Lyman β are the most important sources of ionization in the nighttime E region at midlatitudes [Fohmatsu, 1970; Swider, 1972; Strobel et al., 1974].

It may be noted that neither Lyman α nor Lyman β is capable of ionizing N_2 because the wavelengths are too long (Lyman α and Lyman β ionize NO and O_2 , respectively).

There are, however, two helium lines, caused by the scattering of solar radiation by helium in the geocorona, that are capable of ionizing molecular nitrogen: 58.4 nm and 30.4 nm. The photon flux of these two helium lines have been measured on several occasions and have been considered as a source of nighttime midlatitude E -region ionization [e.g., Strobel et al., 1974]. Since the total flux of these two lines does not amount to more than a few rayleighs (one rayleigh is an apparent column emission rate of $10^6 \text{ photons cm}^{-2} \text{ s}^{-1}$), it is

not believed that this is a significant source of ionization for N_2 .

Cosmic rays are another possible ionization source for N_2 . Calculations by *Potemra and Zmuda* [1972] indicate that ionization of N_2 due to this source, although present, is negligible.

Although X-rays and ultraviolet starlight are other possible photon sources of ionization of N_2 , they are not thought to be of any significance.

2.1.3 Energetic charged particle sources of ionization.

Energetic electrons have been considered as a source of midlatitude ionization [*Rees*, 1963; *Green and Stolarski*, 1966; *Potemra and Zmuda*, 1972; *Smith et al.*, 1974; *Voss and Smith*, 1974; *Geller et al.*, 1975; *Israelson and Winckler*, 1975; *Paulikas*, 1975; *Smith and Voss*, 1976]. Others argue that there is a sufficient flux of UV to account for the ionization in the nighttime *E* region at midlatitudes [*Tohmatsu*, 1970; *Swider*, 1972; *Strobel et al.*, 1974; *Young et al.*, 1975].

There is evidence that energetic electrons may be a major source of ionization at some midlatitude locations and not at others. Figure 2.1 shows the geographical distribution of the observations of 100 keV electrons at altitudes between 240 and 410 km made by a low-altitude satellite [*Seward*, 1973]. Note that a band of energetic electrons stretches east-west across the United States and directly over Wallops Island, Virginia, where the 391.4 nm airglow measurements are to be made. Also, evidence of high levels of energetic electron flux over Wallops Island has been found using rocket-borne instrumentation [*Smith et al.*, 1974; *Voss and Smith*, 1974; *Smith and Voss*, 1976].

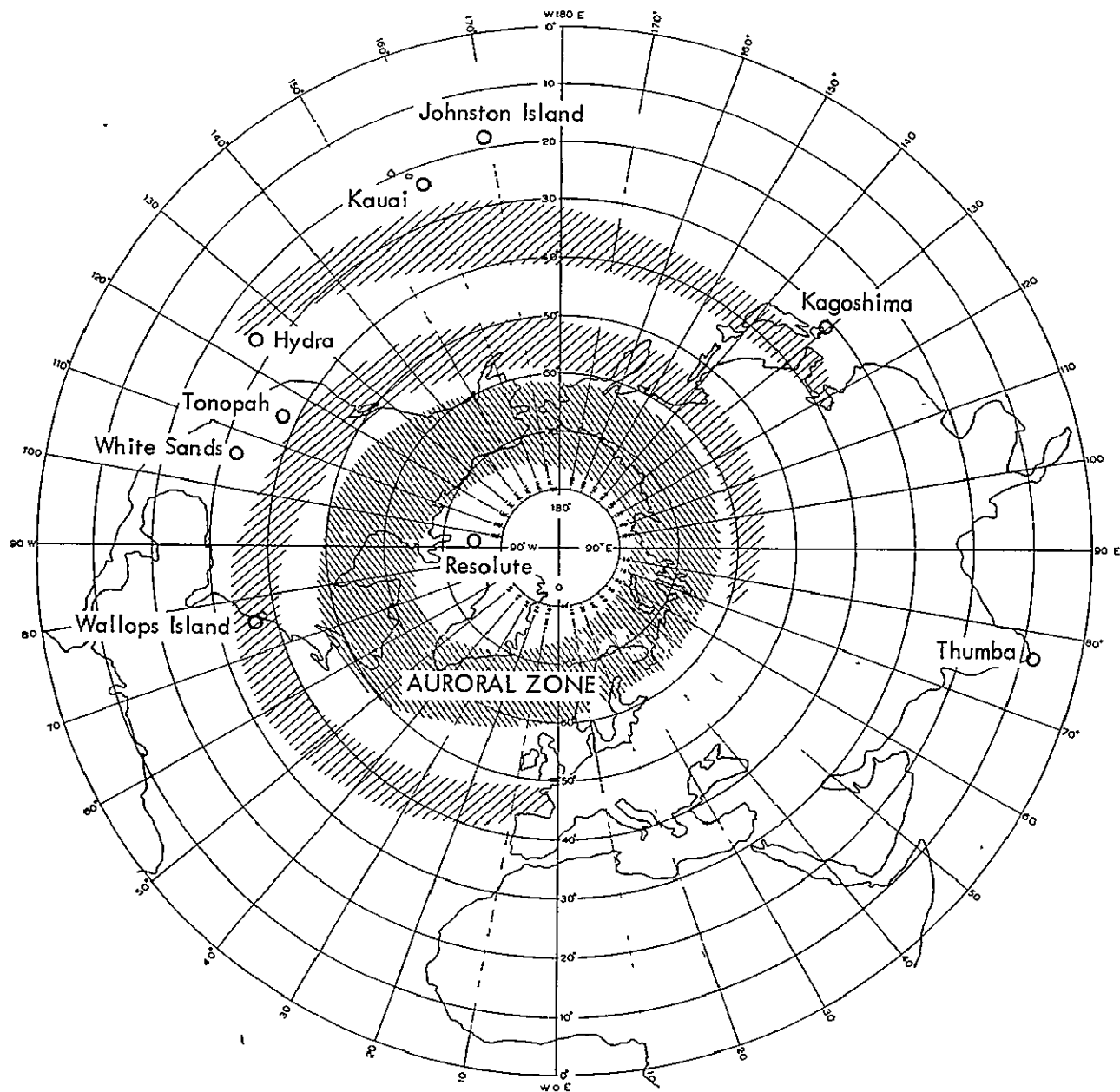


Figure 2.1 Geographic distribution of the observations of 100 keV electrons at altitudes between 240 and 410 km made by a low-altitude satellite [Seward, 1973].

It is postulated that, at least at Wallops Island, energetic electrons are the major source of nighttime *E*-region ionization of N_2 and therefore that 391.4 nm airglow can be expected.

2.1.4 *Spectral characteristics.* The spectral characteristics of N_2 are very well known. In fact, the spectral characteristics are known as a function of vibrational and rotational temperatures so well that these two temperatures can be determined from the observed emission spectrum [Muntz, 1962]. Vibrational and rotational temperatures (related to the vibrational and rotational motions of the molecules) are effective temperatures. "They represent true temperatures only if either the excitation is strictly thermal or is of such a type that it does not affect the thermal distribution" [Hersberg, 1950].

A detailed model of the N_2^+ first negative spectrum (bandhead at 391.4 nm) excited by electron impact has been developed by Degen [1976], and is the model that was used in the design of the photometer. When the discrete line spectra are convolved with a triangular function that has a halfwidth of 0.4 nm, yielding partially integrated results, the curves of Figure 2.2 are obtained. In these curves the peak of each has been normalized to one. Note that the spectrum is a function of temperature.

2.1.5 *Intensity variations.* The intensity of 391.4 nm radiation is a function of the flux of energetic electrons, which in turn is a function of the K index. "Magnetic activity is usually expressed in terms of the so-called 'K index' which is a measure of the local fluctuations on a logarithmic scale, running from 0 to 9. Generally a given K value signifies a higher activity at low latitudes than at high latitudes. The worldwide weighted average is called Kp" [Whitten

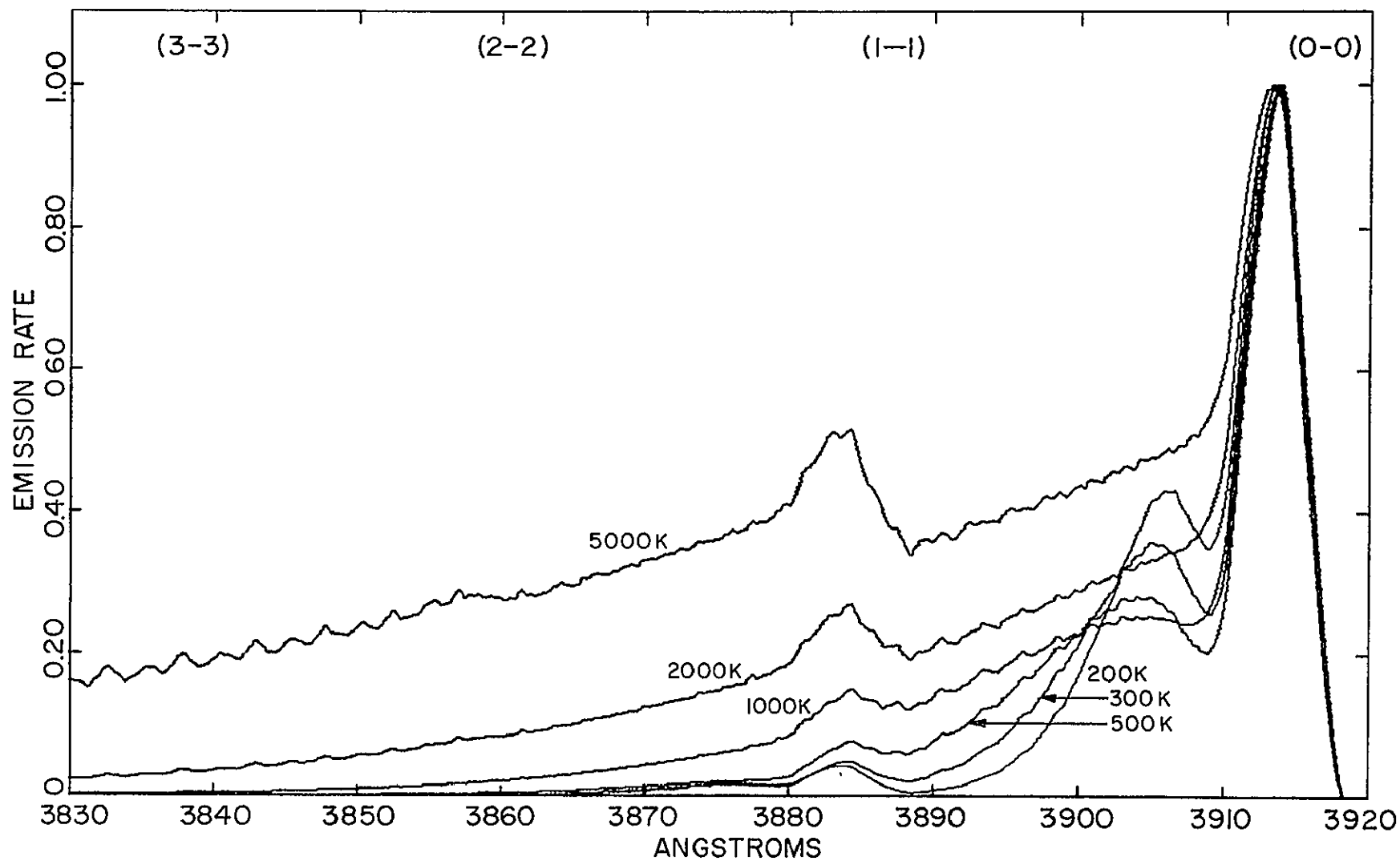


Figure 2.2 Model of 391.4 nm spectrum excited by electron impact at several vibrational and rotational temperatures, and smoothed by a 4 Å triangular halfwidth. For each curve, the vibrational temperature equals the rotational temperature [V. Degen, Univ. of Alaska, private communication].

and Poppoff, 1971]. The intensity during an aurora may be many tens of kilo-rayleighs (kR) whereas the intensity at midlatitudes during quiet geomagnetic conditions may be less than one R. The intensity range anticipated at Wallops Island is from less than 1 R to perhaps as high as 100 R, depending upon geomagnetic conditions.

2.2 Problems Associated with the Measurements

2.2.1 *Other ionization sources.* Not all of the 391.4 nm radiation coming from ionized molecular nitrogen will be caused by energetic electrons. As already mentioned, other sources of ionization of N_2 include helium geocoronal lines (58.4 nm and 30.4 nm), cosmic rays, X-rays, ultraviolet starlight, and energetic protons. When a significant energetic electron flux is present, the other sources listed above are believed to be insignificant, however, under very quiet geomagnetic conditions it may be that they must be considered.

2.2.2 *Vibrational and rotational temperatures.* As can be seen in Figure 2.2, the width of the emission spectrum is a function of vibrational and rotational temperatures. Therefore, when an optical filter is used, the bandwidth of which being more narrow than the emission spectrum, the percentage of the total emission actually measured is a function of temperature. Even knowing the temperature would not suffice since the temperature is a function of altitude and the instrument looks at spectra representing temperatures over a range of values. One solution would be to arrive at an average temperature and use that in the data reduction. Alternatively, a height profile of the temperature could be obtained and used in conjunction with a height profile of the emission measurements. As far as reporting the

emission measurements is concerned, it can be done at an equivalent temperature. That is, calibrate the instrument to give accurate measurements, in terms of rayleighs, at one temperature and then report the emission measurements at that temperature. If some other temperature is found to be more accurate, the measurement magnitudes can easily be translated to the new temperature due to the constant relationships illustrated in Figure 2.2.

2.2.3 *Extraterrestrial light.* Not all of the radiation measured by the photometer will be caused by the ionization of molecular nitrogen. Extraterrestrial light (starlight, etc.), within the passband of the optical filter, will be measured along with the desired radiation. Under disturbed geomagnetic conditions the ultraviolet starlight measured by the photometer will be insignificant compared with the more intense 391.4 nm airglow. Even under quiet geomagnetic conditions this problem will be partially overcome by making differential measurements as the instrument is carried to a high altitude by a rocket, thereby obtaining a height profile of the emission.

2.2.4 *Other airglows.* There are also other airglows that will interfere with the measurements. Because of the characteristics of the optical filter to be used, only wavelengths that fall between 387 nm and 396 nm need be considered and those wavelengths that are within the above range but close to the extremes will be greatly attenuated. One airglow that will interfere with the measurements is the Herzberg bands of O_2 which dominate the night sky spectrum from approximately 310 nm to 490 nm.

Figure 2.3 shows a typical night sky spectrum between the wavelengths of 305 nm and approximately 398 nm. The ν' and ν'' numbers represent

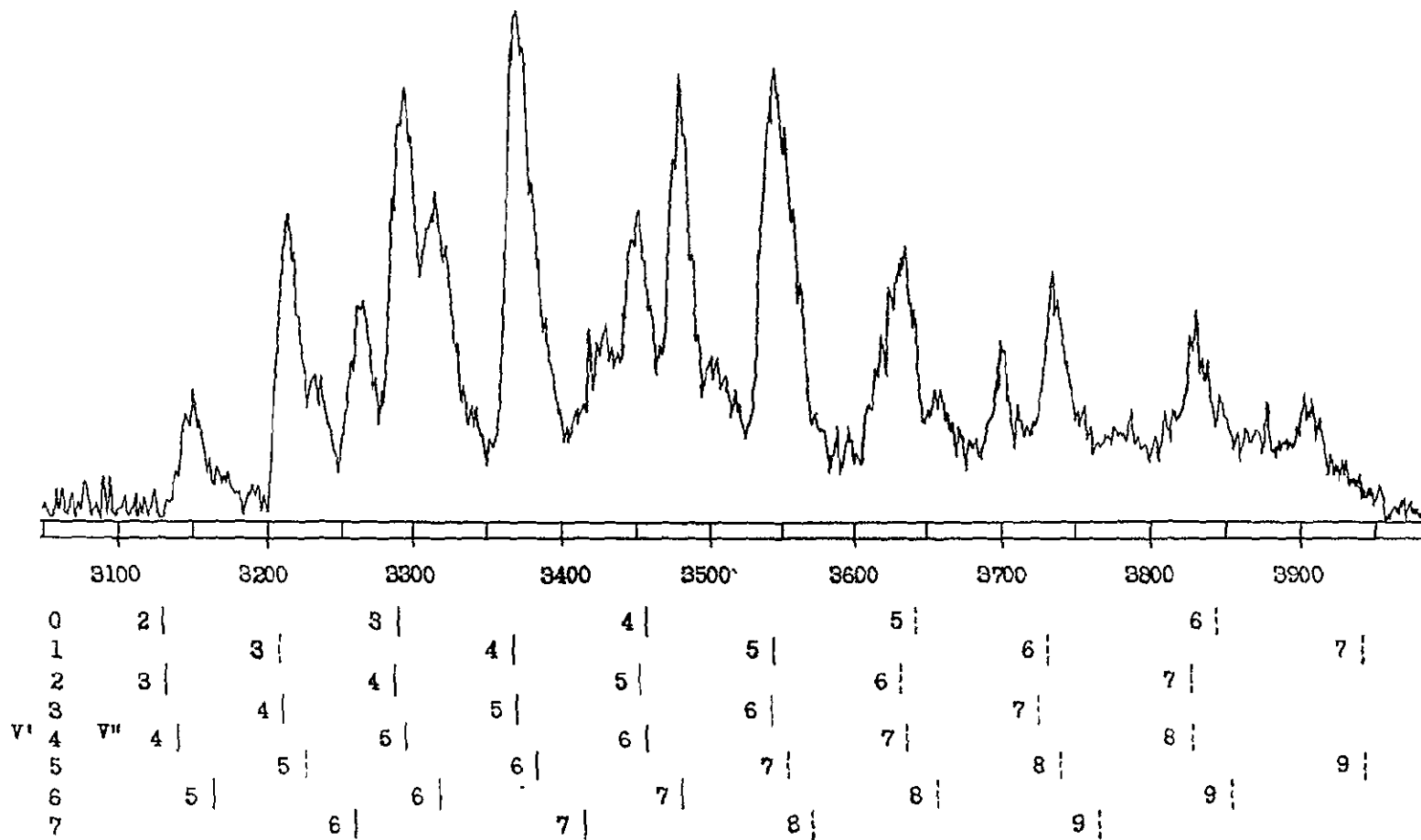


Figure 2.3 Measured night sky spectrum in the range 3050 Å to 3980 Å. Below, the locations of Herzberg bands of the O₂ molecule for the given vibrational level transitions [Krassovsky *et al.*, 1962].

vibrational levels of the molecule: v' being the initial vibrational level and v'' being the final vibrational level. For example, when a transition occurs from vibrational level 3 to vibrational level 5, a photon is emitted in a wavelength band which has a bandhead at 3368.4 Å, as marked below the spectrum. Those bandheads indicated with dashed lines are not identified with certainty. The measurement was made from the ground and primarily shows part of the spectrum of the Herzberg bands of O_2 but other airglows are included and the "spectrogram includes integrated starlight, zodiacal light, radiation scattered by the lower atmosphere, and the effects of absorption by gases in, and the extinction of, the lower atmosphere" [Packer, 1964].

The only Herzberg bands of O_2 that fall between 387 nm and 396 nm are the v' , v'' transitions 1, 7 and 5, 9. According to *Krassovsky et al.* [1962] these transitions result in bands with bandheads at 394.09 nm and 394.10 nm. The bands associated with these bandheads go toward longer wavelengths [see *Chamberlain*, 1961]. The spectrogram in Figure 2.3 indicates that the intensities of these two bands are not very strong. It is not believed that they will cause any serious interference problems with the 391.4 nm airglow measurements. The peak in the spectrogram slightly to the long wavelength side of 390 nm may be the N_2^+ airglow at 391.4 nm.

Another very important night airglow is that produced by the Meinel OH bands. The only band that can possibly interfere with the 391.4 nm airglow measurements is the one with a bandhead at 381.66 nm. Its lines extend to longer wavelengths and four of those lines are within the 387 nm to 396 nm range of interest. Those lines are 387.42, 387.72, 389.10, and 389.37 nm. By referring to Table 9.1

on page 368, Table 13.1 on pages 556 and 557, and to Figure 13.2 on page 555 of *Chamberlain* [1961], it is possible to calculate an estimate of the intensity of these four OH lines using:

$$I = I_A \sum_{i=1}^4 I_{Ri}$$

where

I = total intensity of the four lines in rayleighs

I_A = estimated absolute intensity for the 381.66 nm band
from Figure 13.2

I_R = calculated relative intensities for the individual
lines from Table 13.1

It is found that the total intensity is 0.015 R which is indeed insignificant.

There are a number of atomic oxygen lines of interest that occur in aurora and may also be present in night airglow. These lines are identified by *Chamberlain* [1961] as follows: 387.245, 387.582, 388.245, 388.315, 391.20, 391.9287, 394.5048, 394.75, and 395.4372 nm. However, in an aurora, the N_2^+ first negative band structure is far more intense than all of the above lines together [*Chamberlain*, 1961]. Of the bands within the N_2^+ first negative band structure the 391.4 nm band is by far the most intense. Therefore it is likely that if the above lines are present in the night airglow they will be weak in comparison to the desired 391.4 nm band.

There are two N_2 bands which need to be considered: 394.30 and 394.8 nm. However, in an aurora we see that N_2^+ 391.4 nm radiation is

much more intense than the above-mentioned bands [Chamberlain, 1961]. Again, it is likely that if the above bands are present in the night airglow they will be weak in comparison to the desired 391.4 nm band.

2.3 Rocket Photometry

A photometer is an instrument that produces an electrical output that is a measure of an optical input. It is an electronic instrument that includes some electrical or electronic device that is sensitive to optical radiation, usually some type of lens assembly, and some type of optical filter to determine the band of wavelengths to which it will respond.

By obtaining an altitude profile of a nightglow emission, it is possible to obtain knowledge of upper atmosphere processes. In the present case, it is knowledge about energetic electrons as an ionization source in the nighttime midlatitude E region that is sought. Height profiles will give information about the altitude dependence of energetic electron flux. Measurements from a rocket are the most direct method of obtaining this information.

Height profiles are obtained by making differential measurements; if the measured columnar emission rate (instrument looking straight up) at altitude h_1 is e_1 , and the rate at altitude $h_1 + \Delta h$ is $e_1 - \Delta e$, then the differential layer, Δh , is a source with volume emission rate of $\Delta e / \Delta h$. The volume emission rate is then used in further studies.

Figure 2.4 shows the photometer mounted in the frame of a rocket payload. The diameter of the payload is approximately six inches. A lens cap covers the optical assembly of the instrument. The look-angle of the instrument is 45° with respect to the axis of the payload.

ORIGINAL PAGE IS
OF POOR QUALITY

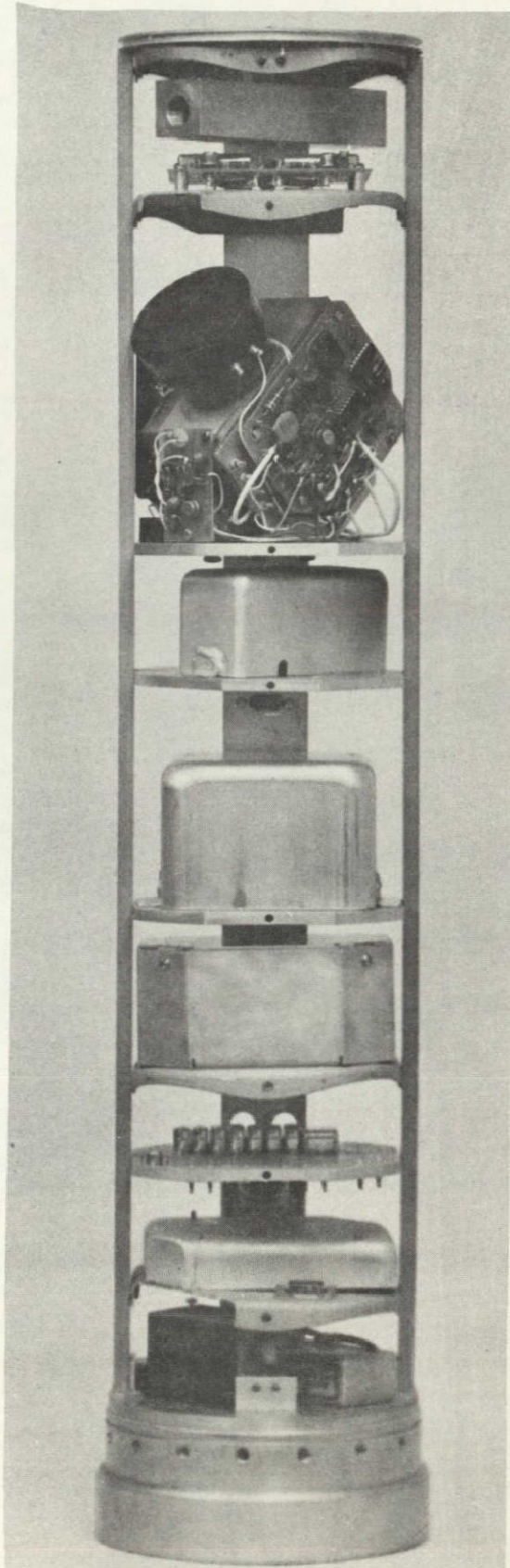


Figure 2.4 The photometer mounted in the frame of the rocket payload.

2.4 *Technological Advances in Photometry*

In recent years there have been several technological advances that have facilitated the development of a 391.4 nm airglow photometer for low intensity measurements. This application requires narrow bandwidth optical filters with close tolerance on the center wavelength. With recent advances in thin-film technology, tighter control during the manufacturing process is possible.

One of the problems associated with any low-level light measurement is the inherent background signal produced by the light-sensitive electronic device, the dark current. Recently devices with very low dark current have been developed that permit measurements of extremely low levels without the necessity of cooling the device below room temperature.

It is common practice when making very low-level light measurements to count photons rather than to attempt to measure an integrated level. Since photons, in the appropriate light-sensitive electronic device, produce low-level electric charge pulses of extremely short duration, very fast electronics is required to amplify and process the data. In recent years integrated circuits have been developed that provide high gain, very high frequency response, fast overdrive recovery, and low noise characteristics. This enables a simplified design of the electronics in a compact, rugged package.

In order to properly design a photometer to measure 391.4 nm airglow, an accurate mathematical model of the emission spectrum is required. As already mentioned, a detailed model of the N_2^+ first negative spectrum has been developed by *Degen* [1976], and is the model

that was used in the design of the photometer. Good mathematical models have been developed and used in the past but the one used here is a more general expression suitable for computer coding at arbitrary vibrational and rotational temperatures.

3. GENERAL DESCRIPTION

The purpose of this chapter is to give a general description of the operation and use of the photometer, giving some details in order to convey understanding of the instrument and instrumentation system.

A photograph of the photometer is shown in Figure 3.1. On the side of the instrument is a +28 V to -23 V converter. At the lower left is the instrument connection plug. At the lower right is a toroidal filter choke and at the upper right is the optical assembly.

The main elements of the photometer are shown as a block diagram in Figure 3.2. These are described in subsequent sections. In addition, the instrumentation system must also include some form of pulse counting or recording equipment, metering equipment, and a low-voltage power supply.

3.1 *Detector*

The detector determines the angle of view, collection area, and radiation pass-band. It provides conversion from photon flux to electrical energy, and includes electrical current gain.

The input to the detector is electromagnetic radiation incident on the optical window of the photometer within the angle of view determined by the optics of the instrument. However, only a very small part of this radiation will be detected by the photometer. The band of electromagnetic radiation that is detected by the photometer is determined by the bandpass characteristics of the optical window material, the optical filter, the lens material, and the channel multiplier cathode material. The bandwidth of the optical

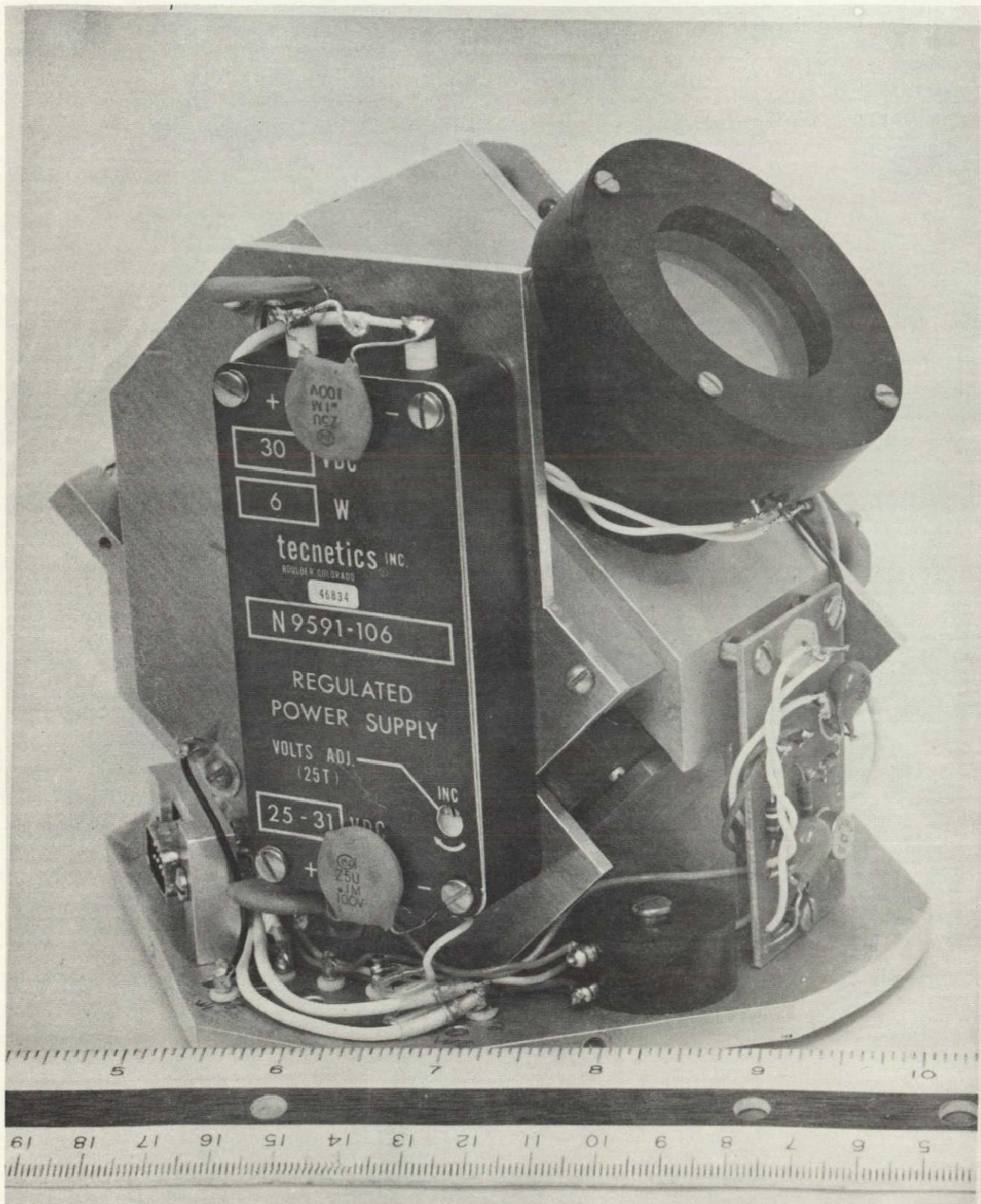


Figure 3.1 A side view of the photometer.

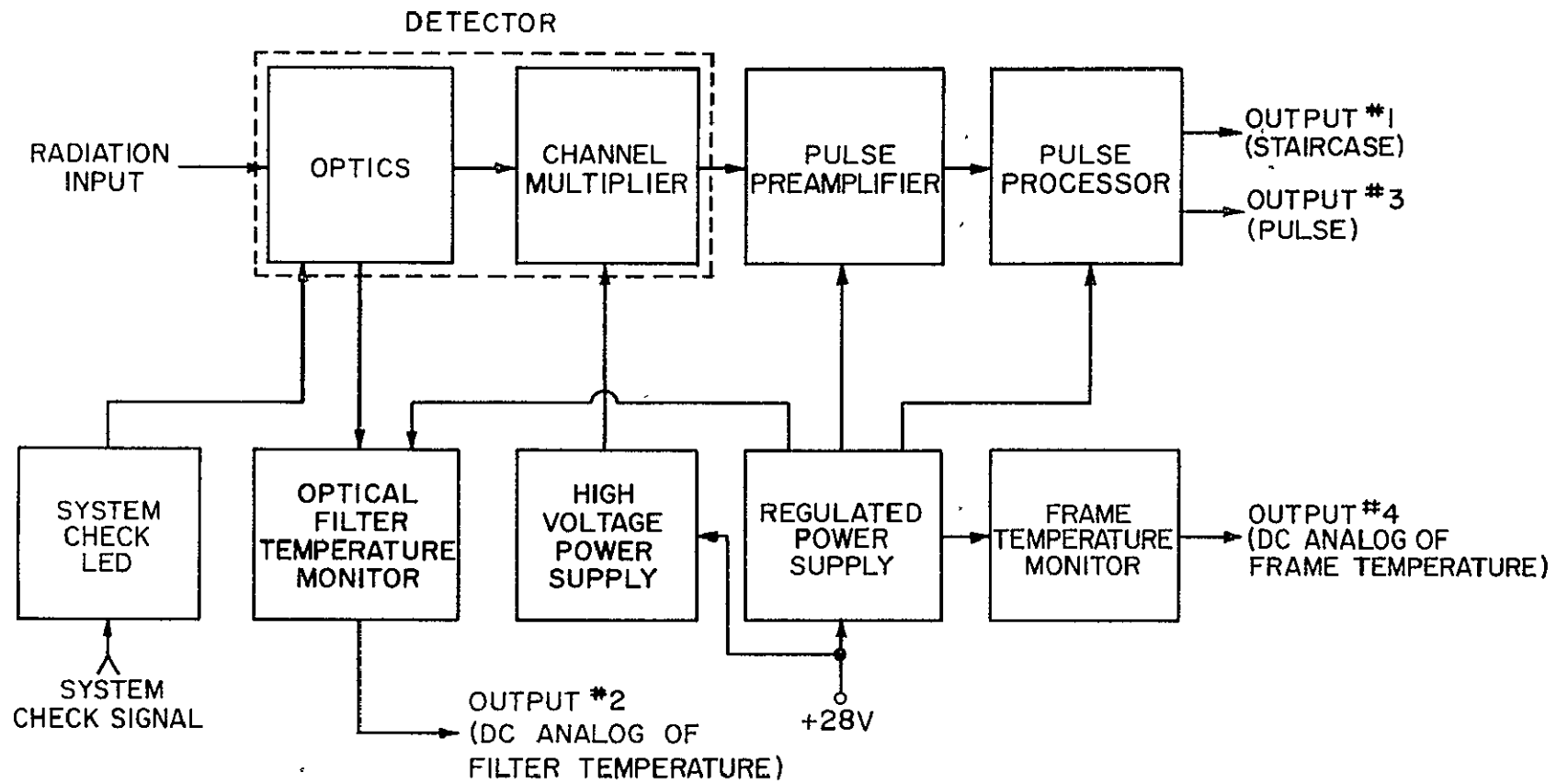


Figure 3.2 Photometer block diagram.

filter is so narrow in comparison to that of the other elements in the optical system that the overall bandwidth is essentially the same as that of the optical filter. It should be noted here that the optical transmission (optical output for unit optical input) of the window and lens material is high (greater than 0.8) at the center wavelength of the optical filter (the wavelength where the greatest optical transmission occurs). The quantum efficiency (number of electrons photoelectrically emitted per incident photon) of the channel multiplier cathode material, although not high (approximately 0.10), is at a maximum at the center wavelength of the optical filter. The optical transmission of the optical filter itself is approximately 0.2 at the center wavelength.

At any given wavelength, the number of electrons photoelectrically emitted per second from the channel multiplier cathode will be determined by the following equation:

$$E = P T_w T_F T_L Q$$

where

E = number of electrons photoelectrically emitted per second by the channel multiplier cathode

P = number of photons at the given wavelength incident on the optical window per second within the angle of view of the photometer

T_w = optical transmission of the optical window at the given wavelength

T_F = optical transmission of the optical filter at the given wavelength

T_L = optical transmission of the lens at the given wavelength
 Q = quantum efficiency of the channel multiplier cathode
at the given wavelength

Over the narrow bandwidth of the optical filter (approximately 1.2 nm), T_w , T_L , and Q are essentially constants.

If an electron has been emitted by the channel multiplier cathode, it has to be the result of a photon within the passband of the optical filter being incident on the channel multiplier cathode. (The dark current is an almost insignificant factor in the channel multiplier used in this instrument). This electron, emitted by the channel multiplier cathode, then undergoes great current amplification as it progresses down the channel. The result is a current (or charge) pulse. In the channel multiplier the current gain is approximately 10^6 , however, the gain is not constant but varies from pulse to pulse. The output charge pulse is therefore a packet of, typically, 10^6 electrons. Due to slight differences in the path taken by individual electrons down the channel and due to repulsion of like charges, the pulse spreads out in time; the charge pulse width is approximately 20 ns. These output pulses are applied to the input of the pulse preamplifier.

3.2 *Pulse Preamplifier*

The purpose of the pulse preamplifier is to accept the output charge pulses of the detector, convert the charge pulses to voltage pulses, and provide sufficient amplification so that output voltage pulses, well above any inherent noise level, can be sent by coaxial cable to following electronic circuits.

The conversion of the charge pulses to voltage pulses is accomplished by the input impedance characteristics of the preamplifier. This impedance will determine the magnitude and pulse width of the input voltage pulses. The input voltage pulses (for this instrument) are of the order of a few millivolts (negative). Actually the input voltage pulses vary considerably in amplitude, because, as noted above, the amplitude of the charge pulses vary considerably.

This variation in input voltage pulse amplitude necessitates a high preamplifier gain to properly amplify small input pulses and fast overdrive-recovery to properly accommodate large input pulses.

Since the input pulses are very narrow (very short time duration), the preamplifier must have wide bandwidth in order to properly amplify the pulses. High gain coupled with wide bandwidth necessitate that the circuit must have low-noise characteristics, since noise output is directly related to gain and bandwidth.

The preamplifier provides positive output pulses of about 4 V for input pulses as small as 2 mV. The output pulse width is a function of input pulse amplitude, varying from approximately 30 ns for a 2 mV input to 40 ns for a 500 mV input. These output pulses are applied to the input of the pulse processor.

3.3 *Pulse Processor*

The first two stages in the pulse processor provide further amplification and also pulse stretching (increasing the time duration). The further amplification gives improvement in sensitivity, triggering the following stage even when the output of the preamplifier is less than 4 V. The pulse stretching insures reliable triggering of the following stage, of which the minimum input pulse width specification is 50 ns.

The following stage is a monostable Schmitt trigger which provides a constant-amplitude constant-pulse-width output and some noise immunity by not responding to inputs below a set level.

The remaining circuitry provides an interface between the output of the monostable Schmitt trigger stage and the VCO (voltage controlled oscillator) of the rocket payload telemetry system. The interface contains a frequency divider and a staircase generator. Each step on the staircase represents N counts or pulses; this is selectable so that each step may represent 1, 2, 4, 8 or 16 counts. At low count rates (i.e., low 391.4 nm emission rates) the individual steps on the staircase are easily identifiable at the telemetry receiving station. At higher count rates the individual steps on the staircase will not be identifiable but only separate staircases (each staircase has 16 steps, and represents a total of $16 \times N$ counts: see Figure 3.3). At higher count rates less resolution is needed for the same degree of accuracy. This arrangement maximizes resolution without exceeding the bandwidth restrictions of the assigned telemetry channel.

If ground-based measurements are to be made using this photometer, the interface may not be needed. Output pulses, one positive pulse for every charge pulse from the detector, are available at output #3 (see Figure 3.2). This output by-passes the interface circuitry.

3.4 Temperature Monitors and System Check

As mentioned previously, the optical filter has a very narrow bandwidth (approximately 1.2 nm); the emission spectrum that we wish to measure (391.4 nm) is also very narrow. Therefore, the optical signal output of the filter is highly dependent upon the

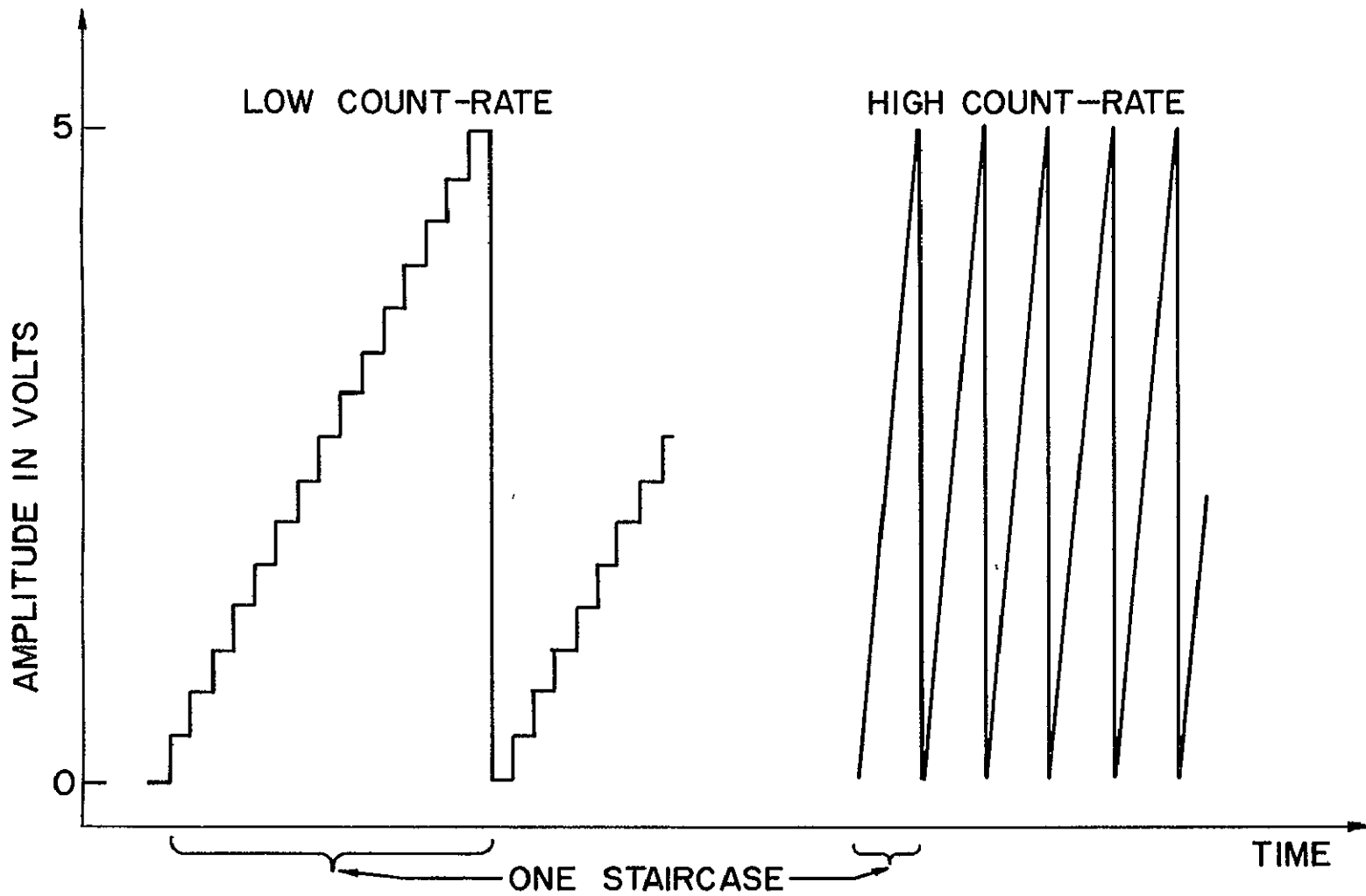


Figure 3.3 Output #1 of Figure 3.2. Individual steps can be seen in the low count-rate waveform but not in the high count-rate waveform.

center wavelength of the filter, and the center wavelength must be precisely known. The center wavelength of the filter is temperature dependent. If the filter temperature and the temperature characteristics of the filter are known, then shifts in filter center wavelength caused by temperature can be taken into consideration when interpreting the output of the photometer.

The output of the filter temperature monitor (output #2 in Figure 3.2) is designed to be a dc voltage varying from 0 to 5 V depending upon the temperature of the filter. Upon calibration the output voltage can be translated into filter temperature.

Other parts of the photometer are also temperature sensitive, in particular the gain of the channel multiplier. Therefore it is desirable to measure the instrument frame temperature. Since the channel multiplier is completely surrounded by the frame and is in physical contact with it, the frame temperature and the channel multiplier temperature will be essentially the same. Upon calibration, the gain of the electronics can be determined as a function of frame temperature and taken into consideration when interpreting the output of the photometer.

An LED (light emitting diode) has been mounted in the optical assembly to provide verification that the instrument is operating satisfactorily. On the ground, the LED may be turned on manually to check the system performance. When launched in the payload of a rocket, baroswitches will automatically turn on the LED between the altitudes of 40 kft and 70 kft, both on ascent and descent, to perform preflight and post-flight system checks.

3.5 Rocket-borne Instrumentation System

The staircase output of the photometer (output #1 in Figure 3.2) determines the frequency of a VCO (voltage controlled oscillator). The VCO output, summed with other VCO outputs, modulates the FM transmitter of the payload.

In the ground-based telemetry station the transmitted signal of the rocket payload is received and FM demodulated. The FM demodulated signal, corresponding to the input of the payload FM transmitter, is recorded on analog tape. The FM demodulated signal is also connected to a bandpass filter followed by a frequency discriminator to recover the staircase signal, which is then recorded on a chart recorder. The staircase signal is either digitized in real time and recorded on magnetic tape or the analog tape signal, after passing through the appropriate bandpass filter and frequency discriminator, is digitized at a later time. From these records, and other records recorded during the rocket flight, the zenith-corrected count rate at any given time during the flight may be derived.

Major advantages of a rocket-borne instrumentation system are as follows: 1) the rocket will be above scattered light from ground sources for most of the flight, and 2) differential measurements (the change in measured emission rate for unit change in altitude) allow the construction of a graph showing the height profile of measured radiation.

The main elements of the rocket-borne instrumentation system are shown as a block diagram in Figure 3.4.

Figure 3.5 shows the photometer seen through the open door of the

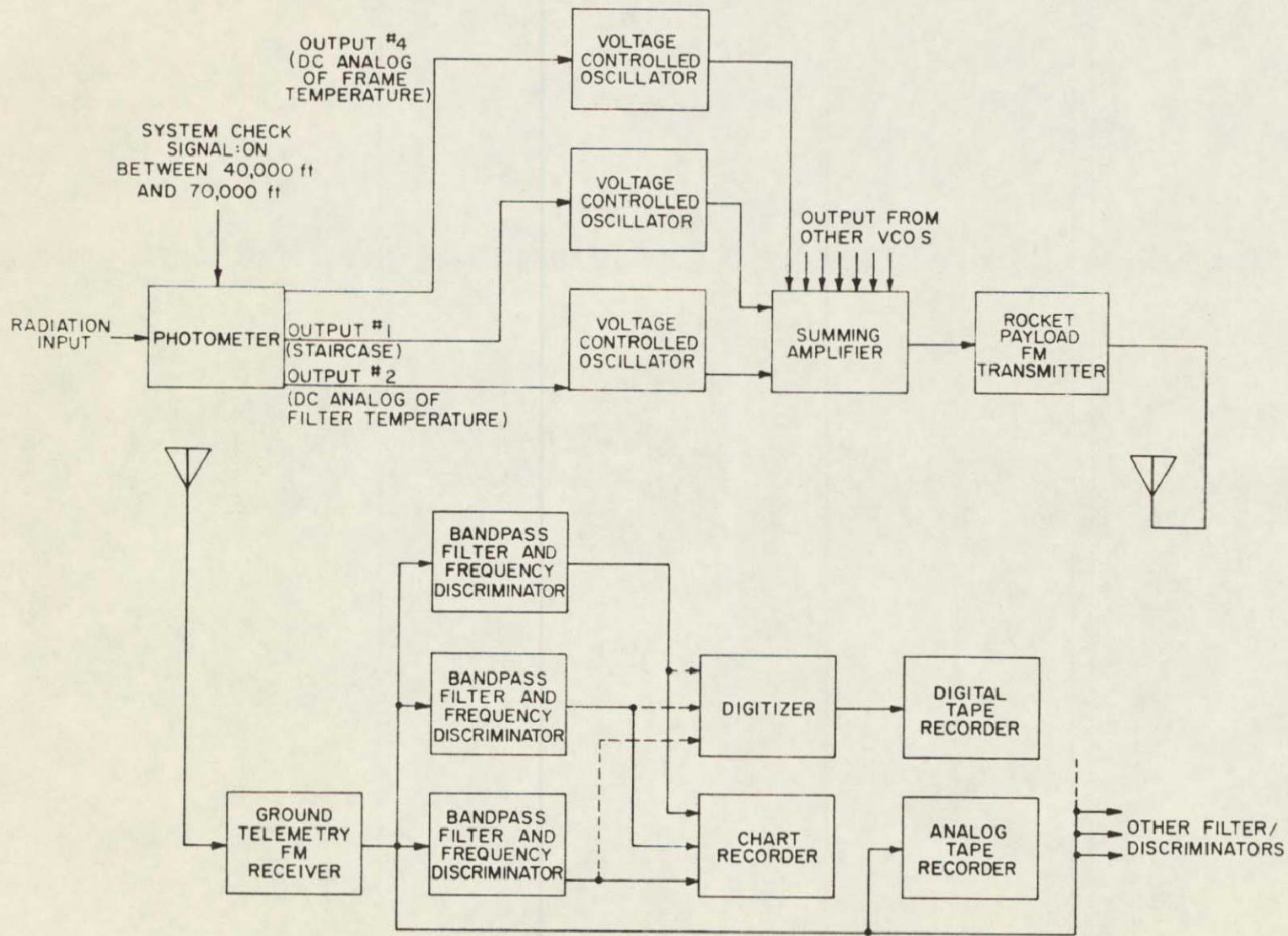


Figure 3.4 Rocket-borne instrumentation system block diagram.

ORIGINAL PAGE IS
OF POOR QUALITY

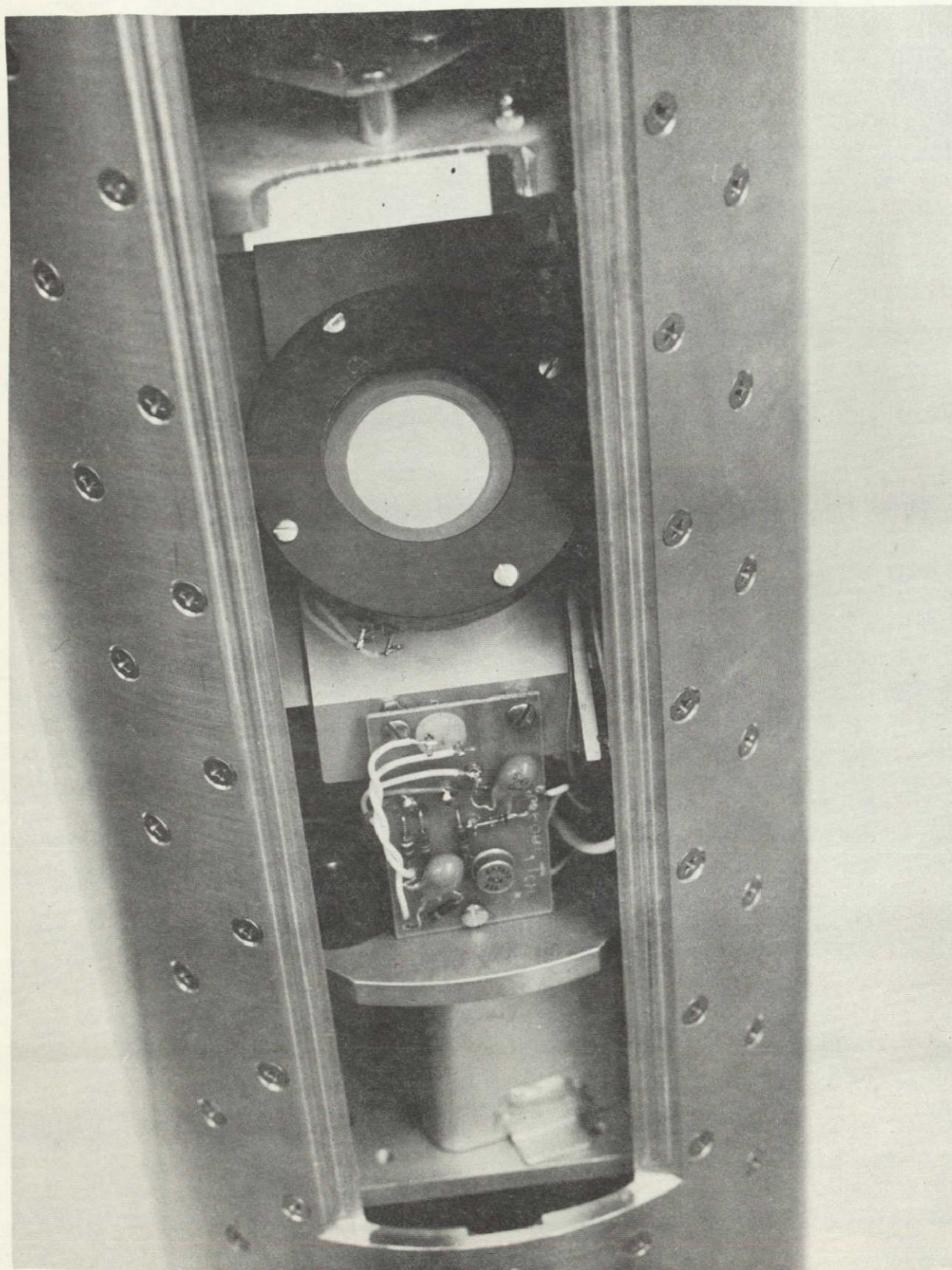


Figure 3.5 The photometer seen through the open door of the rocket payload.

rocket payload. During the first part of the flight, the doors (one on this side of the payload and one on the opposite side) are on the payload; they are blown off by an explosive charge at an altitude of 40 km.

3.6 *Ground-based Instrumentation Systems*

If the photometer is used for ground-based measurements, the staircase output of the photometer (output #1 in Figure 3.2) is connected directly to the input of a chart recorder. With a time-mark channel on the same chart recorder as well as temperature channels, the measuring system may be left unattended. From these records and knowledge of the photometer calibration, the measured emission rate is obtained for any time period on the record of interest (see Figure 3.6).

An alternative for unattended operation is to connect the staircase output of the photometer to a VCO (voltage controlled oscillator) and then record the output of the VCO on analog tape. The temperature outputs of the photometer are also connected to VCOs, the outputs of which are recorded on other channels of the same analog tape. Time marks are recorded on a fourth channel of the analog tape. Later, the appropriate output of the analog tape is connected to a frequency discriminator to recover the staircase for display on a chart recorder or oscilloscope. The appropriate output of the analog tape can be converted to temperature directly from the channel frequency, or it could be converted back to a dc voltage first by means of a discriminator. From these records and knowledge of the photometer calibration, the emission rate may be obtained for any time period on the record of interest. If it is desired to analyze the

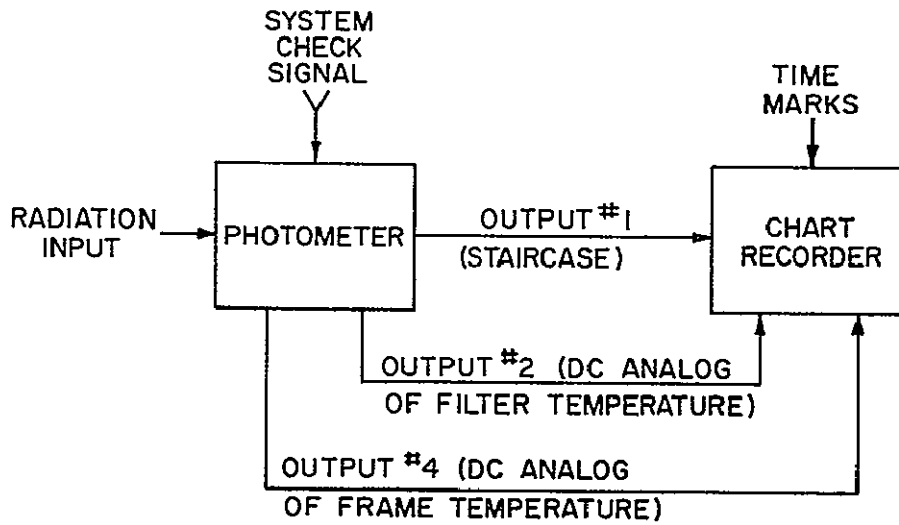


Figure 3.6 Ground-based instrumentation system block diagram, method 1.

entire analog tape record, the tape signals may be processed digitally (see Figure 3.7) and a graph showing emission rate versus time may be obtained.

When only one or a few measurements are desired, e.g., a measurement at one time and one place, it may be preferable to by-pass the interface circuitry of the photometer (frequency divider and staircase generator) and connect the pulse output of the photometer (output #3 in Figure 3.2) through a 10 to 1 scope probe to the input of a frequency counter (see Figure 3.8). Using this method the photometer count rate may be observed directly. And again, having knowledge of the photometer calibration, the emission rate may be obtained.

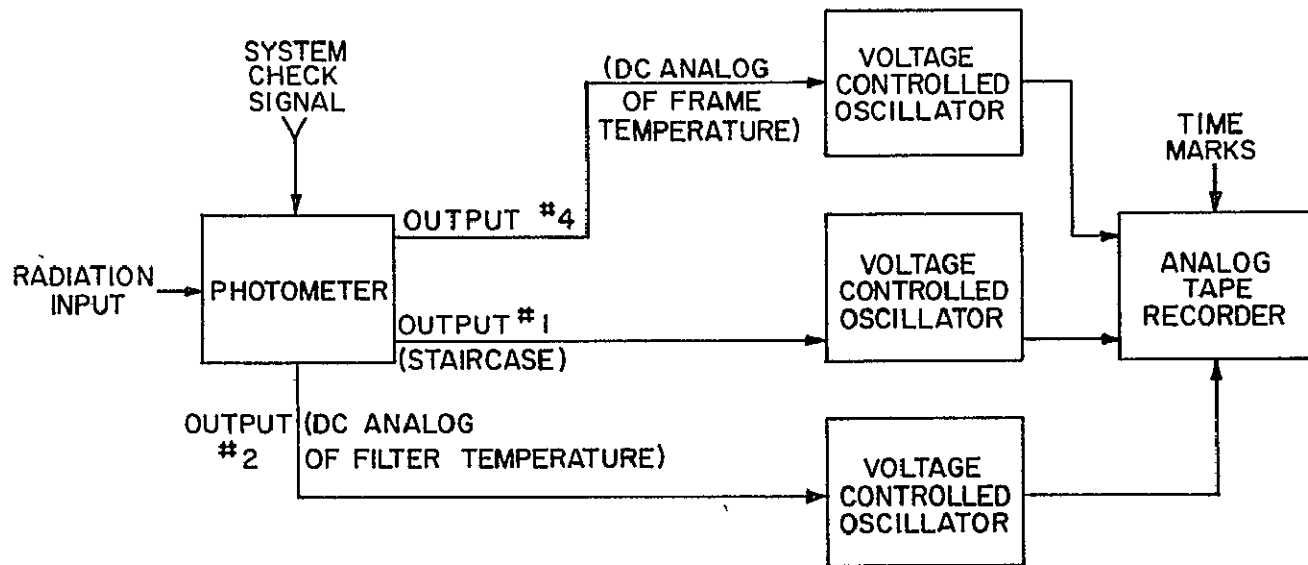


Figure 3.7 Ground-based instrumentation system block diagram, method 2.

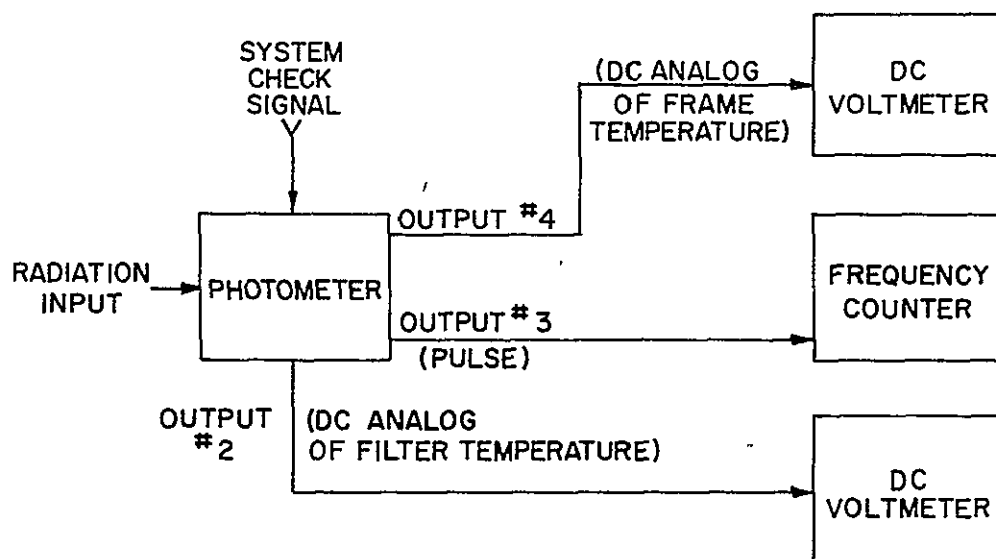


Figure 3.8 Ground-based instrumentation system block diagram, method 3.

4. DETECTOR

The purpose of this chapter is to present technical details of the photometer detector beyond that given in Chapter 3. The photometer detector includes the optical window, optical filter, lens, channel multiplier, and optical housing. The two most important components in the photometer detector, and in the entire instrument, are the channel multiplier and optical filter. Therefore these two components will be considered first.

4.1 *Channel Multiplier*

4.1.1 *Selection considerations.* The channel multiplier used in the photometer is a type of photodetector. A photodetector is a device that senses incident radiation and provides an electrical output analog of that radiation. There are a number of characteristics, both electrical and mechanical, that need to be considered when selecting a photodetector for this specific application. These considerations are presented below.

The electrical characteristics of a photodetector, whether it is a solid-state device or a vacuum tube, include 1) spectral response, or the radiation band over which it is sensitive, 2) gain, or electrical output for unit optical input, and 3) dark current, or electrical output with no optical input. For the present application the spectral response of the photodetector must include 391.4 nm and it is desirable that the response be at a maximum at that wavelength. In addition, the electrical signal output must be large enough to be readily detectable even for very weak optical radiation, which this instrument is intended to measure. Also, the dark current must be very small or it will mask the desired signal.

There are two basic modes of operation for a photodetector, 1) current integrating mode, where the output current of the device is measured or a directly related voltage, and 2) photon counting mode, where output charge pulses of the device are counted. The current integrating mode requires that the gain of the device be constant in order for accurate measurements to be made. For a weak input radiation the output current becomes very small and difficult to measure even when the gain of the device is high. A major advantage, however, to this mode of operation is that it need not respond rapidly to individual photons since the output is integrated anyway.

The photon counting mode requires the device to respond very rapidly to individual photons and is limited to relatively weak radiation measurements. The above limitation is a result of the maximum count-rate at which the device is capable of operating. However, there are three very important advantages to photon counting: 1) the gain of the device need not be constant because only the presence of an output pulse need be detected, 2) the amplitude of the output pulses will be relatively the same regardless of how weak the input radiation may be, and 3) the necessary electronic circuitry will be inherently more reliable and stable.

The third advantage mentioned above requires further comment. When the current integrating mode is used, it is a dc quantity that must be measured, corresponding to a constant input radiation. The electrical output of the instrument is inherently dependent upon power supply voltages, temperature changes, and component value changes.

Although many of these sources of error can be effectively reduced by feedback, or more sophisticated techniques such as using chopper-stabilized amplifiers or a chopper-driven shutter in the optical section, the sources of error remain. When the photon counting mode is used, relatively simple circuitry is required. If the gain of the device changes, or that of the preamplifier, little change in the instrument output count-rate will occur. If the gain of the preamplifier changes, so will the threshold level (the minimum input pulse amplitude that is detectable) of the photometer electronic circuitry. But if the threshold level is very low, changes in the threshold level will have little effect on the count-rate since essentially all input pulses will be counted.

For the above reasons, photon counting is preferable over measuring the integrated current in this application.

This photometer is designed to be used in the payload of a Nike Apache rocket and therefore the photodetector must have the following mechanical characteristics: be physically small to fit (with the accompanying optics and electronic circuits) in a payload of 6.5 in (16.5 cm) diameter, be light weight, and be mechanically rugged to withstand the g forces and vibration levels experienced in a Nike Apache payload (see Appendix I).

4.1.2 *The multiplier and accompanying high voltage power supply.*

With the above considerations in mind the EMR Photoelectric channel multiplier model 521N-01-CM was selected. Table 4.1 contains some of the important characteristics of the device. Note the extremely low dark-current count-rate, ruggedness, and small size. Table 4.2 shows some actual measured characteristics of the three units obtained.

Figure 4.1 shows a photograph of the device both potted and unpotted.

Table 4.1

Important Characteristics of the
521N-01-CM Channel Multiplier

	<u>Min.</u>	<u>Typ.</u>	<u>Max.</u>	<u>Units</u>
I. Physical Characteristics				
Weight unpotted		10		grams
Length unpotted		76		mm
Dia. unpotted			8	mm
Length potted		86.4		mm
Dia. potted			12.7	mm
II. Photocathode Characteristics				
Detectivity*, 410 nm (essentially the same at 391.4 nm)	8	14		%
Dark current at a gain of 5×10^7		6		cts/sec
III. Channel Characteristics				
Voltage required for a gain of 5×10^7		3300		V
Anode pulse width			20	nsec
IV. Maximum Ratings				
Supply voltage		3800		V
Recommended count-rate at a gain of 10^7		2×10^5		cts/sec
V. Environmental Characteristics				
Shock, 11 ms duration		100		g
Vibration, 20 to 3000 H_z		30		g
Temperature	-55		75	$^{\circ}C$

* Detectivity is defined as the ratio of the number of anode pulses out to the number of photons in at the cathode.

Table 4.2

Summary of Measured Characteristics
of 521N-01-CM Channel Multipliers

Detectivity at 4100 Å:

Serial No. 160, 10.7%
Serial No. 203, 10.2%
Serial No. 334, 13.0%

Voltage required for a gain of 1×10^7 :

S.N. 160, 2790 V
S.N. 203, 2900 V
S.N. 334, 2800 V

Voltage required for a gain of 5×10^7 :

S.N. 160, 3230 V
S.N. 203, 3340 V
S.N. 334, 3170 V

Dark counts:

S.N. 160, 5 counts/sec at 2790 V
S.N. 203, 2 counts/sec at 2850 V
S.N. 334, 1 count/sec at 2850 V

Channel resistance:

S.N. 160, 7.18×10^8 ohms
S.N. 203, 7.58×10^8 ohms
S.N. 334, 5.1×10^8 ohms

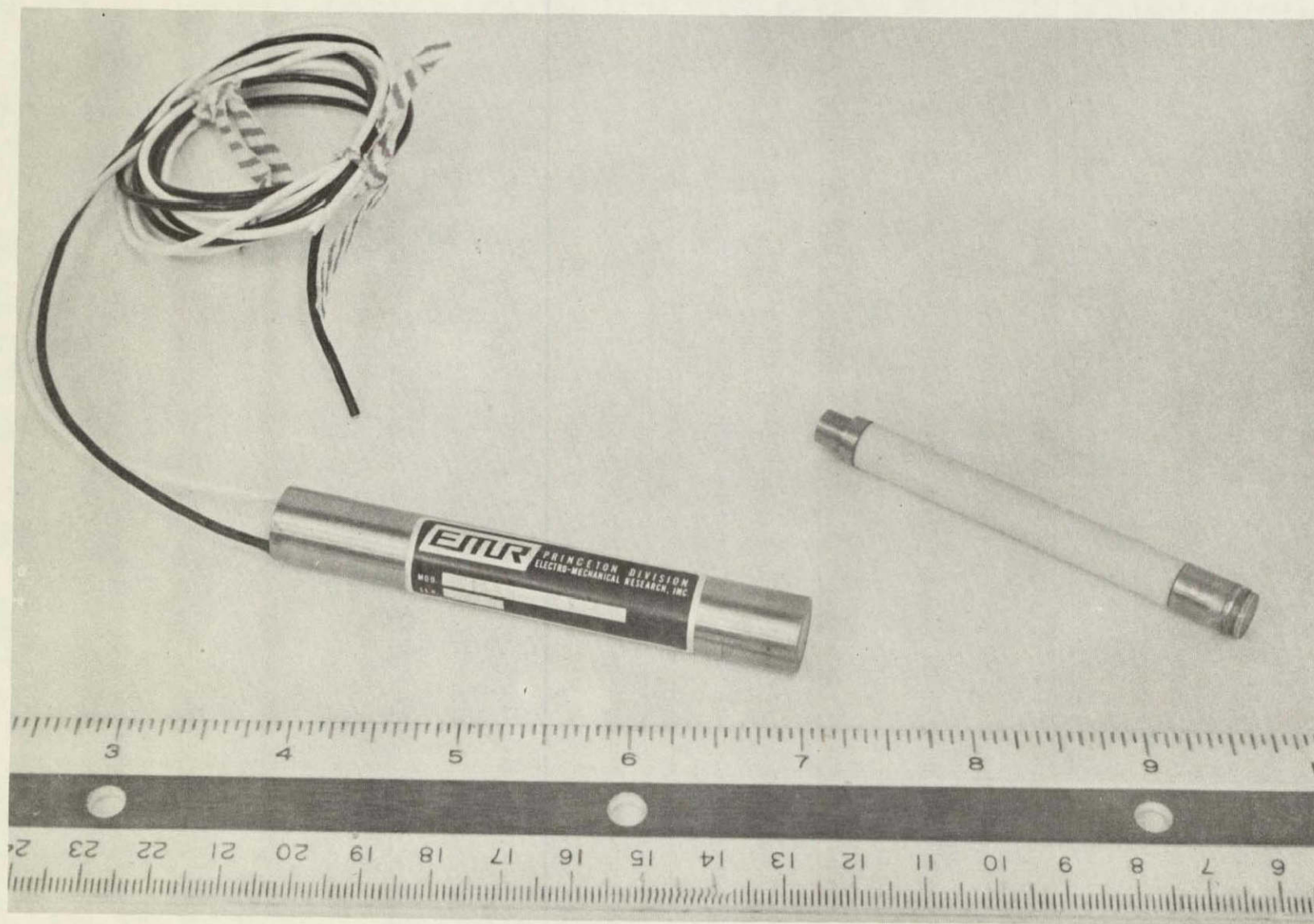


Figure 4.1 The channel multiplier tube, potted on the left and unpotted on the right.

ORIGINAL PAGE IS
OF POOR QUALITY

The channel multiplier is a two-terminal device that operates with a high dc voltage applied from photocathode to anode. The dc voltage produces a voltage gradient along the length of the channel. When a photon strikes the photocathode, there is a certain probability (approximately 0.1 for this device) that an electron will be emitted due to the release of the energy of the photon. This electron emitted by the photocathode will be electrostatically focused into the channel and will be accelerated by the voltage gradient until it strikes the side of the channel. The channel material has a high secondary-emission ratio and when struck by a high-velocity electron will liberate many electrons. This liberated packet of electrons will then be accelerated by the voltage gradient until it strikes the side of the channel and secondary emission again occurs, and so forth down the channel. The result is that for each electron emitted by the photocathode a charge pulse (e.g., 10^6 electrons) will arrive at the anode (see Figure 4.2).

The channel multiplier requires a high voltage power supply capable of delivering about 10 μ A at approximately 3000 V. To be compatible with the rocket payload, it is desirable that the high voltage power supply operate from a 28 V dc input. In addition, the unit must have low ripple, good regulation, good power efficiency, small size, and be rugged, and be capable of operation at any altitude. With the above considerations in mind the EMR model 640E-2 high voltage power supply, with negative ground, was selected.

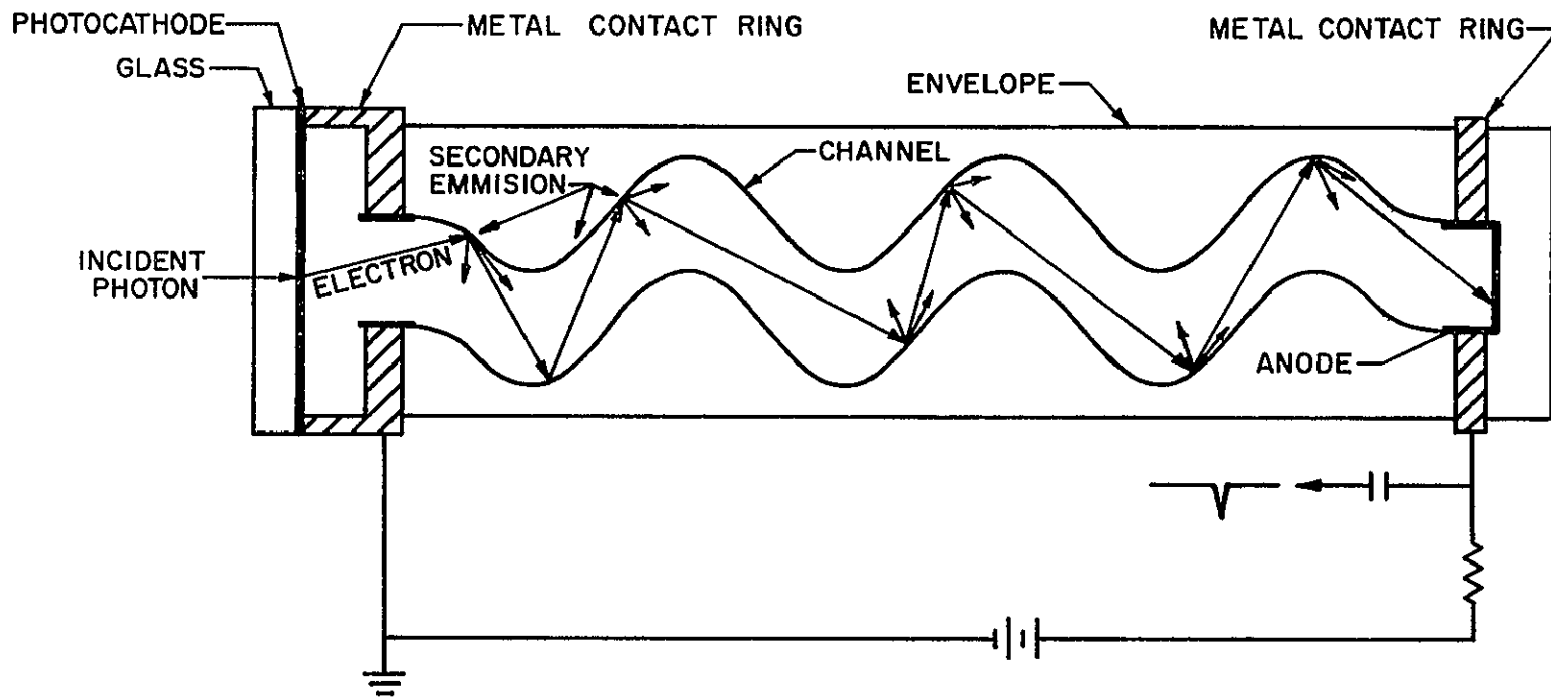


Figure 4.2 Operation of a channel multiplier.

4.2 *Optical Filter*

4.2.1 *Theoretical introduction.* Types of bandpass filters include absorption filters, combinations of edge filters, polarization filters, frustrated total reflection filters, and Fabry-Perot filters. Absorption filters and combinations of edge filters do not have bandpass characteristics as narrow as is needed in this application. Polarization filters, capable of extremely narrow passbands, are complicated and massive [Gray, 1957; Heavens, 1965]. Frustrated total reflection filters have inherent theoretical disadvantages when compared with Fabry-Perot filters (e.g., high center wavelength dependence upon the polarization of the incident radiation) and have construction difficulties at least as great as Fabry-Perot filters [MacLeod, 1969]. Fabry-Perot filters are capable of very narrow passbands utilizing modern thin-film technology, and are widely used in photometry. Therefore, only Fabry-Perot filters (and modifications thereof) will be considered here.

Fabry-Perot filters are a type of interference filter. An interference filter is "An optical filter in which the wavelengths that are not transmitted are removed by interference phenomena rather than by absorption or scattering" [Billings, 1971]. The terms "Fabry-Perot filter" and "interference filter" are often used interchangeably; however, the operations of other filters are also dependent upon interference phenomena (e.g., the frustrated total reflection filter). But due to the popularity of Fabry-Perot filters, "interference filter" usually means a Fabry-Perot filter or modification thereof. The description of a Fabry-Perot filter

follows [Gray, 1957; Heavens, 1965; Lipson and Lipson, 1969; Macleod, 1969; Billings, 1971].

The Fabry-Perot filter is based on the Fabry-Perot interferometer (see Figure 4.3), the major difference being the thickness of the dielectric layer that is between the partially reflecting layers. In the interferometer (an optical instrument, the position of one of the partially reflecting layers is adjustable thereby varying the thickness of the dielectric layer) the thickness of the dielectric layer (often air) is on the order of centimeters. In the Fabry-Perot filter the thickness of the dielectric layer is normally a few hundred nm.

In reference to Figure 4.3, we see that the transmitted radiation will involve the sum of the transmitted terms TT' , R^2TT' , R^4TT' , However, the wavelength thickness of the dielectric layer must be considered and therefore the summation is [Lipson and Lipson, 1969]

$$TT' \sum_{p=0}^{\infty} R^{2p} \exp(-jkps)$$

where

p = number of the transmitted beam

k = $2\pi/\lambda$

s = optical path difference between successive reflections
at the same surface

This is a geometric series and its sum to infinity is

$$\frac{TT'}{1-R^2 \exp(-jks)}$$

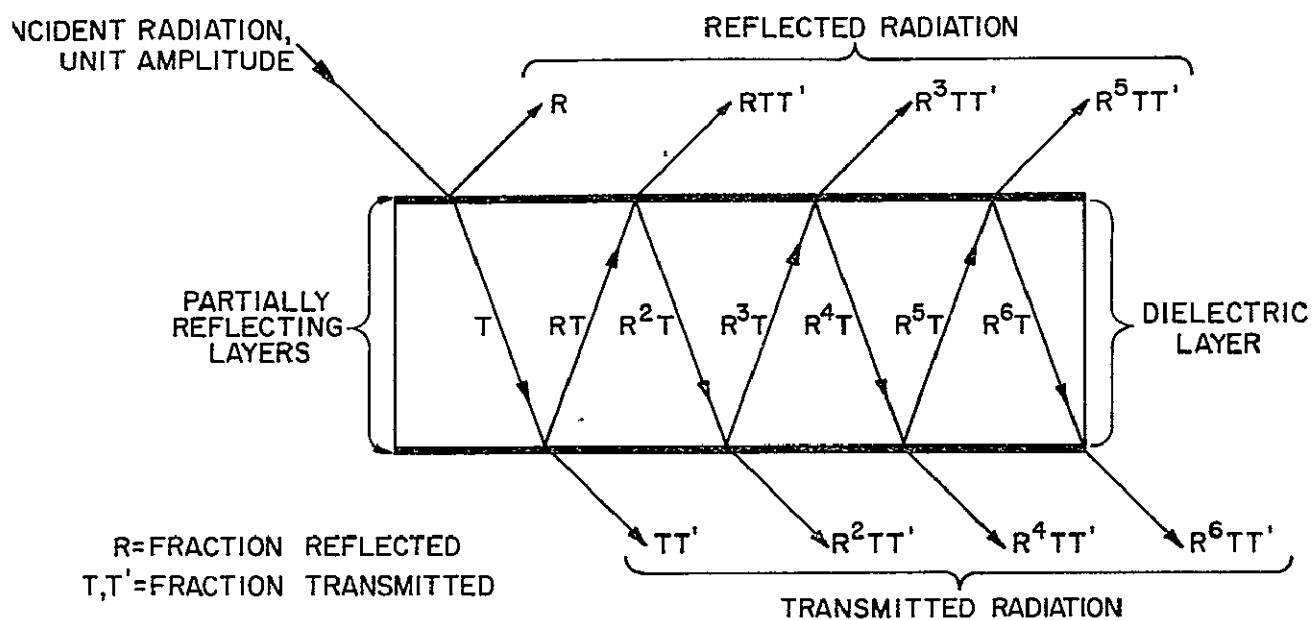


Figure 4.3 Multiple internal reflections in a Fabry-Perot interferometer or filter. The angle of incidence is nearly normal; it is exaggerated here for clarity.

The intensity, which is equal to the above expression multiplied by its complex conjugate is

$$I = \frac{(TT')^2}{1+R^4-2R^2\cos(ks)}$$

This expression has a maximum value of $(TT')^2/(1-R^2)^2$ when s is an integral number of wavelengths and it has a minimum value of $(TT')^2/(1+R^2)^2$ when s is an odd number of half-wavelengths. Therefore,

$$\frac{I_{\max}}{I_{\min}} = \left[\frac{1+R^2}{1-R^2} \right]^2$$

Figure 4.4 illustrates how the sharpness of the transmission bands are influenced by the value of R .

A complete Fabry-Perot filter may be manufactured by thin-film techniques. Figure 4.5 illustrates the transmittance versus wavelength response of an assembly consisting of a dielectric layer bounded by two metallic reflecting layers. If the response at $0.69 \mu\text{m}$ is desired, for example, the shorter wavelength responses can be suppressed by an absorption filter, the transmittance of which is shown as curve b in the figure. The longer wavelength responses may be suppressed by some other means (e.g., the photocathode of the photodetector used with the filter may have a spectral response insensitive to the longer wavelengths).

For very narrow bandpass Fabry-Perot filters the reflectance of the partially reflecting layers must be quite high (see Figure 4.4). For metallic reflecting layers the losses due to absorption can be objectionable and there is a marked improvement in performance if the

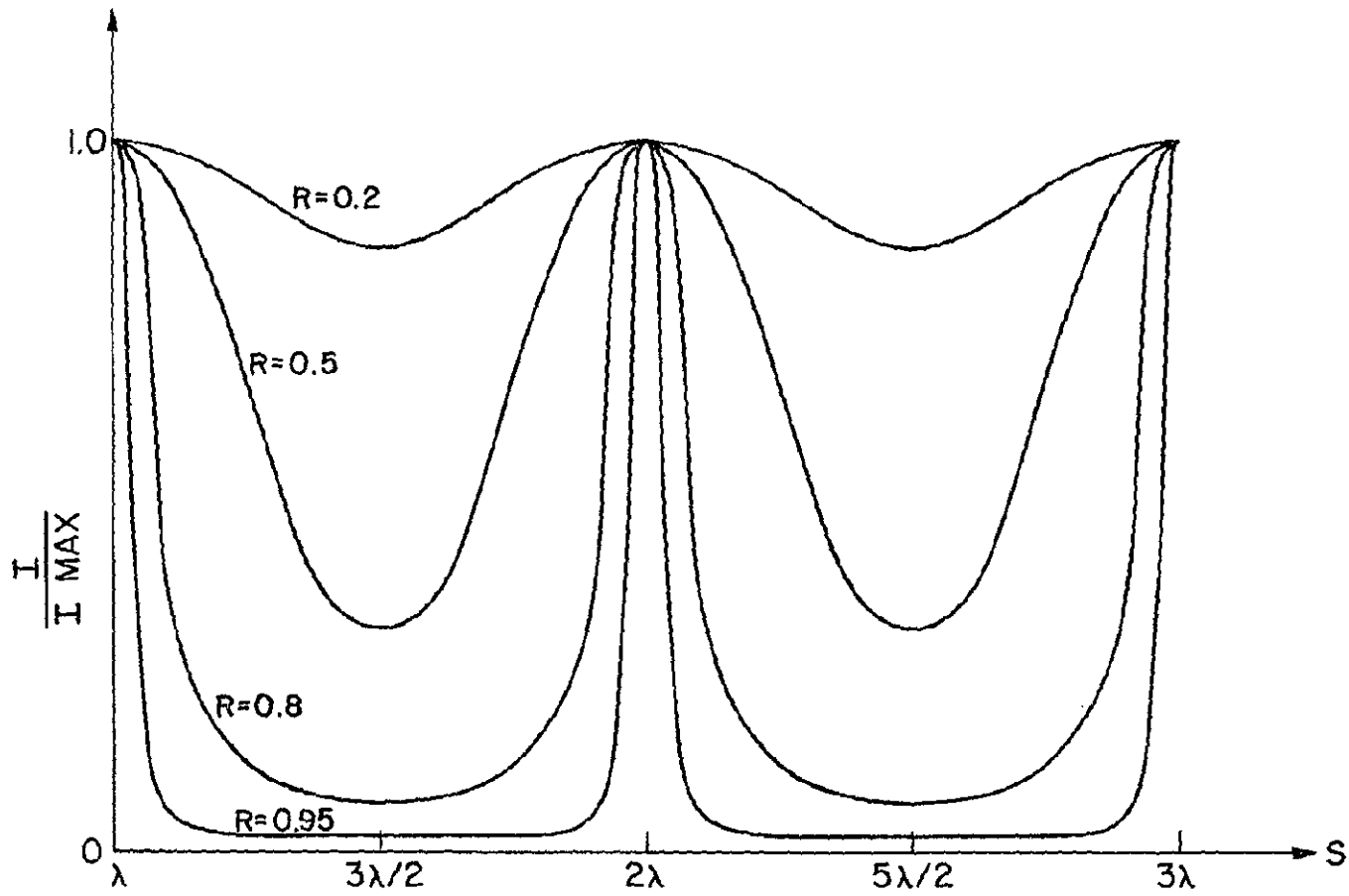


Figure 4.4 The sharpness of Fabry-Perot filter transmission bands as a function of reflectance, R [Lipson and Lipson, 1969].

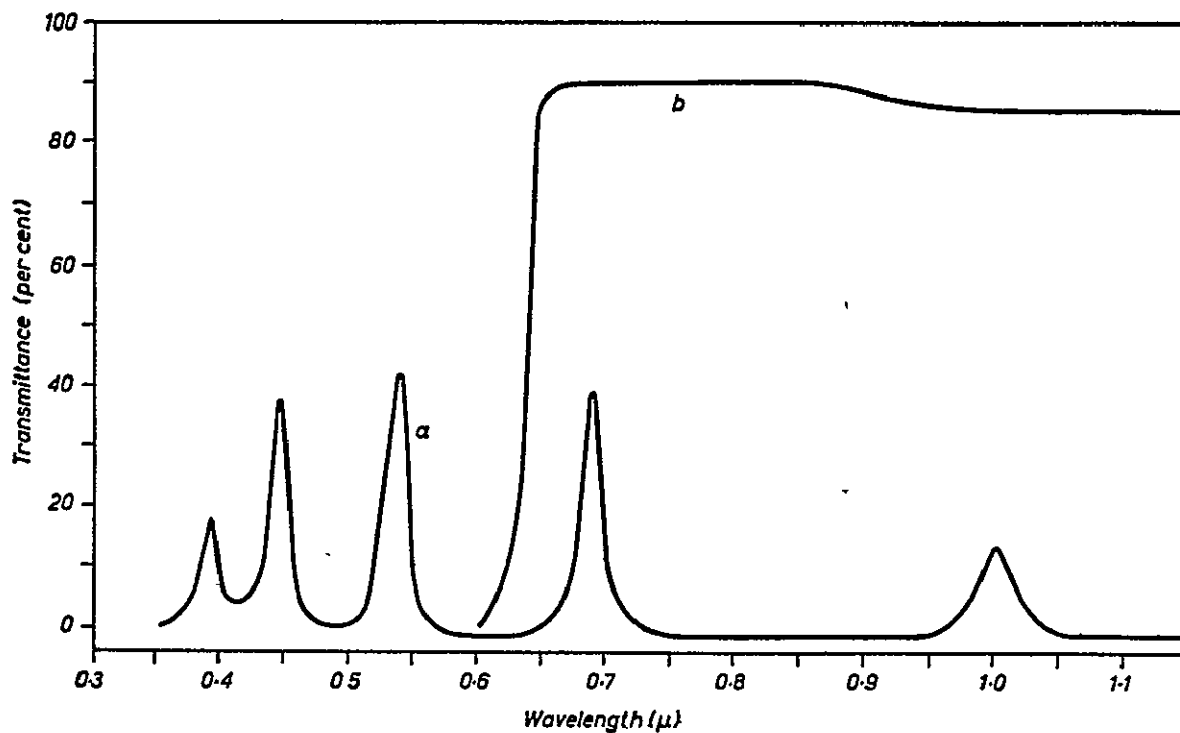


Figure 4.5 Transmittance versus wavelength response of a dielectric layer bounded by two metallic reflecting layers (curve a). Curve b is the transmittance of an absorption filter used to suppress the shorter wavelength responses [Barr and Stroud Ltd., in Macleod, 1969].

reflecting layers are made from dielectric materials.

An all-dielectric multilayer reflector is illustrated in Figure 4.6, and a typical reflectance versus wavelength curve for a multilayer reflector is shown in Figure 4.7. Note that high reflectance occurs only over a narrow band of wavelengths. Only the fundamental reflectance zone is shown, for which all the layers are one quarter of a wavelength thick. High-reflectance zones will also exist at all wavelengths for which the layers are an odd number of quarter wavelengths thick, that is with center wavelengths of $\lambda_0/3$, $\lambda_0/5$, $\lambda_0/7$, etc.

A complete Fabry-Perot filter using all-dielectric multilayer reflectors is shown in Figure 4.8. A typical transmittance versus wavelength response of a Fabry-Perot filter using all-dielectric multilayer reflectors is shown in Figure 4.9.

If the spacer layer is exactly $\lambda/2$ and each of the reflector layers are exactly $\lambda/4$ for normal-incidence radiation, then clearly the wavelength thickness of the layers will deviate from $\lambda/2$ and $\lambda/4$ for radiation at oblique incidence. This means that the transmittance versus wavelength response is a function of the angle of incidence. For collimated radiation the shape of the transmittance curve will be relatively independent of the angle of incidence, only the center wavelength will change. However, in most applications the radiation will not be collimated.

In photometers, the lens and the diameter of the focal plane collection area will determine the angle of view of the instrument. In such a situation, the radiation can arrive over a range of angles of incidence within the angle of view of the instrument. The result is a shift in the effective center wavelength, a broadening

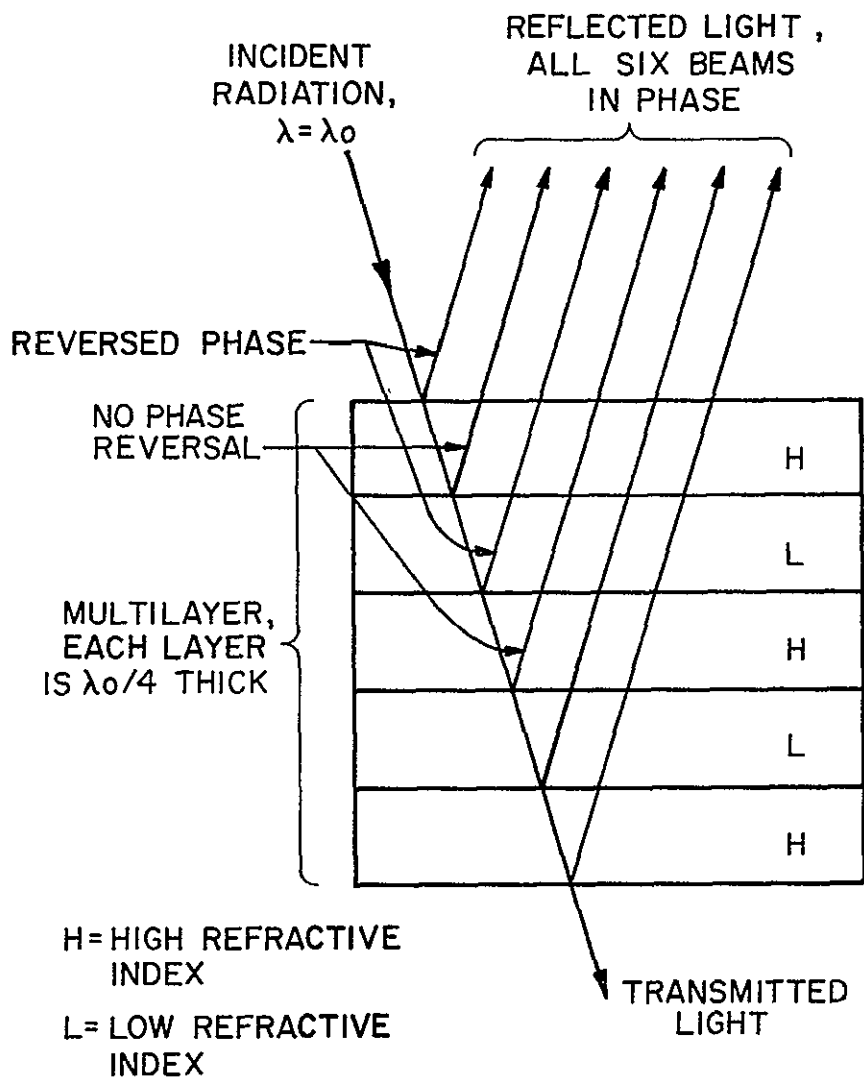


Figure 4.6 A multilayer reflector.

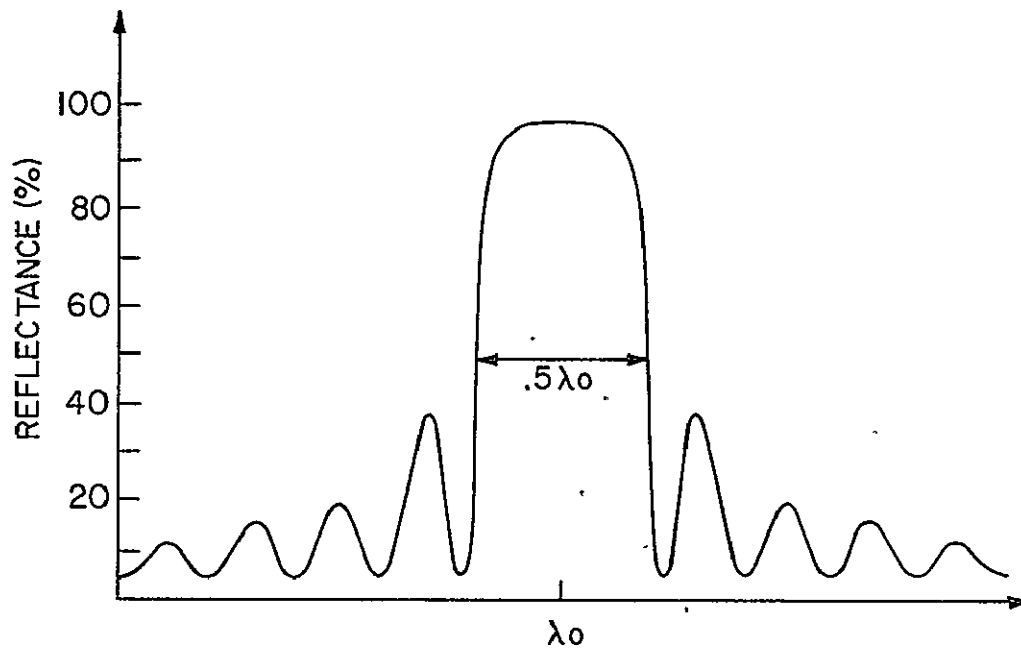


Figure 4.7 A typical reflectance versus wavelength curve for a multilayer reflector [after *MacLeod*, 1969].

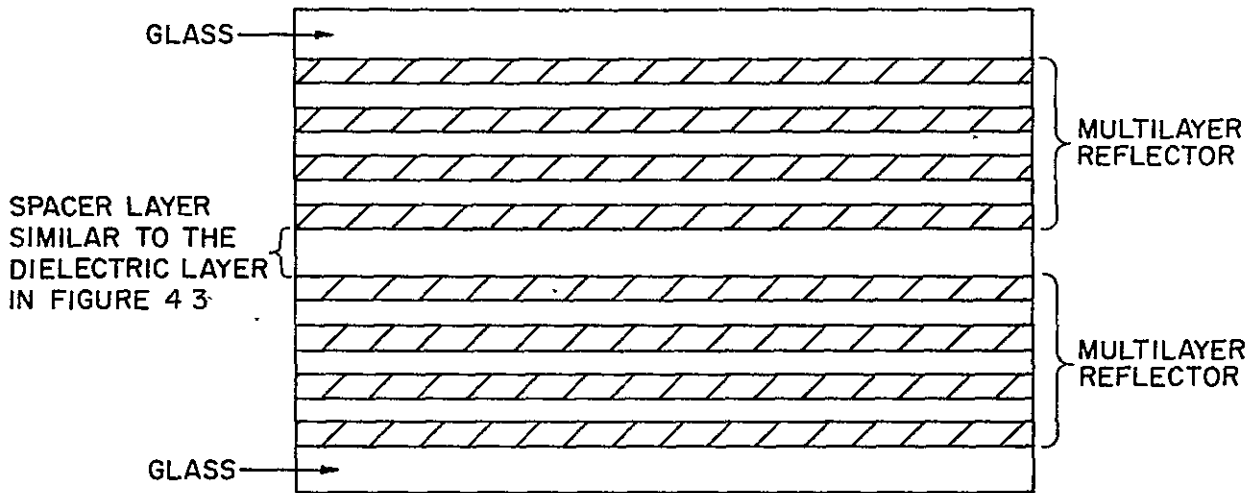


Figure 4.8 A Fabry-Perot filter using all-dielectric multilayer reflectors.

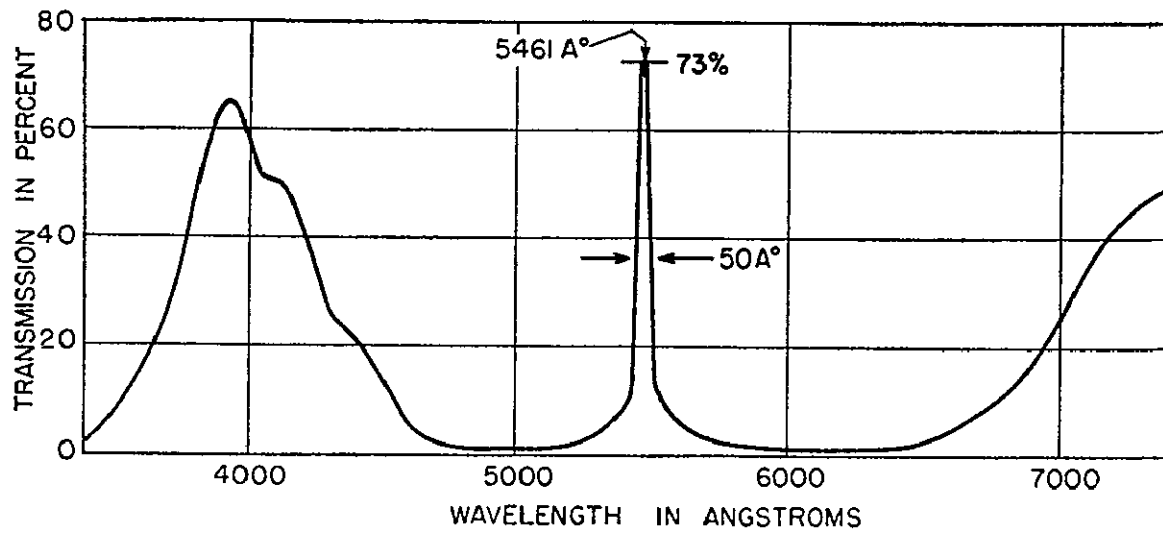


Figure 4.9 A typical transmittance versus wavelength response of a Fabry-Perot filter using all-dielectric multilayer reflectors [Gray, 1957].

of the effective bandwidth, and a lowering of the effective peak transmittance. Therefore, when very narrow passbands are desired, it is important to restrict the instrument angle of view to a value that will not significantly degrade the performance of the filter, and the shift in center wavelength must be considered before specifying the desired filter characteristics.

Also, since the physical dimensions of the filter layers are subject to thermal expansion, the center wavelength is a function of temperature.

Many modifications of the basic Fabry-Perot filter are possible. These include the stacking of several Fabry-Perot filters together to improve the passband shape, and the adding of additional filters to suppress unwanted passbands within the transmittance versus wavelength response.

4.2.2 *Determination of specifications.* The radiation levels to be measured with this instrument are very low (perhaps only a few rayleighs) and the desired radiation, with a band head at 391.4 nm, is concentrated in a very narrow band. There is radiation from other sources than N_2^+ that may cause interference by being in or near the passband of the optical filter. The optical filter characteristics should be specified to maximize the signal-to-noise ratio (interference radiation getting through the filter will here be considered noise). If the bandwidth of the optical filter is made as narrow as is practical and the center wavelength of the filter is specified for a calculated value that will result in a maximum signal transmittance, then a maximum signal-to-noise ratio is assumed.

A first step is to arrive at an accurate model for the relative

intensity of 391.4 nm radiation versus wavelength. Professor V. Degen, University of Alaska, has provided a set of calculated N_2^+ line intensities for several vibrational temperatures. See Figure 2.2 for partially integrated (4 Å triangular halfwidth) synthetic spectra derived from these data.

From this model it is obvious that the shape of the intensity versus wavelength curve varies with temperature. Of the temperatures for which data is provided, 1000 K seemed a realistic value to work with for the purpose of specifying the optical filter characteristics.

Optical filter passband characteristics are carefully measured by the manufacturer and provided with the filter, or the characteristics can be measured in the laboratory. For the purpose of continuing with the analysis and specifying the desired center wavelength and bandwidth, the passband shape is made Gaussian, a reasonable approximation to the actual shape.

A computer program is given in Appendix II.1 that folds the Gaussian-shaped filter transmission function with the 1000 K discrete line spectrum for half-peak-transmittance bandwidths of 5, 10, 20, 30, and 40 Å, and increments the center wavelength from 3880 Å to 3920 Å and plots the resultant curves. Figure 4.10 shows the curves obtained from this program.

By analyzing the results of this calculation, it is possible to determine a curve that displays the optimum center wavelength for a given bandwidth (optimum in terms of maximum energy transmission); it is also possible to determine a curve shown in Figure 4.11 that displays the maximum possible energy transmission for a given bandwidth, assuming the optimum center wavelength and a peak transmittance of 1.0.

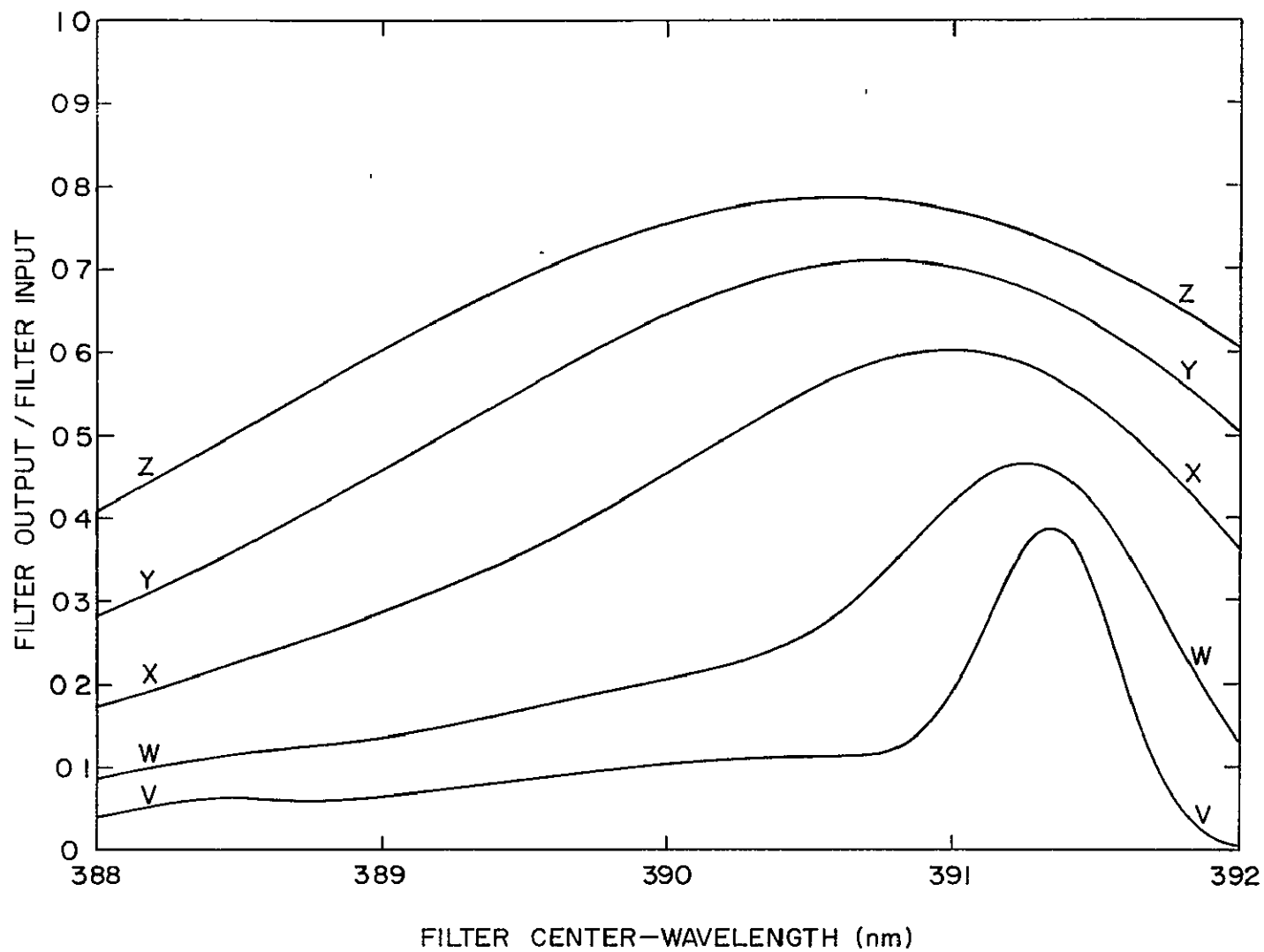


Figure 4.10 Gaussian-shaped filter transmission functions folded with the 1000 K discrete line spectrum. Filter peak transmittance = 1.0. Filter half-peak-transmittance bandwidth: V = 0.5 nm, W = 1.0 nm, X = 2.0 nm, Y = 3.0 nm, Z = 4.0 nm.

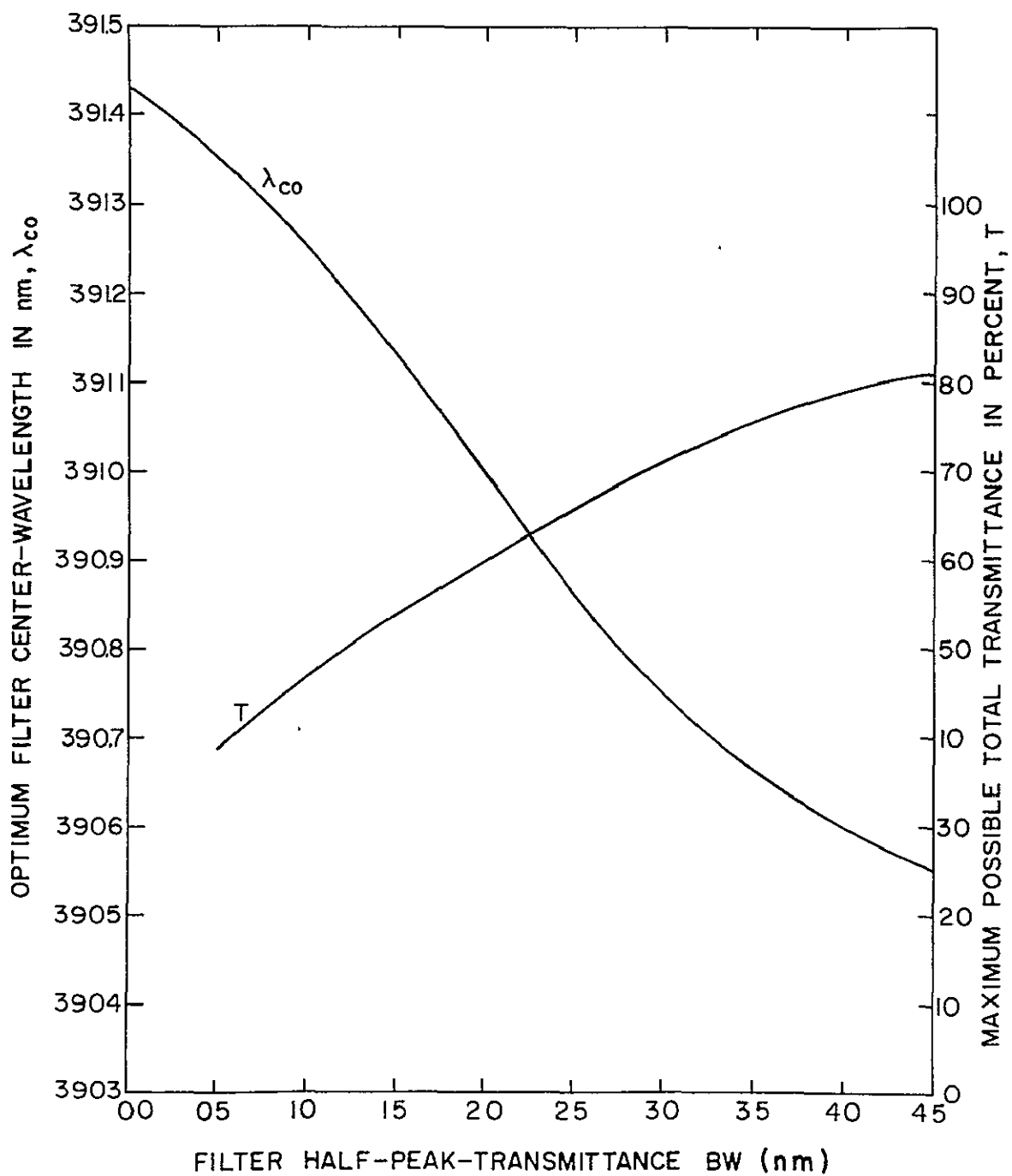


Figure 4.11 Optimum filter center wavelength versus bandwidth, and maximum possible total transmittance versus bandwidth.

Study of Figures 4.10 and 4.11 leads to specifications for the filter center wavelength and bandwidth. There are, however, additional considerations: 1) there are practical manufacturing limits concerning filter bandwidth, 2) generally the more narrow the bandwidth the smaller the peak transmittance, 3) the more narrow the bandwidth the more critical is the center wavelength (see Figure 4.10), and 4) the more narrow the bandwidth the more sensitive will be the instrument output to variations in filter temperature. That last consideration requires some elaboration.

Although it varies with manufacturing technique, materials, wavelengths involved, etc., the change in center wavelength with temperature for filters of this type is generally in the range from 0.01 to 0.02 nm/°C. As an example, suppose the temperature coefficient is 0.02 nm/°C and it is desired that the filter operate satisfactorily over a temperature range of from -7 °C to 32 °C and have a bandwidth of 0.5 nm. From Figure 4.11, the optimum center wavelength would be 391.35 nm. Let this be the center wavelength at the center of the temperature range, 12.5 °C. Then, over the desired temperature range the center wavelength would vary from 390.96 nm to 391.74 nm. From Figure 4.10 the energy transmission would vary by a factor of 4.8 and could have a very undesirable effect on the signal-to-noise ratio when the actual center wavelength had deviated from the optimum. Therefore, unless temperature control is to be employed, it is undesirable to use a filter with a bandwidth as narrow as 0.5 nm. For this reason alone (the extreme sensitivity of instrument output to variations in filter temperature for extremely narrow bandwidth filters), an extremely narrow bandwidth filter is undesirable for this application (at least at the present

state-of-the-art of optical filter design). If temperature control were to be employed or extremely small temperature coefficients were possible, and assuming for the moment that a filter could be manufactured with extremely narrow bandwidth, e.g., 0.5 nm, extremely close center wavelength tolerance, good peak transmittance, etc., then such a filter would be desirable for this application, since the loss of maximum possible filter transmittance by going to an extremely narrow bandwidth filter (see Figure 4.11) would be small compared to the greater suppression of interference radiation.

Since it is desirable to avoid the complications of filter temperature control, and considering the other above-mentioned factors and also commercial availability, a bandwidth of 1.2 nm was decided upon. The optimum center wavelength is then 391.2 nm.

Although a bandwidth of 1.2 nm results in an instrument output that is far less dependent upon filter temperature than a much narrower bandwidth, a temperature dependence is still present and therefore the filter temperature must be measured. The filter temperature monitoring circuit will be considered in a later chapter.

As mentioned earlier, the bandwidth and center wavelength of an optical filter are dependent upon the cone angle of view of the instrument. Therefore, if the cone angle of view is known or decided upon before the optical filter is ordered, the center wavelength and bandwidth can be specified for the stated cone angle of view. Using this method, the optical filter characteristics will be properly matched to the rest of the instrument. A full cone angle of 10° was decided upon as a good compromise between increasing signal intensity and decreasing filter performance.

In summary, the desired filter characteristics for a Gaussian-shaped passband are, for a full cone angle of view of 10° : a center wavelength of 391.2 nm and a bandwidth of 1.2 nm; high peak transmittance; very high blocking outside the passband; and a low center wavelength temperature coefficient.

The specifications of the optical filter, established in discussions with a manufacturer, are presented in Table 4.3.

4.3 Lens

The diameter of the photocathode of the channel multiplier, d , is 5 mm. The full cone angle of view of the instrument, 2θ , was earlier decided upon to be 10° , or 0.17453 radians. The focal length, F , of the lens may be found by the following relation:

$$F = \frac{d}{2\theta \text{ (in radians)}}$$

If the entire diameter of the photocathode is utilized, then the required focal length is found to be, by the above relation,

$$28.65 \text{ mm}$$

Since the collection area of the instrument is directly related to the diameter of the lens, it is desirable to have a large diameter. Therefore, the desirable lens characteristics are as follows:

- a) be made of a material that will pass 391.4 nm with little attenuation,
- b) have a focal length that satisfies the following inequality,

$$F \leq 28.65 \text{ mm}$$

but be close to the maximum allowable, c) have a large diameter for good instrument sensitivity. The lens selected was an Oriel model number A-17-141-10. Important characteristics of the lens are

Table 4.3

Specifications of the Optical Filter

Manufacturer: Barr Associates, Inc.

Diameter: 31.8 mm (1.25 inches)

The following specifications refer to a temperature of 10°C and a field of view (total angle) of 10 degrees:

1. Effective center wavelength: 391.2 ± 0.1 nm
2. Peak transmittance: not less than 20%
3. Temperature coefficient of the center wavelength: not greater than 0.012 nm/°C
4. Effective bandwidth at 50% of peak transmittance: 1.2 ± 0.2 nm
5. Approximate width of the filter:
 - at 10% of peak transmittance, 2.4 nm
 - at 1.0% of peak transmittance, 4.2 nm
 - at 0.1% of peak transmittance, 7.2 nm
6. Transmittance outside the passband: not greater than 0.001% of peak transmittance, from 1 μ m to X-ray.

presented in Table 4.4.

4.4 *Window*

The purpose of the window is to protect the optical filter, provide thermal insulation for the optical filter, and pass, with little attenuation, 391.4 nm radiation on to the filter. In order to serve effectively as a thermal insulator, the window should be relatively thick. In order to not interfere with the instrument angle of view and to facilitate construction of the optical assembly, the window should have a diameter considerably greater than the optical filter. The window selected was an Oriel model number A-45-102-0. Important characteristics of the window are presented in Table 4.5.

4.5 *Detector Assembly*

A requirement of the detector assembly is to provide a housing for the window, optical filter, lens, and channel multiplier. It should do this in such a way that assembly and disassembly is easily accomplished. It must also provide an effective way of connecting the thermistor of the filter temperature monitor circuit to the optical filter. In addition, the system check LED must be mounted in the detector assembly.

In addition to the above, the detector assembly must include a focal plane stop. The focal plane stop performs the following functions:

- a) determines the distance between the lens and the channel multiplier-- the end of the channel multiplier rests against the focal plane stop,
- b) in conjunction with the lens, the diameter of the hole in the focal plane stop determines the angle of view of the instrument. The diameter of the hole in the focal plane stop, D , may be solved for as follows:

$$D = (2\theta)(F)$$

Table 4.4
Important Characteristics of the Lens

manufacturer:	Oriel Corporation of America
model number:	A-17-141-10
material:	crown glass
transmission at 391.4 nm:	$\geq 85\%$
shape:	plano-convex, aspheric, molded
surfaces:	fire polished
diameter:	27 mm
focal length:	20 mm

Table 4.5
Important Characteristics of the Window

manufacturer:	Oriel Corporation of America
model number:	A-45-102-0
material:	high quality plate glass
transmission at 391.4 nm:	$\geq 80\%$
flatness:	both sides flat to 1 wave (at 546.1 nm) over 1 inch diameter
parallelism:	30 seconds or better
surfaces:	standard optical polish
thickness:	6.3 mm ($\frac{1}{4}$ inch)
diameter:	50.8 mm (2.0 inches)

where

2θ = desired full angle of view of the instrument in radians

and

F = the focal length of the lens

therefore

$$D = (0.1745)(20 \text{ mm}) = 3.5 \text{ mm}$$

Figure 4.12 illustrates the detector assembly.

Figure 4.13 is a photograph of the optical assembly parts break-down. The optical assembly, as illustrated in Figure 4.12, includes everything in the detector assembly except the channel multiplier and the instrument frame. Upper left, in Figure 4.13, is the lens cap. The lower row of parts, from left to right, is as follows: the retainer ring that holds the window, rubber washer, and optical filter in place; the window, which is partially painted with black enamel; the rubber washer; the optical filter (below the optical filter are shown the thermistor assembly and LED); the lens; and the focal plane stop assembly, which also holds the lens in place and provides the threads by which the optical assembly is screwed into the instrument frame.

Upper right is the optical housing: on the right side the terminals that connect to the LED can be seen; on the lower edge the hole that the thermistor assembly screws into can be seen; the lens is inserted from the bottom with the focal plane stop assembly following it; the filter, rubber washer, and window are inserted from the top, the retainer ring is then placed over the window and fastened to the optical housing.

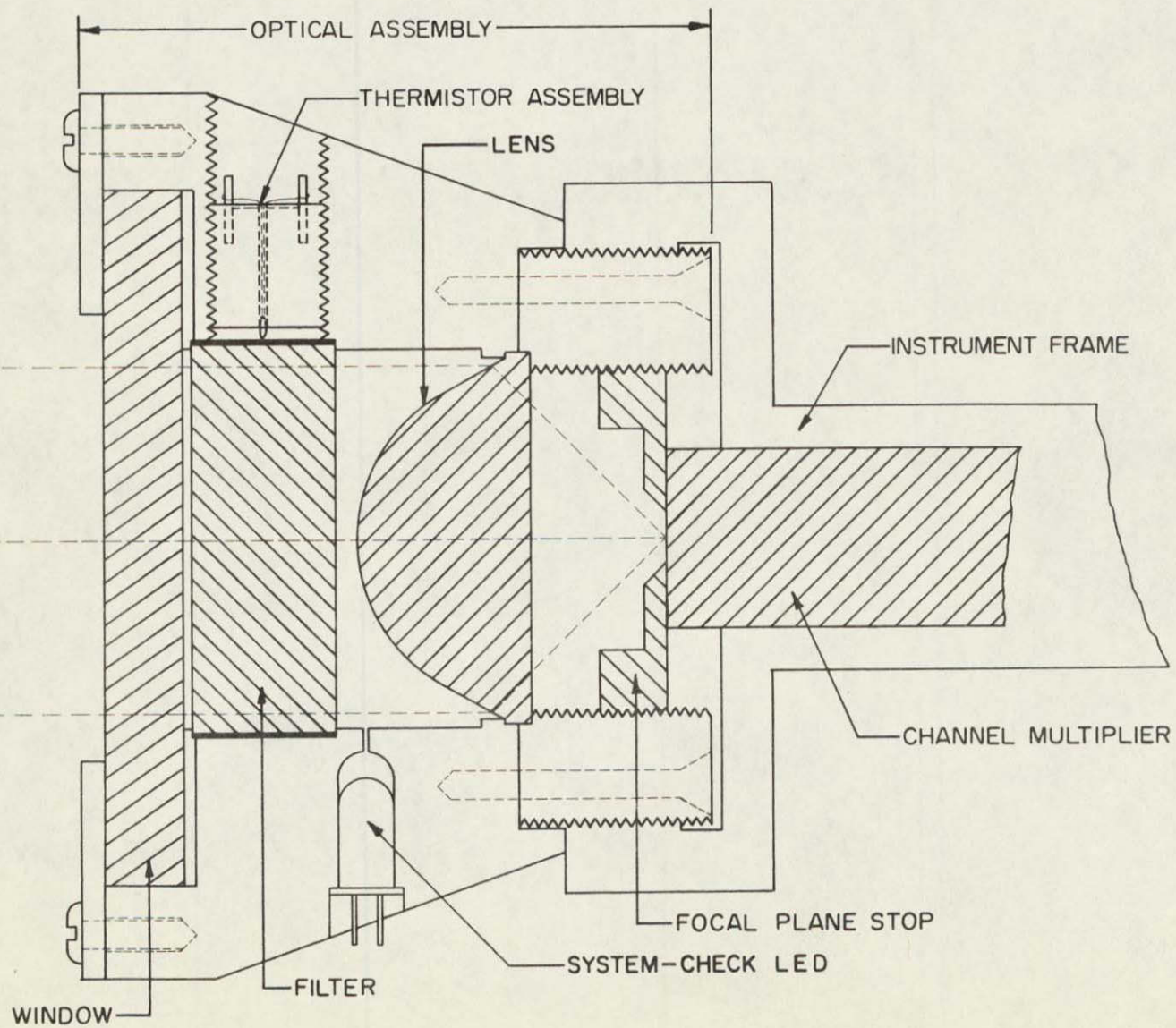


Figure 4.12 Detector assembly.

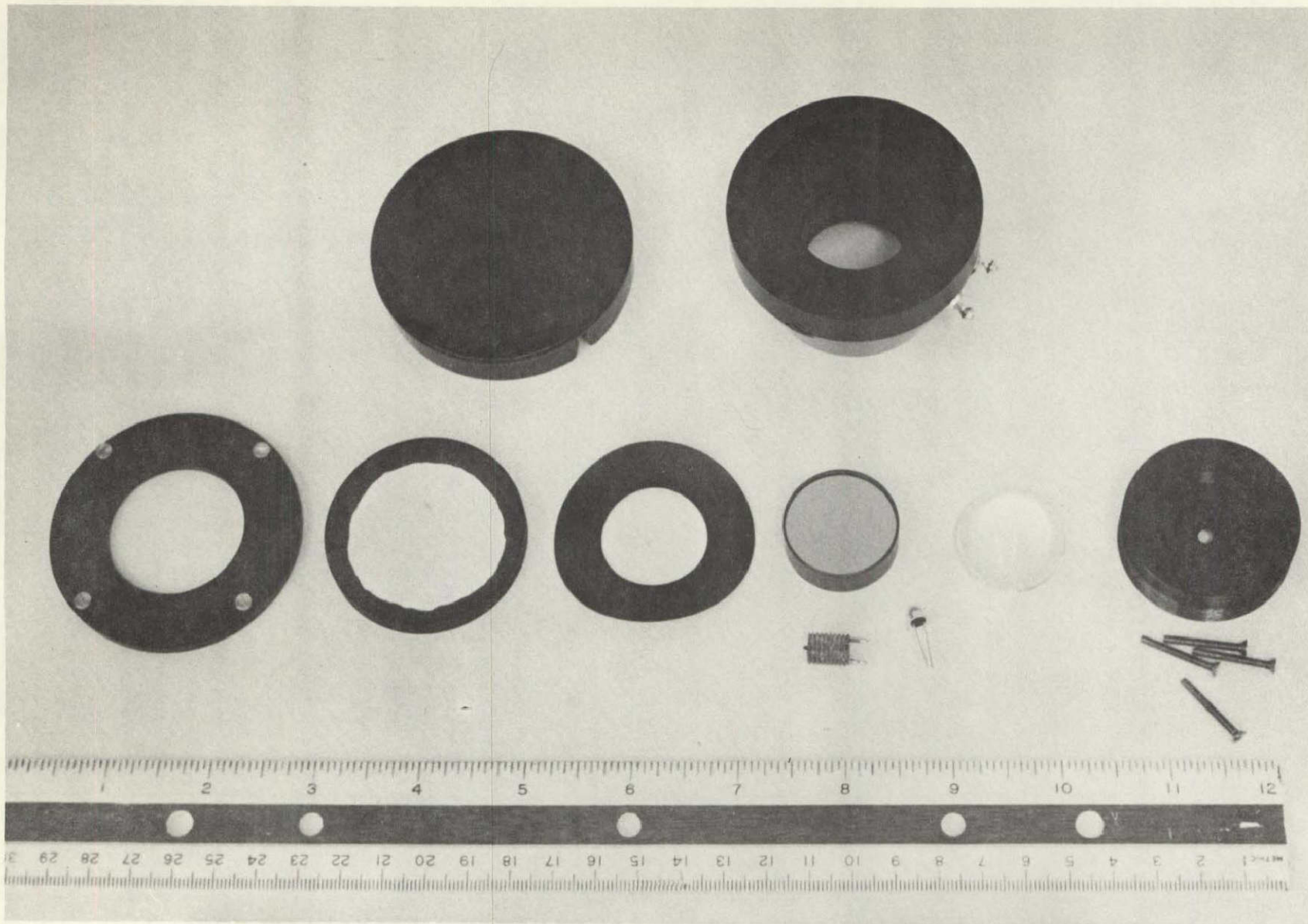


Figure 4.13 Optical assembly parts breakdown.

ORIGINAL PAGE IS
OF POOR QUALITY

4.6 *Adjustments*

The only adjustment in the photometer detector is the distance between the lens and the focal plane stop. It is assumed that the focal length of the lens is essentially the same at 391.4 nm as it is at visible wavelengths. The adjustment can be made as follows.

With the optical assembly removed from the instrument frame and the optical filter removed from the optical assembly:

- a) tape a small piece of thin, hard, translucent white paper over the hole in the focal plane stop, the side that the face of the channel multiplier rests against
- b) on a bright sunny day, adjust the position of the focal plane stop to give a sharp image on the white paper when viewing a distant object through the optical assembly
- c) fix the position of the focal plane stop using paint or varnish

5. ELECTRONIC CIRCUITS

The purpose of this chapter is to present technical details of the photometer electronic circuits beyond that given in Chapter 3. Circuit schematic diagrams, circuit descriptions, circuit characteristics, trouble-shooting charts, and adjustment procedures are included. The photometer electronic circuits include the pulse preamplifier, pulse processor, and temperature monitors, as well as some other circuits mounted on the frame of the instrument and of the light-emitting diode, which is mounted in the optical assembly. All measured characteristics presented in this chapter are for the serial #1 unit.

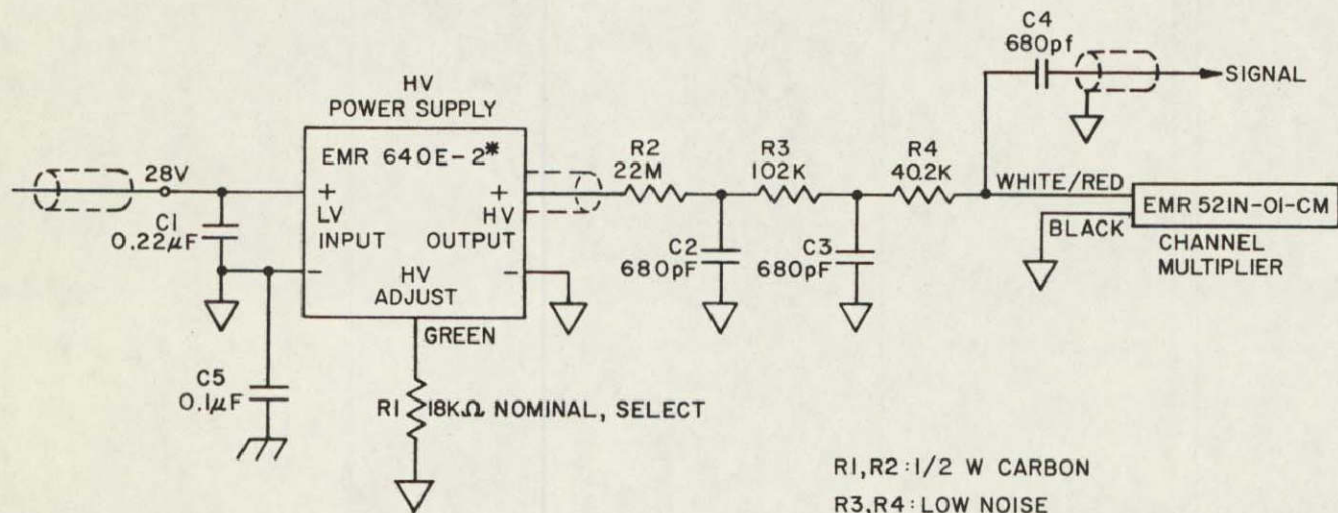
5.1 *Detector Electronics*

The detector electronics comprise the channel multiplier, high voltage power supply, and high voltage filter. The schematic diagram is shown in Figure 5.1. The value of R1 is selected to give the channel multiplier a gain of 10^6 .

Although the output ripple of the high voltage power supply is quite low, it needs additional filtering, otherwise the pulse preamplifier and following circuits will count power supply ripple pulses as well as the desired signal. R2, R3, C2, and C3 accomplishes the required additional filtering.

R4 serves as a load resistor for the signal, and because it is much larger than the input impedance of the pulse preamplifier, it has negligible effect on the circuit operation. R3 and R4 are both low noise resistors to help minimize the inherent noise in the circuit.

Figure 5.2 shows the high voltage power supply and associated circuitry with the coverplate removed. The channel multiplier inserts into a hole which goes through the instrument frame from lower left to



R1,R2:1/2 W CARBON

R3,R4: LOW NOISE

C1:50V

C2-C4:CENTRALAB DD60-681

*WITH POSITIVE HV OUTPUT MODIFICATION

Figure 5.1 Detector electronics schematic diagram.

ORIGINAL PAGE IS
OF POOR QUALITY

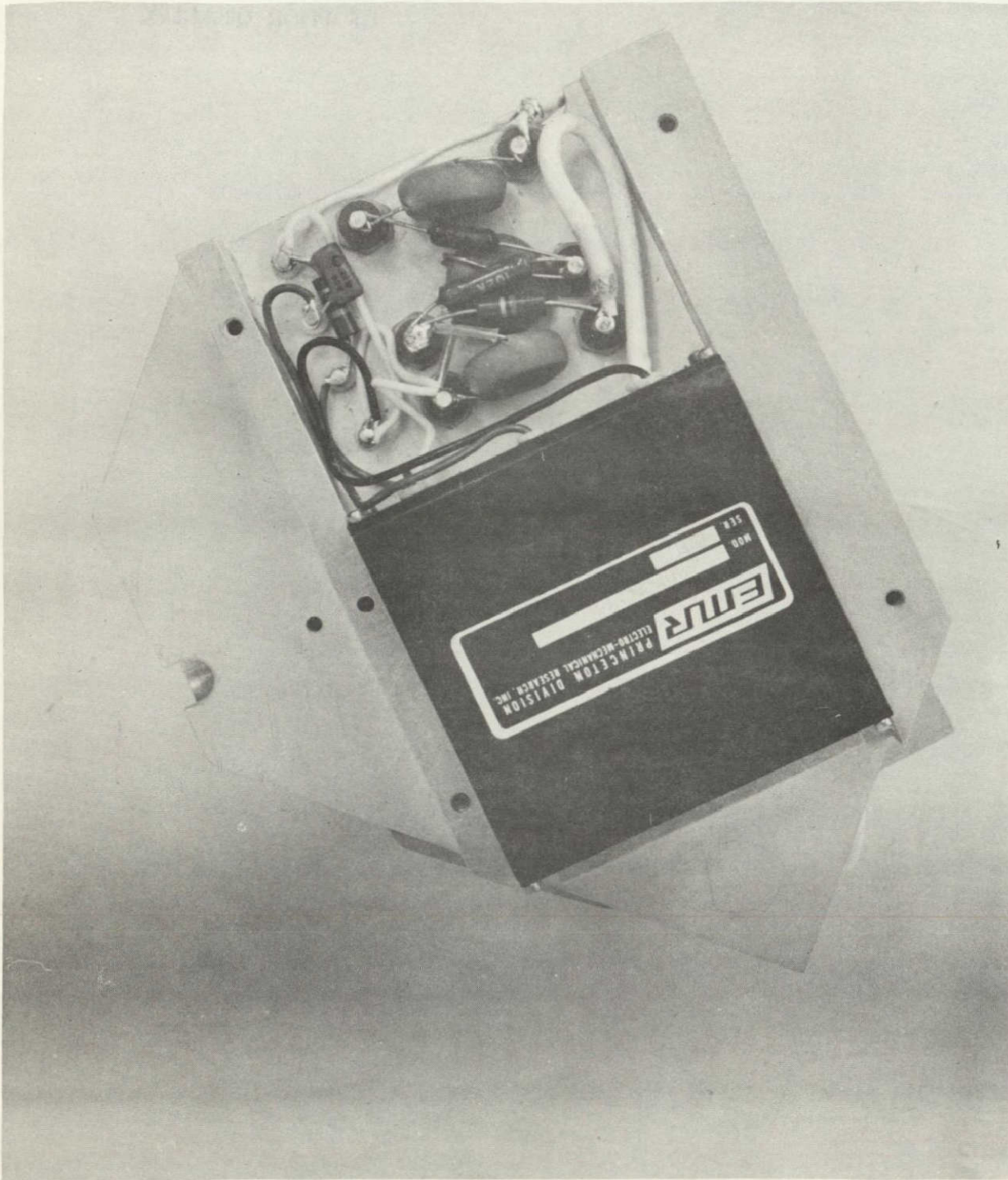


Figure 5.2 High-voltage power supply associated circuitry physical construction.

right. A notch in the edge of the hole where the leads come through is visible on the left (this unit is only partially constructed). The signal output lug is shown upper right. The high voltage output lug for the channel multiplier is shown upper center. The high voltage supply is also seen in Figure 5.3. Illustrated from left to right, in Figure 5.3, is an edge of the pulse processor circuit board, an edge of the pulse preamplifier circuit board, the high voltage power supply and associated circuitry, and the +28 V to -28 V converter.

5.2 Pulse Preamplifier

5.2.1 *Circuit description.* The circuit schematic diagram is shown in Figure 5.4. The output charge pulses of the channel multiplier are capacitively coupled to the input of the pulse preamplifier. The input impedance may be represented by the input resistance shunted by the input capacitance. The input capacitance is made up of the inherent and stray capacitances of the circuit. The magnitude of the input capacitance is the primary factor that determines the magnitude of the input voltage pulses. Since essentially all of the input charge (q) is dumped into the input capacitance (C_{in}), the magnitude of the input voltage pulse is simply

$$V_{in} \cong \frac{q}{C_{in}}$$

Since the output resistance of the channel multiplier is quite large, the input voltage pulse width is primarily determined by the input time constant: $R_{in} C_{in}$. Therefore, to maintain a narrow input pulse width, the input resistance should not be large. R_1 , R_2 , and R_3 , along with the characteristics of the MC1733L, determine the input resistance. R_1 , R_2 , and R_3 also help determine the voltage gain of the MC1733L and establish its dc operating conditions.

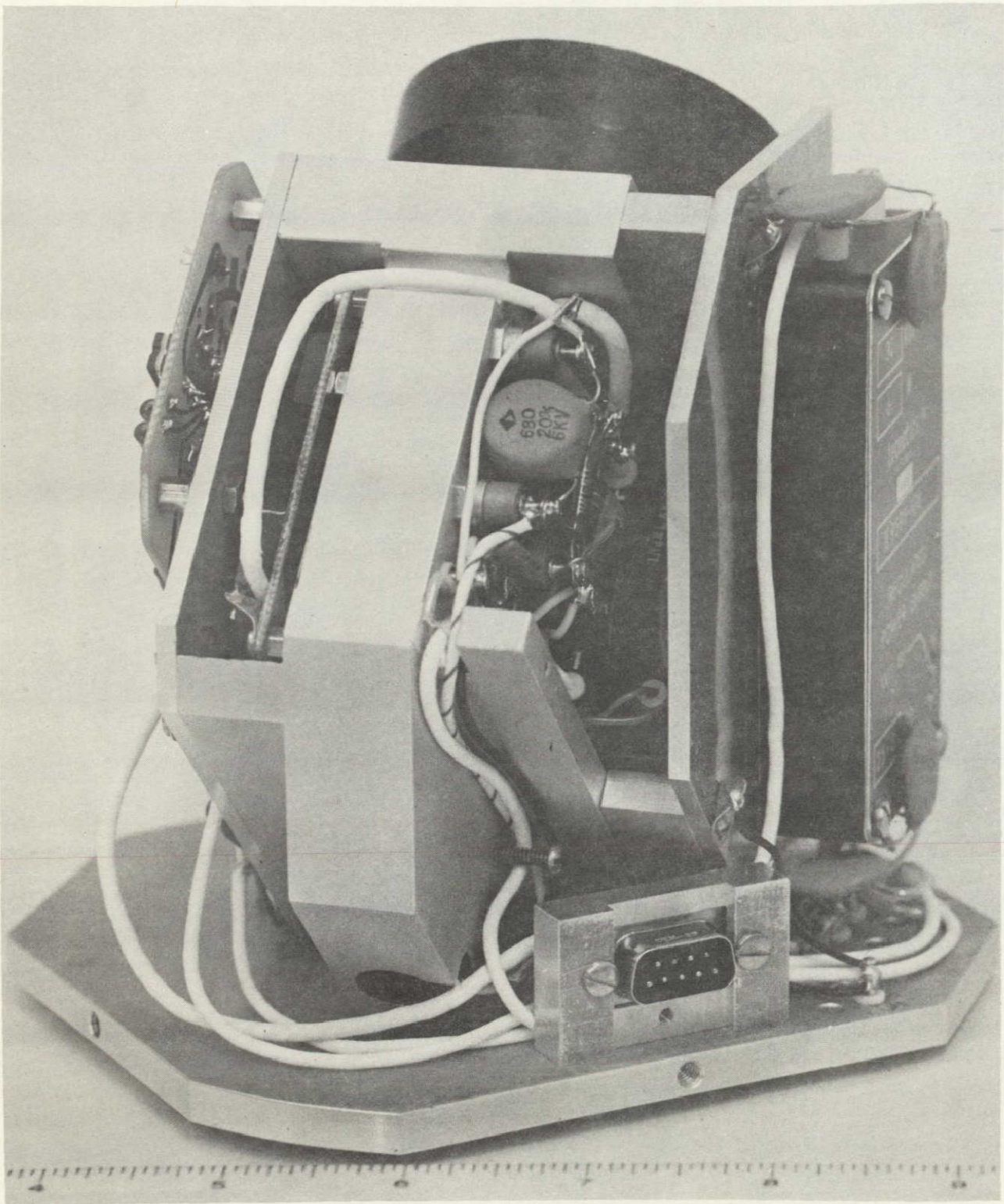


Figure 5.3 Rear view of the completed instrument.

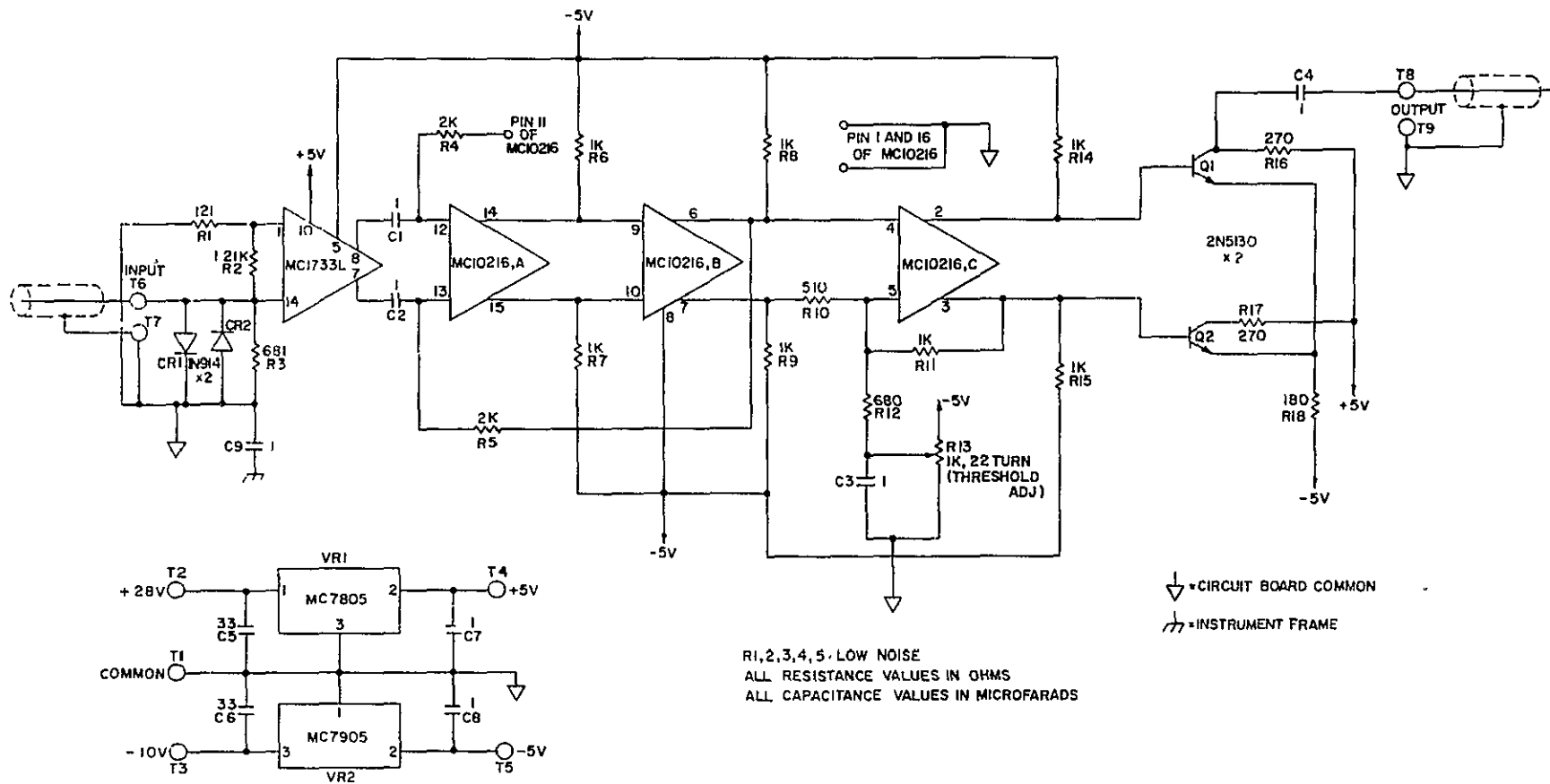


Figure 5.4 Pulse preamplifier schematic diagram.

ORIGINAL PAGE IS
OF POOR QUALITY

The voltage gain from input to pin 7 of the MC1733L is -5. The voltage gain from input to pin 8 of the MC1733L is +5.

CR1 and CR2 help prevent damage to the MC1733L when large spikes may occur on the input, such as when the high voltage is turned on.

The differential output of the MC1733L is applied to pins 12 and 13 of the MC10216. Due to the high gain, there is a significant noise level present at pins 4 and 5 of the MC10216. To prevent this noise from appearing at the output, the threshold adjust potentiometer applies a negative offset voltage to pin 5 which just disables the output stage. Any signal pulse above the noise level will appear at the output. The MC10216 is an emitter-coupled device and the output voltage swing is less than a volt. Q1 and Q2 increase this voltage swing to approximately 4.5 V.

5.2.2 *Characteristics.* Some of the most important characteristics are contained in Table 5.1.

Some important signal waveforms are displayed in Figure 5.5. The input signal was a Hewlett Packard 8002 A pulse generator. The smaller inputs were obtained by feeding the signal through a Kay model 30-0 attenuator. Although the input impedance of the pulse preamplifier is not 50 ohms, the dB steps on the attenuator appear to be quite accurate. The oscilloscope traces were obtained on a Tektronix 7623.

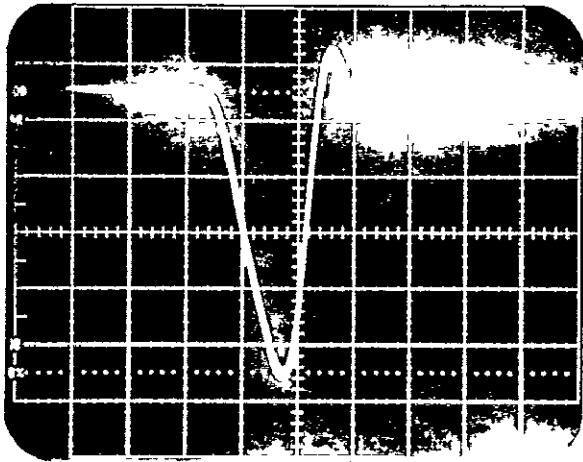
Table 5.2 shows dc measurements. The voltage measurements were made with a Simpson model 460 digital volt-ohm-milliammeter; all voltage measurements were made with respect to the circuit board common. The current measurements were made with a B&K model 280 digital VOM.

Figure 5.6 shows the pulse preamplifier mounted in the instrument frame. The optical assembly screws into the left side of the frame.

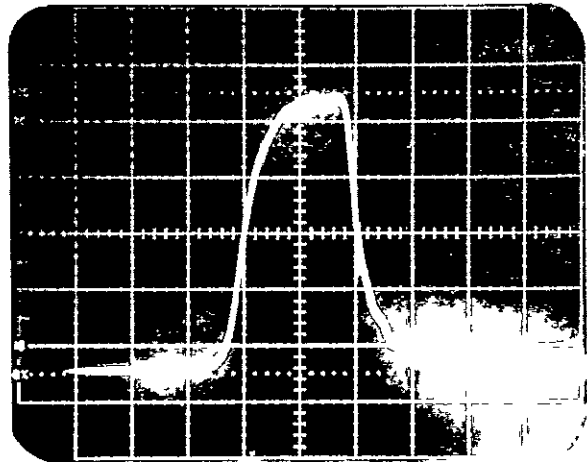
Table 5.1

Pulse Preamplifier Measured Characteristics

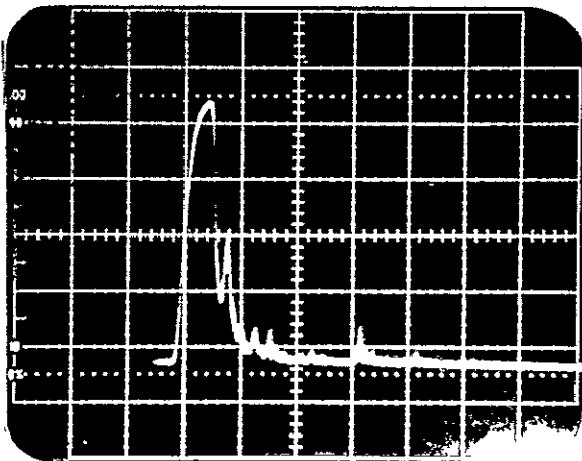
input impedance (measured on an hp 4815A vector impedance meter at 10 MHz)	$380\Omega \angle -24^\circ$, or 416Ω shunted by 17 pF (includes approximately 4 inches of RG-188 A/U cable)
voltage gain from input to output (small input)	-1000
output amplitude	4.5 V
minimum input amplitude for proper system operation	1.3 mV
output pulse width at 50% points (input pulse width = 23 ns at 50% points)	40 ns (500 mV input) 30 ns (5mV input)



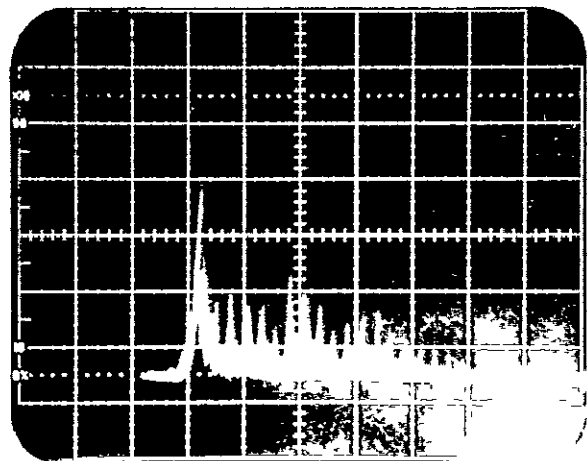
(a)



(b)



(c)



(d)

Figure 5.5 Pulse preamplifier input and output waveforms: (a) input: 20 ns/cm; (b) output: 1 V/cm, 20 ns/cm (input: 500 mV); (c) output: 1 V/cm, 50 ns/cm (input: 5 mV); (d) output: 0.5 V/cm, 50 ns/cm (input: 1.25 mV).

Table 5.2

Pulse Preamplifier DC Measurements

Pin #	MC1733L	MC10216
1	-1.7 mV	0
2	N.C.	-0.75 V
3	-0.82 V	-1.7 V
4	-0.72 V	-1.3 V
5	-5.1 V	-1.8 V
6	N.C.	-1.3 V
7	2.4 V	-1.2 V
8	2.4 V	-5.1 V

Pin #	MC1733L	MC10216
9	N.C.	-1.2 V
10	5.2 V	-1.2 V
11	-0.72 V	-1.3 V
12	-0.81 V	-1.3 V
13	N.C.	-1.3 V
14	-5.4 mV	-1.2 V
15		-1.2 V
16		0

	Q ₁	Q ₂
E	-1.60 V	-1.6 V
B	-0.75 V	-1.7 V
C	-0.40 V	5.2 V

Pin #	VR1	VR2
1	28.2 V	0
2	5.17 V	- 5.11 V
3	0	-10.4 V

wiper arm of R₁₃: -2.61 V

28 V input current: 35 mA

-10 V input current: 87 mA

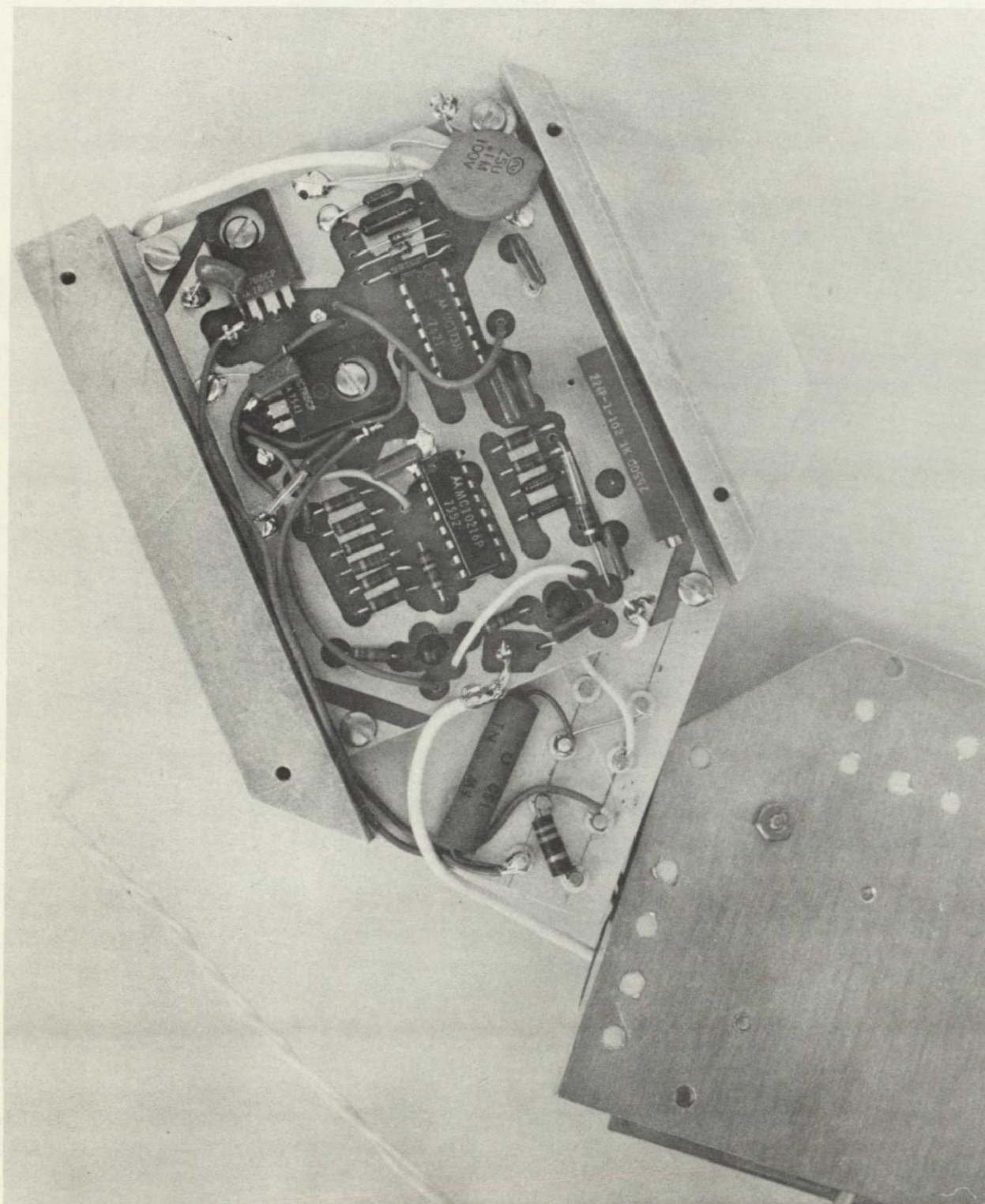


Figure 5.6 Pulse preamplifier physical construction.

The back of the pulse processor mounting plate is shown in the lower right of the photograph. The signal from the channel multiplier comes in through the coaxial cable shown along the top edge of the circuit board. The output signal to the pulse processor goes through the coaxial cable at the bottom of the circuit board. The threshold adjust potentiometer is visible on the circuit board.

5.3 *Pulse Processor*

5.3.1 *Circuit description.* The circuit schematic diagram is shown in Figure 5.7. The positive output pulses of the pulse preamplifier are applied to the input of the pulse processor. Q1 functions as a pulse amplifier biased in the active region, whereas Q2 is normally off. The negative pulses appearing at the collector of Q1 saturate Q2 so that large positive pulses appear at its collector. D1 prevents the base circuit of Q2 from acting as a clamper by enabling the voltage across C1 to remain relatively constant even at high count rates. Q1 and Q2 provide further amplification and thereby improve the sensitivity of the instrument. Q1 and Q2 also provide some pulse stretching to insure reliable triggering of the following monostable multivibrator, of which the minimum input pulse-width specification is 50 ns. The input of the 54121, pin 5, includes a diode with its anode connected to common. As a result, when Q2 is off, the voltage at pin 5 is only slightly negative. When a pulse occurs Q2 turns on and the voltage at pin 5 goes in a positive direction. When the voltage at pin 5 exceeds the positive-going threshold of the device, the monostable triggers. The output of the 54121, pin 6, is approximately 4 V, and its duration is approximately 90 ns as determined by R9 and C4.

The output of the monostable is connected to the input of a 5493

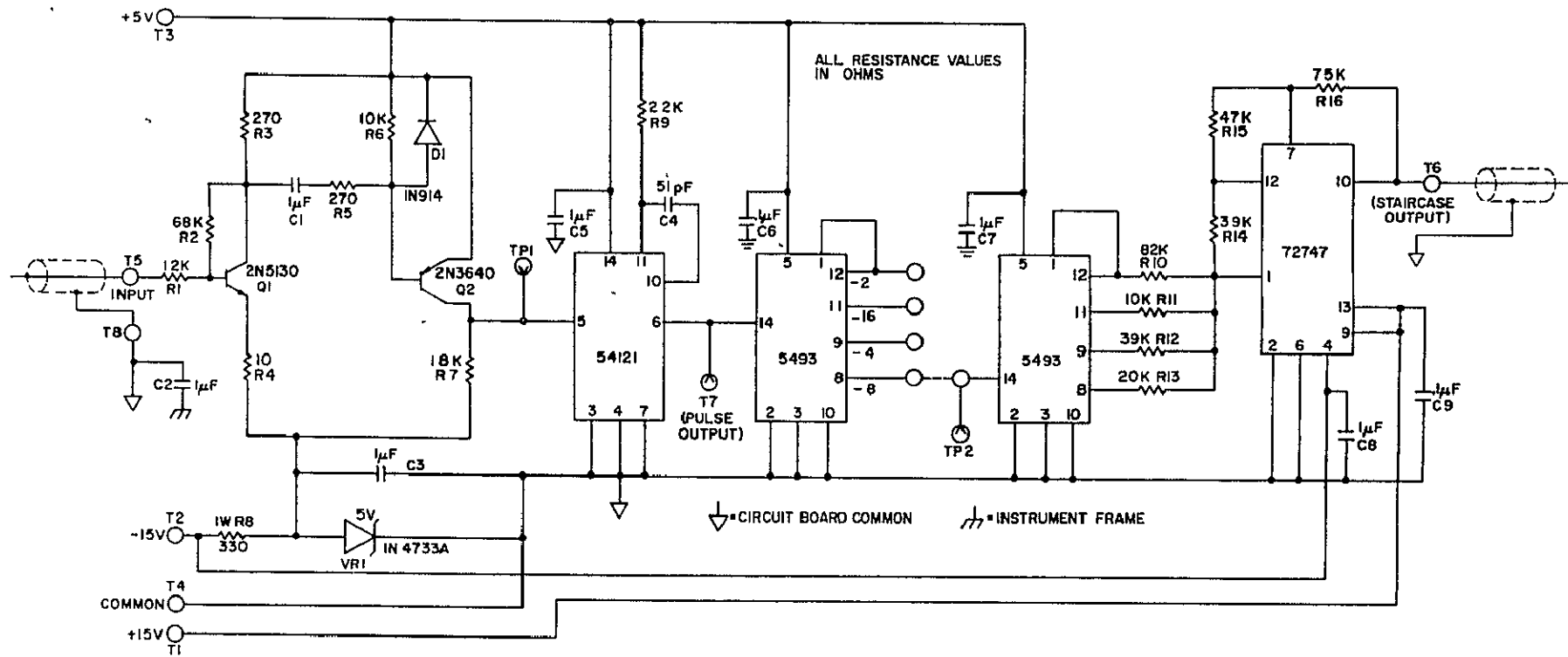


Figure 5.7 Pulse processor schematic diagram.

ORIGINAL PAGE IS
OF POOR QUALITY

which serves as a frequency divider stage. This stage is included to prevent exceeding the bandwidth restrictions of the telemetry channel to be used in the rocket-borne instrumentation system. The amount of frequency division is selectable by a jumper wire, but is initially set at divide-by-8.

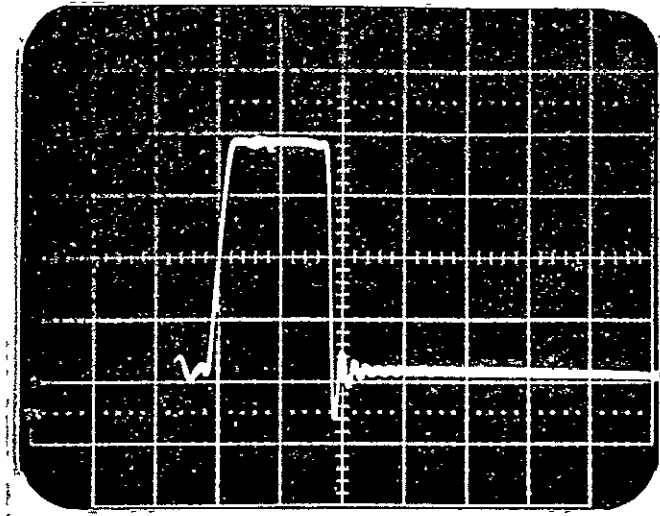
The output of the frequency divider stage is connected to the input of a staircase generator stage (the second 5493 working with the 747). The 747 is a dual operational amplifier. The 5493 functions as a 4-stage binary counter: the least significant digit at pin 12, then pin 9, then pin 8, and the most significant digit at pin 11. The counter outputs are connected through resistors R10 through R13 to the input of the first op-amp. The values of the resistors R10 through R13 properly weight the binary digits.

The output of the first op-amp, pin 12, is connected to the input of the second op-amp, pin 7, through resistor R15. The staircase output appears at the output of the second op-amp and goes from approximately zero volts to +4 volts.

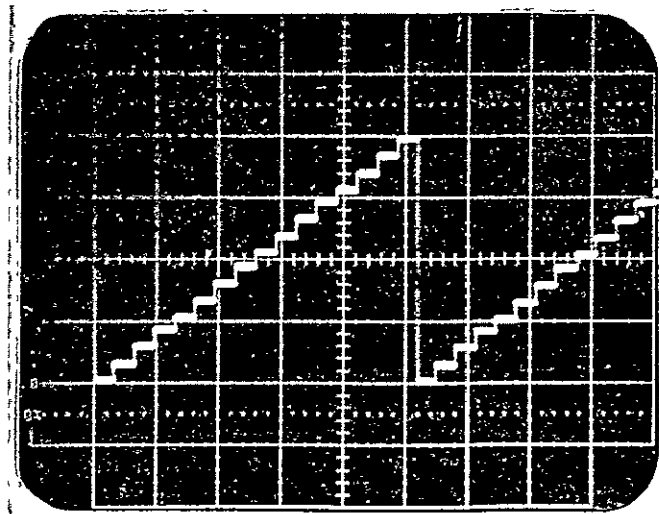
5.3.2 Characteristics. Some of the most important characteristics are contained in Table 5.3.

Figure 5.8 displays the pulse output waveform and staircase output waveform as measured on a Tektronix 7623 oscilloscope. Both waveforms are valid for any input to the pulse preamplifier from 1.3 mV to 500 mV. Note that the staircase displays a count rate of approximately 123 KHz, since each step represents eight counts.

DC measurements are shown in Table 5.4. The measurements were made with a B&K model 280 digital VOM; all voltage measurements were made with respect to the circuit board common.



(a)



(b)

Figure 5.8 Pulse processor output waveforms: (a) pulse output: 1 V/cm, 50 ns/cm; (b) staircase output: 1 V/cm, 0.2 ms/cm.

0-2

Table 5.3

Pulse Processor Measured Characteristics

input impedance (measured on an hp 4815A vector impedance meter at 10 MHz)	980 Ω \angle -52°, or 1590 Ω shunted by 13 pF (includes approximately 4 inches of RG-188 A/U cable)
minimum input amplitude for reliable triggering	250 mV
pulse output amplitude	3.6 V
pulse output pulse-width	90 ns
staircase output amplitude	4.0 V total 0.27 V/step

Table 5.4

Pulse Processor DC Measurements

Pin #	54121	747
1	3.9 V	0
2	N.C.	0
3	0	-15.2 V
4	0	-15.2 V
5	-0.13 V	-15.2 V
6	0.11 V	0
7	0	0

Pin #	54121	747
8	N.C.	-15.3 V
9	0.92 V	14.9 V
10	5.0 V	*
11	0.91 V	N.C.
12	N.C.	*
13	N.C.	14.9 V
14	5.0 V	-15.2 V

* depends on the state of the second 5493

	Q ₁	Q ₂
E	-4.8 V	5.0 V
B	-4.0 V	5.0 V
C	2.0 V	-0.13 V

junction of R_g and VR₁: -4.94 V
voltage on the pins of the 5493 s
depend upon the count-states.

includes both
temperature monitor
circuits

{ 5 V input current: 73 mA
15 V input current: 14 mA
-15 V input current: 41 mA

Figure 5.9 is essentially the same as Figure 5.6 except that the pulse processor mounting plate has been closed over the pulse preamplifier, displaying the physical construction of the pulse processor and optical filter temperature monitor circuit board. The input signal to the pulse processor comes in through the coaxial cable shown at the bottom of the board. The staircase output lug is shown on the right edge of the board--the first lug down from the top. The pulse output lug is shown on the left edge near the top of the board. The optical filter temperature monitor circuit is shown in the lower right-hand corner of the circuit board. The two white wires along the right edge of the circuit board go to the optical filter thermistor assembly. Three power supply regulators are mounted on the pulse processor mounting plate under the circuit board.

5.4 *Temperature Monitors*

5.4.1 *Monitor electronics.* The thermistors used in the temperature monitors are Fenwal GB32P2, whose typical characteristic is shown in Figure 5.10. The circuit schematic diagram is shown in Figure 5.11. The optical filter temperature monitor circuit and the instrument frame temperature monitor circuit are identical. The thermistor, T, in the optical filter temperature monitor is mounted in such a way as to be in thermal contact with the optical filter. The thermistor in the instrument frame temperature monitor is in contact with the instrument frame.

The voltage at pin 3 of the 741 is held at a constant value while the voltage at pin 2 is a function of thermistor resistance. As the temperature of the thermistor increases, its resistance goes down and the voltage at pin 2 goes down, and the voltage at pin 6 goes up.

The value of R3 most greatly affects the value of the output voltage at the maximum temperature that is desired to be measured. Increasing R3

ORIGINAL PAGE IS
OF POOR QUALITY

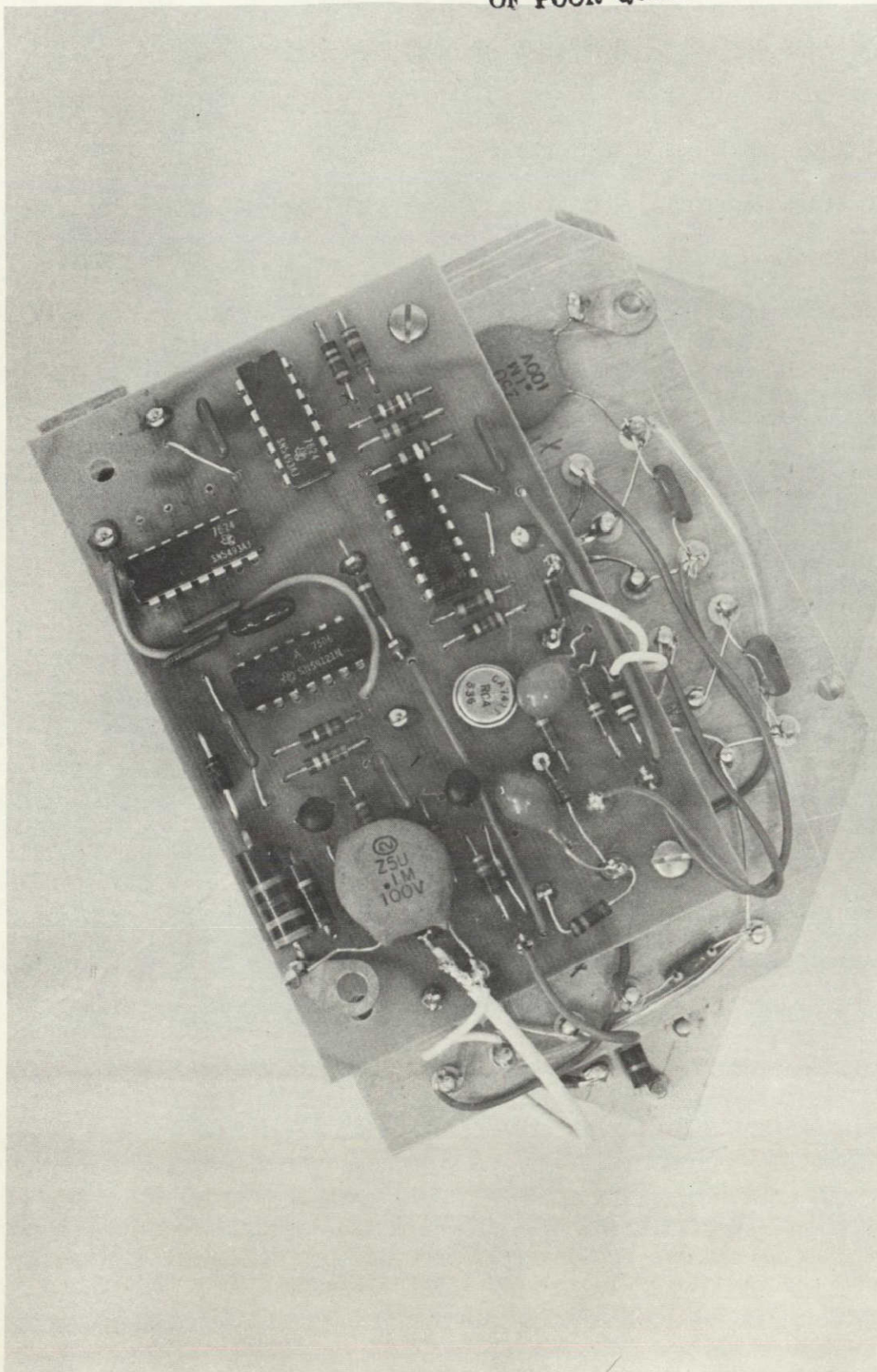


Figure 5.9 Pulse processor physical construction.

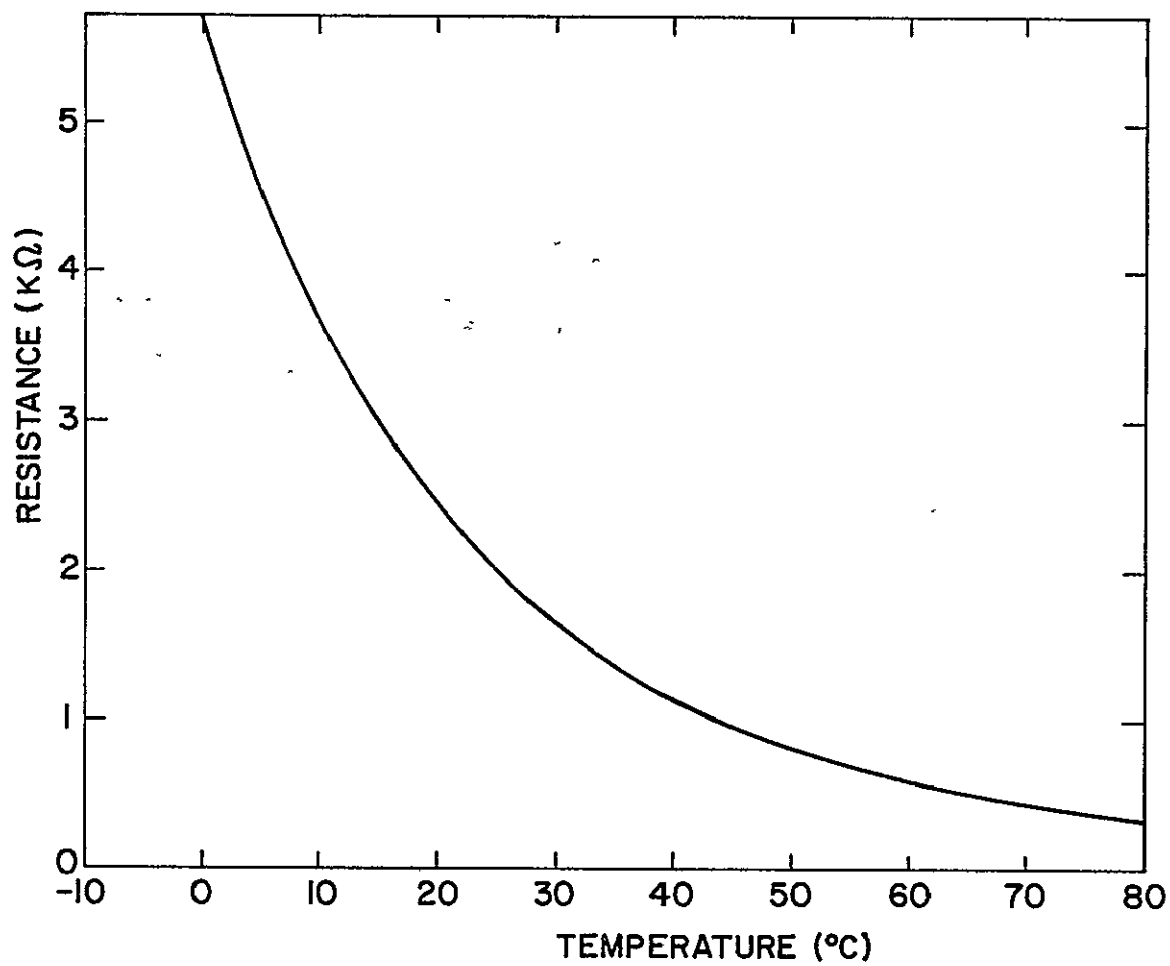


Figure 5.10 Typical characteristics of the thermistor (Fenwal GB32P2).

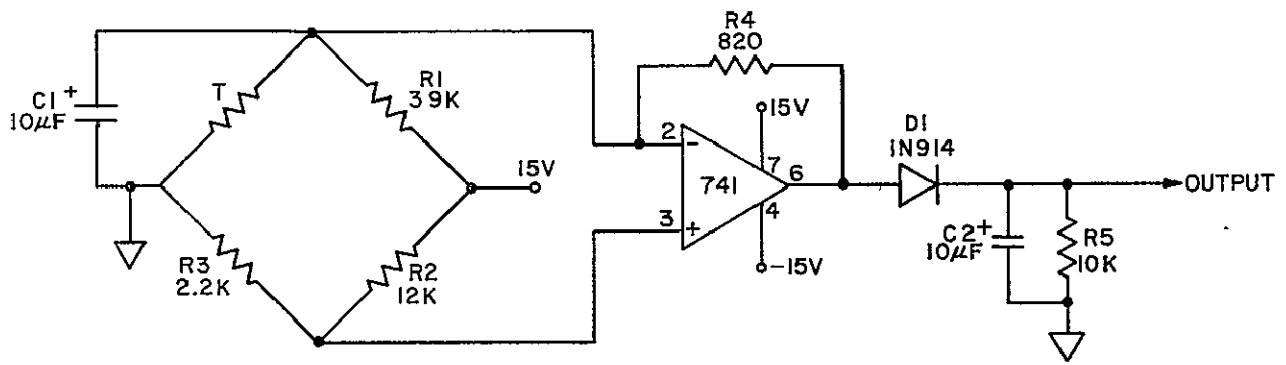


Figure 5.11 Temperature monitor schematic diagram.

will increase the output voltage at a given high temperature.

The value of R4 most greatly effects the value of the output voltage at the minimum temperature that is desired to be measured. Increasing R4 will decrease the output voltage at a given low temperature.

The output voltage of the temperature monitor circuit will be connected to the input of a voltage controlled oscillator in the rocket-borne instrumentation system. The VCO requires that its input voltage be between zero and 5 V. When the instrument is first turned on, and perhaps cold, the voltage at pin 6 of the 741 may be negative. The diode, D1, prevents this negative voltage from being applied to the input of the VCO. Before the instrument is used for any measurements, it must have sufficient time to warm up and reach thermal equilibrium, and by that time the voltage at pin 6 of the 741 will be positive.

Let T' be the temperature that causes the output voltage to just become greater than zero, and let T'' be the temperature that causes the output voltage to become the maximum allowable, 5 V. By properly selecting the values of R3 and R4 a wide range of values for T' and T'' are possible. For this application a temperature range of 15°C to 57°C was selected.

5.4.2 *Calibration.* Tests show that it takes three to four hours for the temperatures of the optical filter and the instrument frame to stabilize after the instrument is turned on. With such a long thermal lag involved it would be very desirable to calibrate the temperature monitors by controlling the temperature of the thermistors alone, while the temperature of the instrument itself would be allowed to remain constant. In order to do this it is necessary to show that the temperature monitor circuits excluding the thermistors are relatively insensitive to thermal changes.

The test was conducted as follows. Both thermistors were replaced by

619 Ω precision resistors connected to the circuit boards through long wires. The entire instrument excluding the precision resistors was placed in a temperature chamber. The instrument was turned on and allowed to warm up for four hours with the temperature chamber off and the door open. The temperature chamber door was then closed and the chamber cooled to -5°C . After $2\frac{1}{2}$ hours the temperature monitor circuits output voltages had stabilized to;

filter temperature output voltage: 2.33 V

frame temperature output voltage: 2.22 V

The temperature chamber was then warmed to 55°C . After 3 hours the temperature monitor circuits output voltages had stabilized to:

filter temperature output voltage: 2.47 V

frame temperature output voltage: 2.32 V

The temperature chamber door was then opened and the instrument frame temperature was measured to be 145°F (63°C).

The total change in filter temperature output voltage was 140 mV; the total change in frame temperature output voltage was 100 mV. It was previously found (not reported in this paper) that the average sensitivity of the temperature monitors is approximately $75\text{ mV}/^{\circ}\text{C}$. Therefore, 140 mV represents an equivalent temperature change or error of approximately 1.9°C , and 100 mV represents an equivalent temperature change or error of approximately 1.3°C . If the temperature monitor circuits are calibrated with the instrument ambient temperature at 25°C (midway between -5°C and 55°C), then an error of $\pm 1^{\circ}\text{C}$ may be expected in temperature measurements due to the thermal sensitivity of the temperature monitor circuits excluding the thermistors.

As mentioned in Chapter 4, typical temperature coefficients for the

center wavelength of optical filters of the type used here are from $0.1 \text{ \AA}/^{\circ}\text{C}$ to $0.2 \text{ \AA}/^{\circ}\text{C}$. Therefore, a 1°C error in filter temperature should result in no more than 0.2 \AA error in center wavelength.

Of course, other sources of error will contribute so that the total error in temperature measurements will be greater than $\pm 1^{\circ}\text{C}$. However, the gain in temperature monitor calibration convenience seems worth the sacrifice of accuracy.

The test set-up for calibrating the temperature monitors is shown in Figures 5.12 and 5.13. The L & N 8687 is a Leeds and Northrup Volt Potentiometer, catalog number 8687, used to measure the thermocouple voltage. The thermocouples are chromel-alumel thermocouples. The EDC VS-111N is an Electronic Development Corporation Precision DC Voltage Standard, Model VS-111N, used to measure the two temperature output voltages. The temperature chamber is a Tenney SST. The ice water was approximately half water, half ice near thermal equilibrium. The thermistors-thermocouple assembly helps insure that all three devices experience the same temperature.

The calibration procedure was as follows. The photometer was turned on and allowed to warm up. With the thermistors-thermocouple assembly in the ice water (both thermocouples in the ice water) the L & N 8687 read 0.020 mV . Since this voltage should ideally read zero, the 0.020 mV will be used as a correction voltage: it will be subtracted from following L & N 8687 readings.

With the thermistors-thermocouple assembly in the temperature chamber, the chamber thermostat is adjusted until the voltage reading on the L & N 8687 indicates a desired temperature, plus the 0.020 mV correction voltage, as shown in a calibration table for chromel-alumel thermocouples

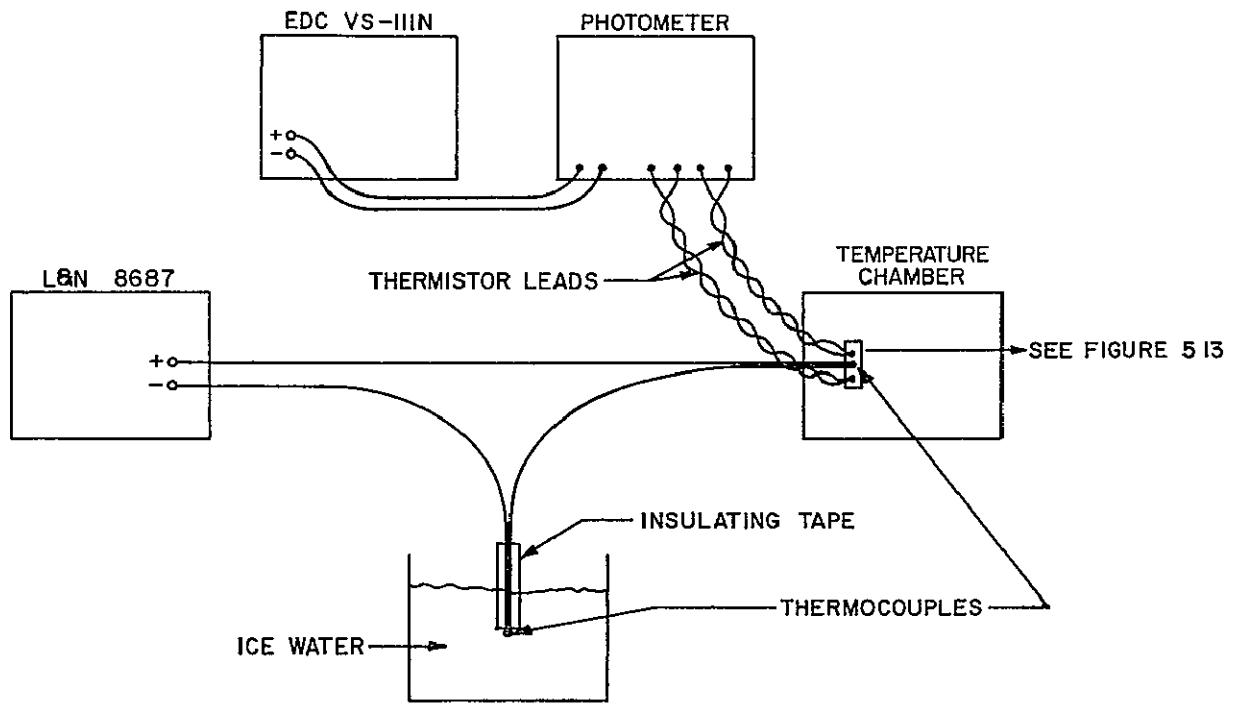


Figure 5.12 Test set-up for calibrating the temperature monitors.

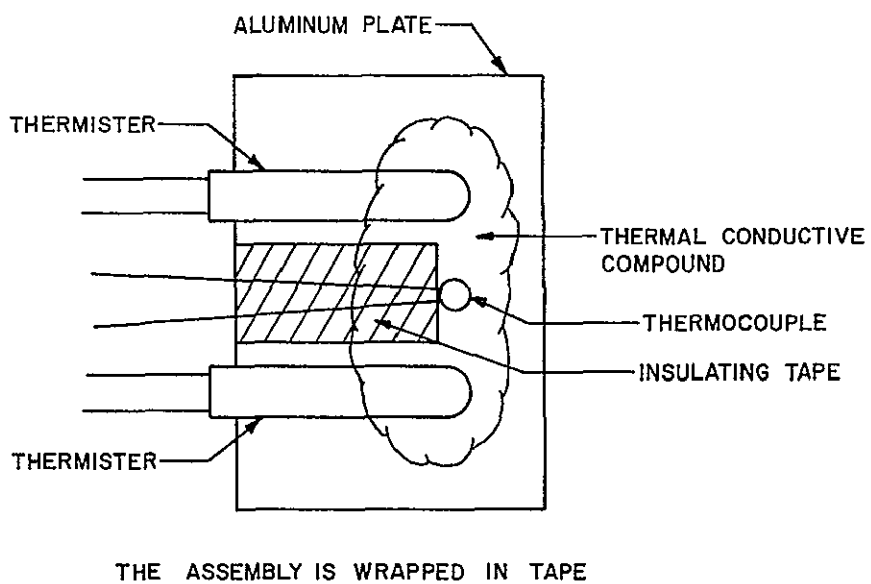


Figure 5.13 Thermistors-thermocouple assembly for calibrating the temperature monitors.

[Weast, 1971]. Then the two photometer temperature output voltages are measured with the EDC VS-111N and recorded. The above is then repeated for as many different temperatures as desired. The calibration chart of Table 5.5 results. Calibration curves are shown in Figures 5.14 and 5.15.

5.5 Other Circuits

5.5.1 *Low-voltage regulators.* Included here are the low voltage regulators not already shown in either the pulse preamplifier schematic or the pulse processor schematic. These regulators are mounted on the frame of the instrument, and include the +28 V to -23 V converter, the +15 V and -15 V regulators used by the pulse processor and temperature monitor circuits, the +5 V regulator used by the pulse processor, and a power resistor connected in series with the -10 V input of the pulse preamplifier. The circuit schematic diagram is shown in Figure 5.16.

The total dc input current from the 28 V supply, for the entire instrument, is 425 mA. The output current from the +28 V to -23 V converter is 130 mA.

5.5.2 *System check.* The system check circuit consists of a resistor in series with an LED, as shown in Figure 5.17. The LED is mounted in the optical assembly as shown in Figure 4.12, whereas the resistor is mounted on the frame of the instrument. The system check is enabled by applying +28 V to the system check signal terminal thereby turning the LED on. If the system check signal terminal is either connected to common or left open the system check LED will be off. When the system check LED is on, and no radiation is coming through the optical filter (such as when the lens cap is on) the instrument count rate should be approximately 105×10^3 counts per second. See Figure 5.18 for oscilloscope traces of the staircase output of the pulse processor when the system check LED

Table 5.5
 Calibration Chart for Temperature Monitor Circuits
 (serial number 1 unit)

<u>measured thermocouple voltage, mV</u>	<u>corrected thermocouple voltage, mV</u>	<u>temperature in °C</u>	<u>filter temperature voltage, V</u>	<u>frame temperature voltage, V</u>
0.020	0.000	0	0.030	0.017
0.220	0.200	5	0.067	0.033
0.420	0.400	10	0.144	0.091
0.620	0.600	15	0.265	0.204
0.820	0.800	20	0.425	0.353
1.020	1.000	25	0.645	0.554
1.220	1.200	30	0.874	0.784
1.420	1.400	35	1.174	1.084
1.630	1.610	40	1.572	1.443
1.830	1.810	45	2.016	1.873
2.040	2.020	50	2.586	2.404
2.250	2.230	55	3.262	3.029
2.450	2.430	60	4.051	3.747
2.660	2.640	65	5.045	4.672
2.870	2.850	70	6.235	5.778

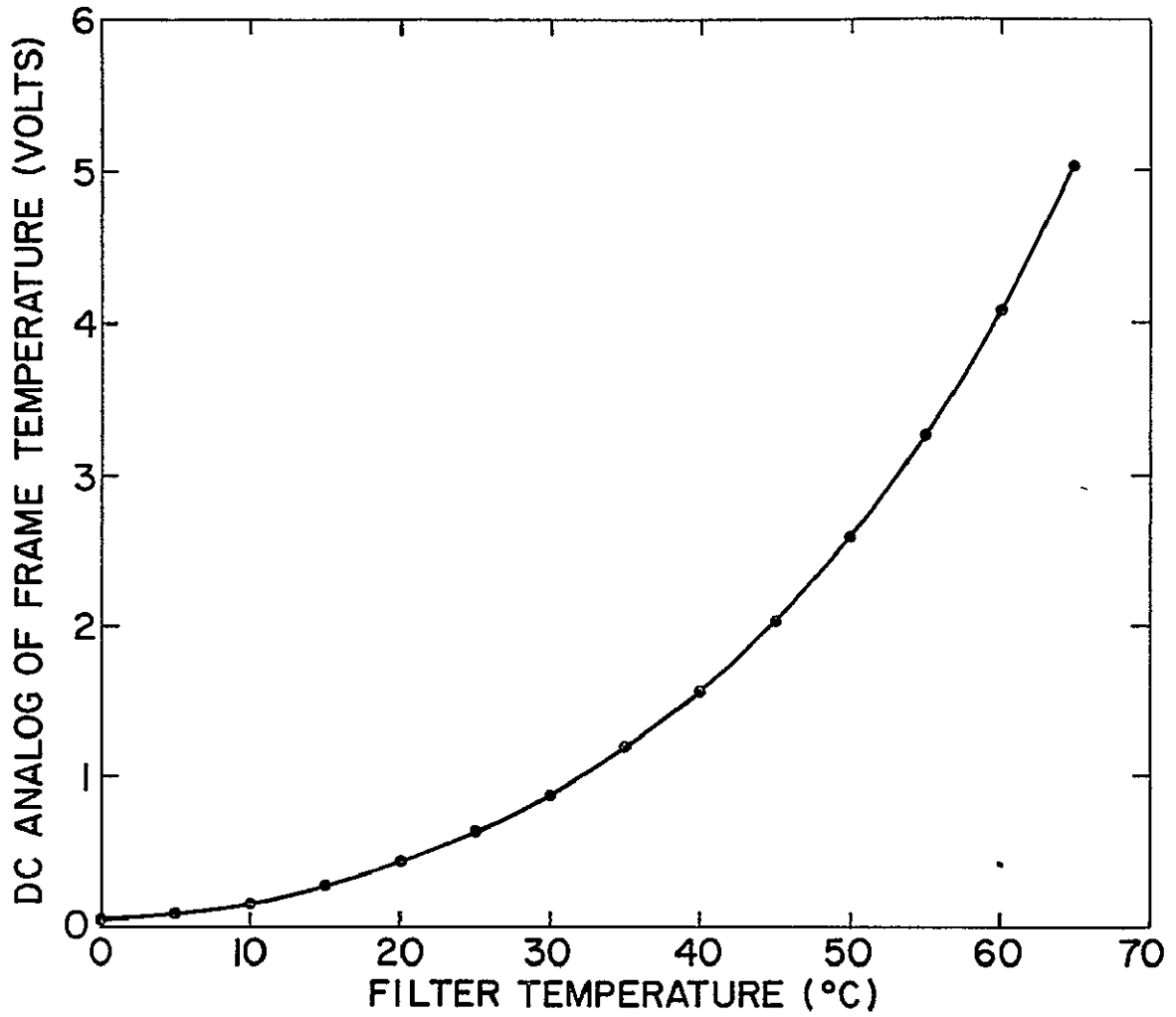


Figure 5.14 Calibration curve for filter temperature monitor (serial number 1 unit).

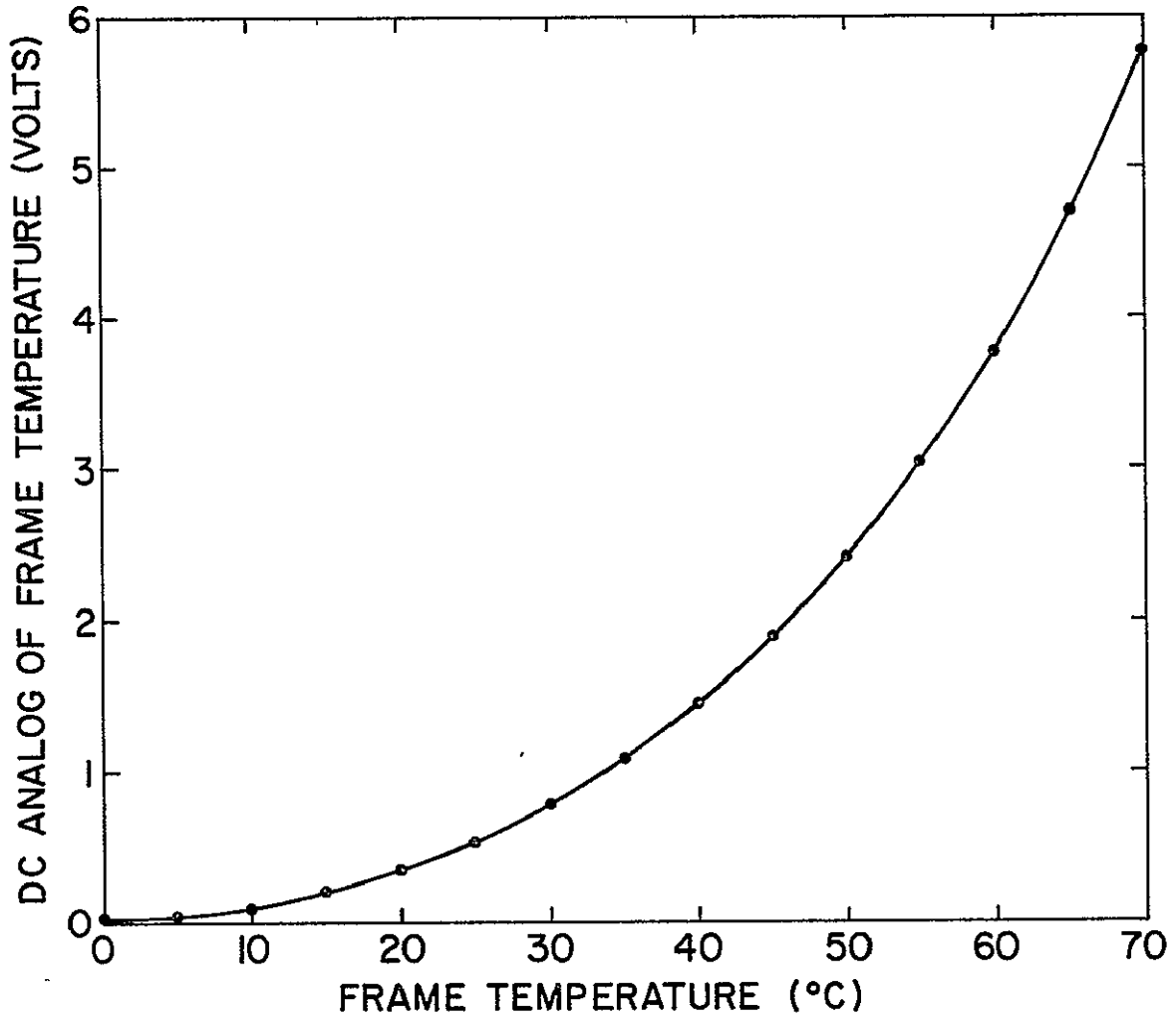


Figure 5.15 Calibration curve for frame temperature monitor (serial number 1 unit).

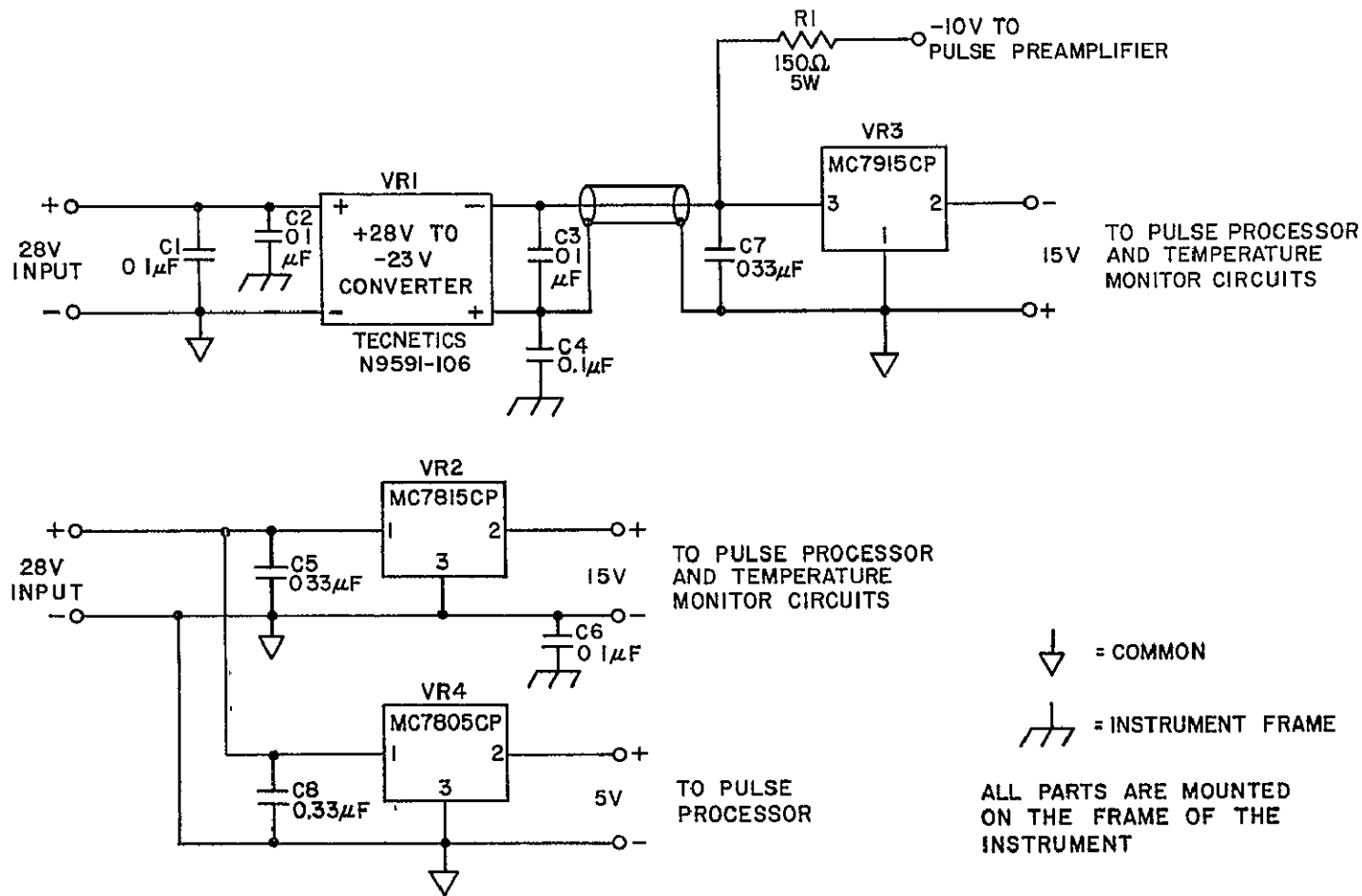


Figure 5.16 Low-voltage regulators schematic diagram.

ORIGINAL PAGE IS
OF POOR QUALITY

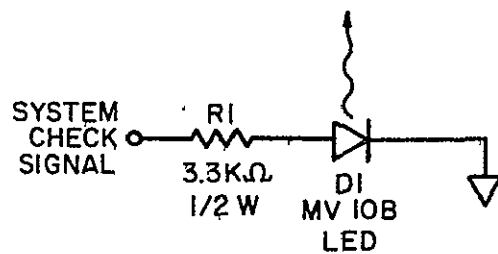


Figure 5.17 System-check schematic diagram.

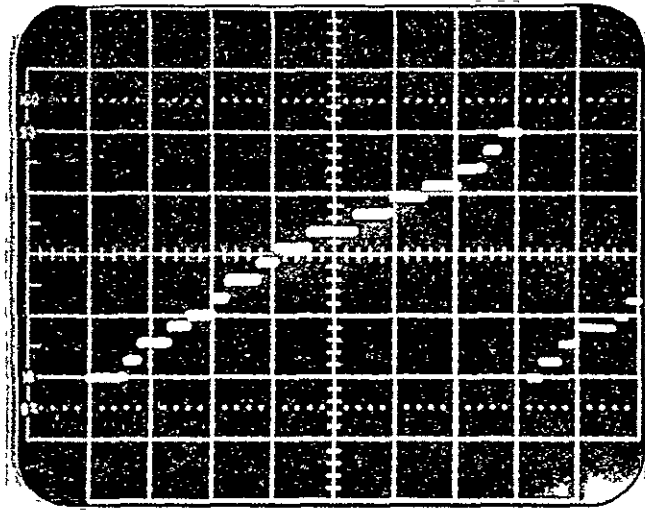
is on; the frequency divider stage in the pulse processor is set at divide-by-eight. Part a of Figure 5.18 shows a single trace as displayed on a storage oscilloscope; note how the trace illustrates that the count-rate is random. Part b of Figure 5.18 shows multiple traces of the staircase output as displayed on a conventional oscilloscope; the blurring results because many traces occur during the time that the shutter of the camera is open and the waveform is random.

5.5.3 *Instrument interconnections.* Instrument interconnections are shown in Figure 5.19. Note that the pulse output of the pulse processor is not available at the instrument connector. Because the pulse output has very fast rise-times and fall-times and is of short time duration, and because of the output impedance characteristics of the 54121, the pulse output is not compatible with long lengths of wire or cable. To obtain output #3 of the instrument (the pulse output) it is necessary to connect a 10:1 oscilloscope probe directly to T7 on the pulse processor board; the other end of the oscilloscope probe may then be connected to an oscilloscope or frequency counter.

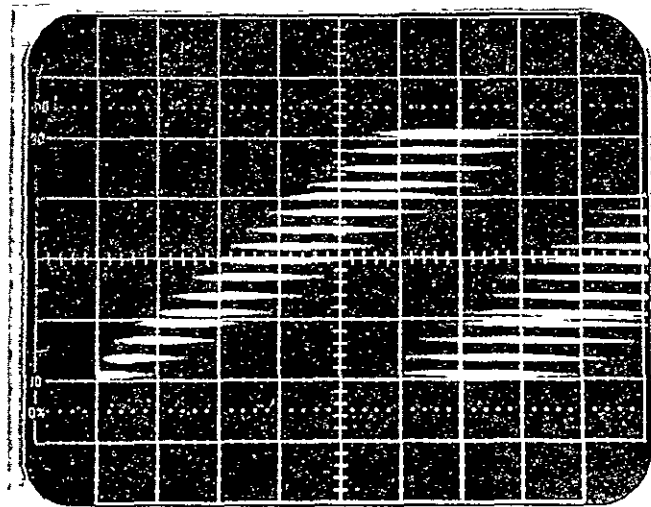
5.6 *Adjustments*

5.6.1 *Negative converter.* The output voltage of VR1 in Figure 5.16 is adjustable. It should be set for -23.0 V.

5.6.2 *High-voltage adjust.* The output voltage of the high voltage power supply in Figure 5.1 is a function of the value of R1. R1 should be selected to give a value of high voltage that will give the channel multiplier a gain of 10^6 . The value of this high voltage varies from channel multiplier to channel multiplier and the data sheets for the specific channel multiplier in use need to be consulted to find the correct high voltage value.



(a)



(b)

Figure 5.18 System-check staircase waveforms: (a) single trace, 1 V/cm, 0.2 ms/cm; (b) multiple traces, 1 V/cm; 0.2 ms/cm.

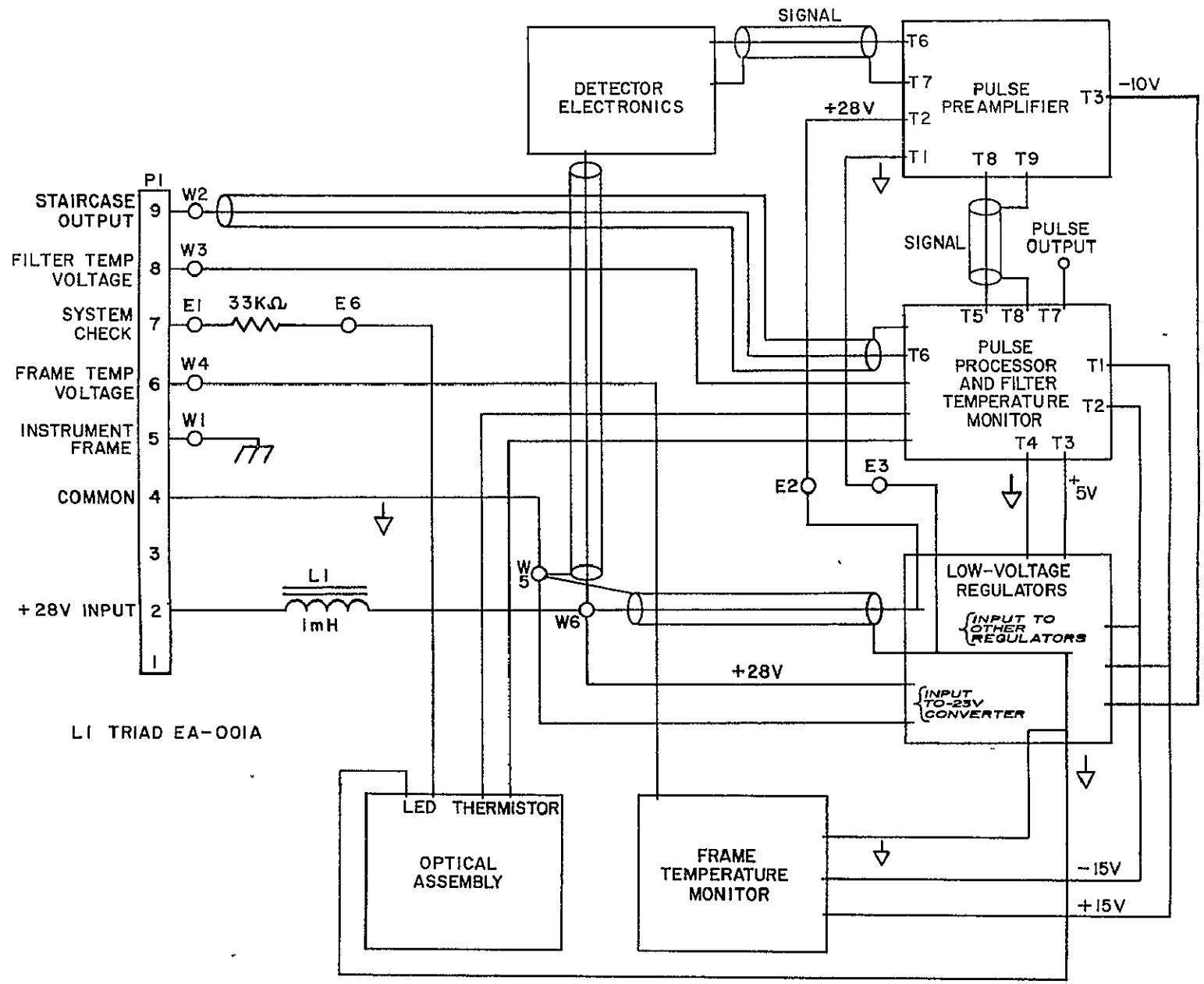


Figure 5.19 Instrument interconnections.

5.6.3 *Pulse preamplifier threshold adjust.* The set-up for making the threshold adjustment is illustrated in Figure 5.20. The alligator clip leads on the end of the 50 Ω cable that connects to the pulse preamplifier should be short. The hot lead should be connected to the preamp input post or to the other end of the input cable - connect the ground lead nearby. No wires need to be unsoldered.

The pulse generator should be set up as follows: negative output pulse, 500 mV peak as measured on an oscilloscope; minimum pulse width, minimum rise time, minimum fall time (not necessarily the minimum setting of the controls, see scope trace); repetition rate, coarse - .3M, vernier - center.

Connect an oscilloscope, through a 10:1 scope probe, to the staircase output of the pulse processor board.

Make the threshold adjustment as follows:

- 1) set the Kay attenuator to 40 dB
- 2) turn the threshold-adjust potentiometer, R13 in Figure 5.4, CCW until the staircase display on the oscilloscope breaks up and becomes erratic.
- 3) turn the threshold-adjust potentiometer slowly CW until the staircase display locks in and becomes stable. It is important that the input cable and the scope probe be physically isolated from each other or feedback may occur.
- 4) test: it should now be possible to increase the attenuation of the Kay attenuator to 50 to 52 dB and still have a stable staircase output.

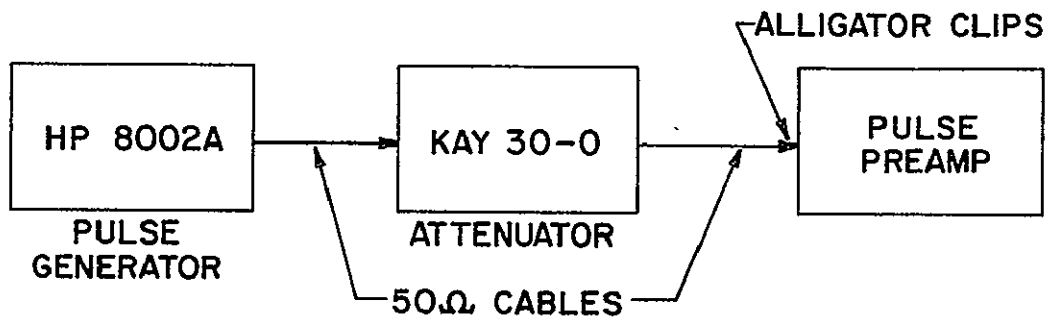


Figure 5.20 Pulse preamplifier threshold adjustment set-up.

6. ANALYSIS OF INSTRUMENT SENSITIVITY

The purpose of this chapter is to present the theoretical factors that must be taken into consideration when interpreting the output of the photometer, and calculations that predict the theoretical output of the photometer for a given layer radiation.

6.1 *Introduction*

Some of the theoretical factors that must be taken into consideration when interpreting the output of the photometer were presented in Chapter 2. These are: ionization sources other than energetic electrons, vibrational and rotational temperatures of the emitting N_2^+ (including the variation with height), and extraterrestrial light and unwanted airglows within the pass band of the optical filter. These factors were discussed in Chapter 2 and it was concluded that, at least at Wallops Island under disturbed geomagnetic conditions, it is probable that other ionization sources and other sources of light may be ignored. It is possible that, even under quiet geomagnetic conditions, photometric measurements of radiation at 391.4 nm will give a measure of energetic electron flux; whether this conclusion can be made awaits the results of experiments, and correlation analysis of the data with that received from other independent measurements of energetic electron flux.

Atmospheric absorption and scattering has not previously been discussed. Atmosphere between the layer and the photometer can absorb part of the emission, thereby decreasing the photometer incident radiation. In the rocket-borne instrumentation system the payload doors will be ejected at 40 km; less than 1% of the earth's atmosphere remains above 40 km, and atmospheric absorption should be negligible at 391.4 nm. In a ground-based instrumentation system atmospheric absorption may be

significant, and will need to be considered when interpreting the output of the photometer. The effects of absorption and scattering can be theoretically analyzed but physical measurements can supply the desired data. During the initial rocket flight a ground-based measurement will be simultaneously conducted, and by comparing the output of the ground-based photometer with that of the rocket-borne instrument prior to its entering the layer, a measure of atmospheric absorption and scattering at 391.4 nm will be obtained.

Another theoretical factor that has not yet been considered in this report is the detailed relationship between 391.4 nm radiation intensity and energetic electron flux. This is a rather difficult relationship to determine with a high degree of accuracy, and will not be considered here. The problem has been addressed for auroras, for example by *Rees* [1963], and much that has been done there should be applicable at mid-latitudes.

The theoretical factors that will be discussed in the remainder of this chapter include the dependence of the radiation incident on the photometer upon the layer height, the dependence of the incident radiation upon the look-angle with respect to zenith, and the dependence of the channel multiplier input upon the optical filter temperature. All of these factors will then be taken into consideration, as well as some others, and the theoretical output of the photometer will be calculated for a given layer radiation.

6.2 *Incident Radiation Independent of Layer Height*

In the following calculations we will assume that the layer may be accurately represented by a plane at altitude h above the point of observation and normal to the look-angle of the instrument as illustrated in Figure 6.1.

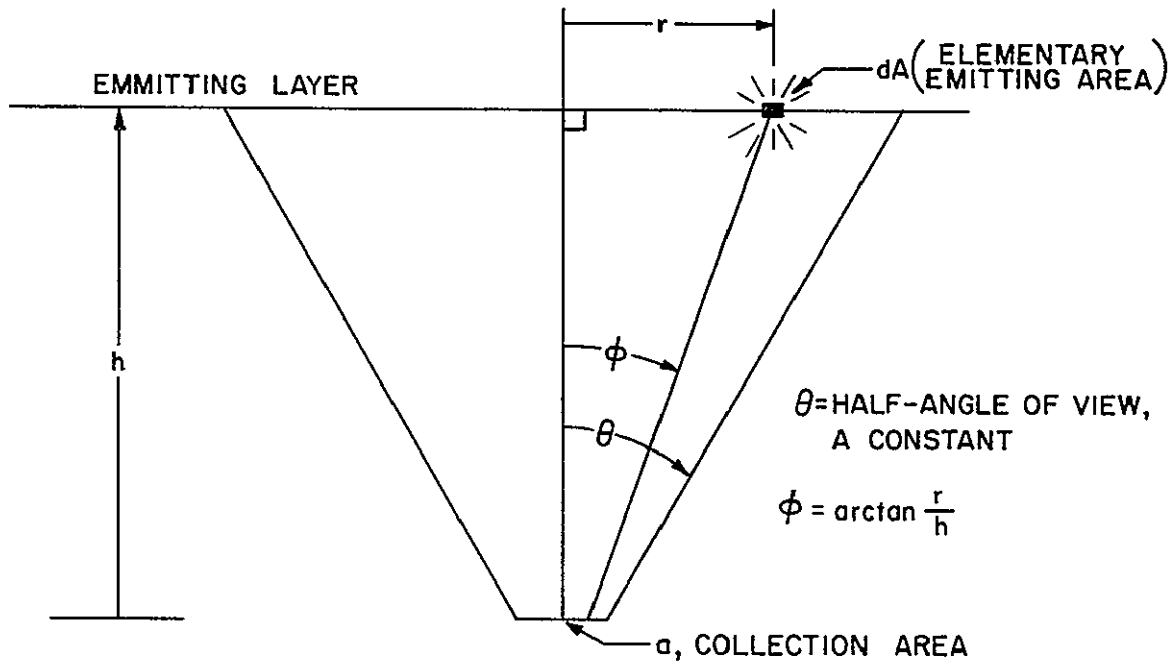


Figure 6.1 Geometry of the photometer directed normal to the emitting layer.

The actual emission comes from a layer, not a plane, but calculations are simplified if the layer is considered to be infinitely thin. In the following calculations, which represents the layer as a plane, it is found that the incident radiation is independent of layer height. This suggests that if there were two or more emitting planes parallel to one another, the incident radiation could be found by superposition but the individual layer heights would be irrelevant. So, the actual layer may be represented as made up of an infinite set of parallel planes running from height h_1 to height h_2 . Since the individual heights are irrelevant to the incident radiation (at least prior to the rocket-borne instrument entering the layer), all of the planes may be represented at one height h . We will also assume that the emission rate is the same for all elementary volumes of the plane (the emitting plane is uniform) and each elementary volume emits isotropically.

The total spherical surface area at a distance of $h \sec \phi$ from the isotropically emitting element of volume is (Figure 6.1)

$$4\pi h^2 \sec^2 \phi$$

The effective collection area of the vertically pointing photometer is

$$a \cos \phi$$

where a is the collection area of the photometer.

The emission rate in units of 10^6 photons s^{-1} of the element of area dA is

$$RdA$$

where R is the emission rate of the emitting layer in rayleighs. One rayleigh is an apparent column emission rate of 10^6 photons $cm^{-2} s^{-1}$.

The signal at the collection area due to the emission from dA is

$$\frac{RdA \alpha \cos \phi}{4\pi h^2 \sec^2 \phi}$$

To obtain the total incident radiation rate on the photometer collection area when the entire emitting plane is considered, it is necessary to integrate over the circular area determined by the intersection of the angle of view of the photometer and the emitting plane, as shown in Figure 6.2.

The range of r is from zero to $h \tan \theta$ where θ is the half-angle of view of the photometer. The range of α is from zero to 2π . Therefore the total incident radiation rate of the photometer, P , (in units of 10^6 photons s^{-1}) is given by the following expression:

$$P = \int_0^{2\pi} \int_0^{h \tan \theta} \frac{R\alpha \cos \phi}{4\pi h^2 \sec^2 \phi} r dr d\alpha = \frac{R\alpha}{4\pi h^2} \int_0^{2\pi} \int_0^{h \tan \theta} \cos^3 \phi r dr d\alpha$$

But $r = h \tan \phi$ and $dr = h \sec^2 \phi d\phi$. And when $r = h \tan \theta$, $\phi = \theta$.

Therefore,

$$P = \frac{R\alpha}{4\pi} \int_0^{2\pi} \int_0^{\theta} \sin \phi d\phi d\alpha = \frac{R\alpha}{4\pi} \int_0^{2\pi} (1 - \cos \theta) d\alpha = \frac{R\alpha}{2} (1 - \cos \theta)$$

But $1 - \cos \theta = 2 \sin^2 \frac{\theta}{2}$

Therefore,

$$P = R\alpha \sin^2 \frac{\theta}{2} \tag{6.1}$$

Note that equation (6.1) is independent of the height, h . This says that, neglecting atmospheric losses between the emitting layer and the photometer, the incident radiation is independent of the distance between

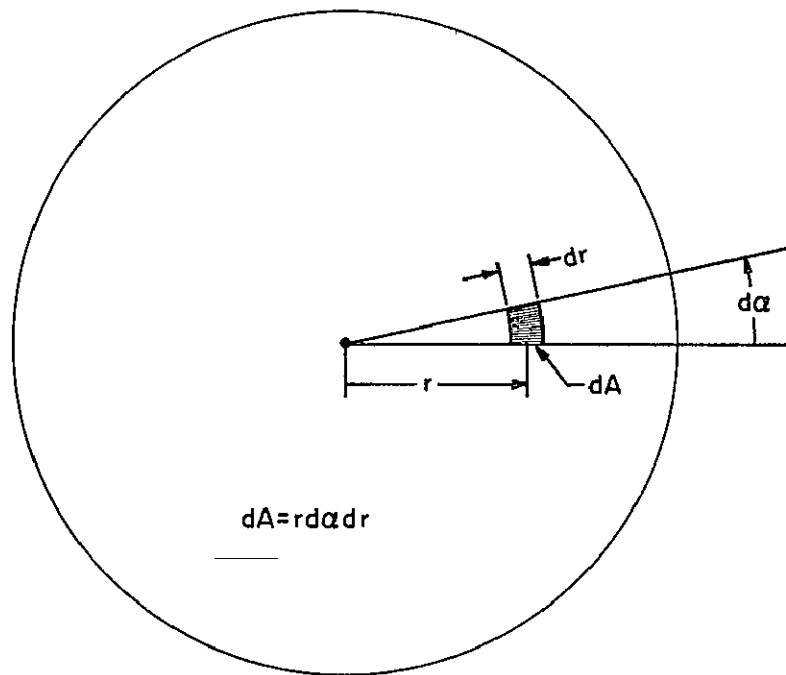


Figure 6.2 The intersection of the angle-of-view cone and the emitting layer.

the layer and the instrument.

Suppose R is 1 rayleigh, θ is 5° , and the diameter of the lens (the collector) is 2.54 cm. The area of the lens is 5.07 cm^2 . The incident radiation rate is then found using equation (6.1):

$$P = 10^6 \left(\frac{\text{photons}}{\text{cm}^2 \text{ sec}} \right) \times 5.07 \text{ (cm}^2) \times 0.0019 = 9646 \text{ photons/sec}$$

It is common to express equation (6.1) in terms of steradians. One steradian is the solid angle which forms a cone such that the enclosed surface, on a sphere, is equal to the square of the radius of the sphere. There are 4π steradians in a sphere. It is easily shown that, for a conical field of view having a half-angle θ , the solid angle Ω is $4\pi \sin^2 \frac{\theta}{2}$ steradians. Thus equation (6.1) may also be written

$$P = \frac{Ra\Omega}{4\pi} \tag{6.2}$$

6.3 *Incident Radiation Dependent Upon Angle with Respect to Zenith*

We will make the same assumptions here that we did in Section 6.2: that the emitting layer may be represented by a plane, and that the emission rate is the same for all differential volumes of the plane. In the following calculations we shall make use of Figures 6.3 and 6.4. Figure 6.3 illustrates the geometry in two dimensions. Figure 6.4 illustrates the geometry in three dimensions; to simplify the figure, an actual sketch of the cone and the resultant ellipse at the intersection with the plane is not shown. Some dimensions have been exaggerated to allow more room for labeling. A clear picture results if Figures 6.3 and

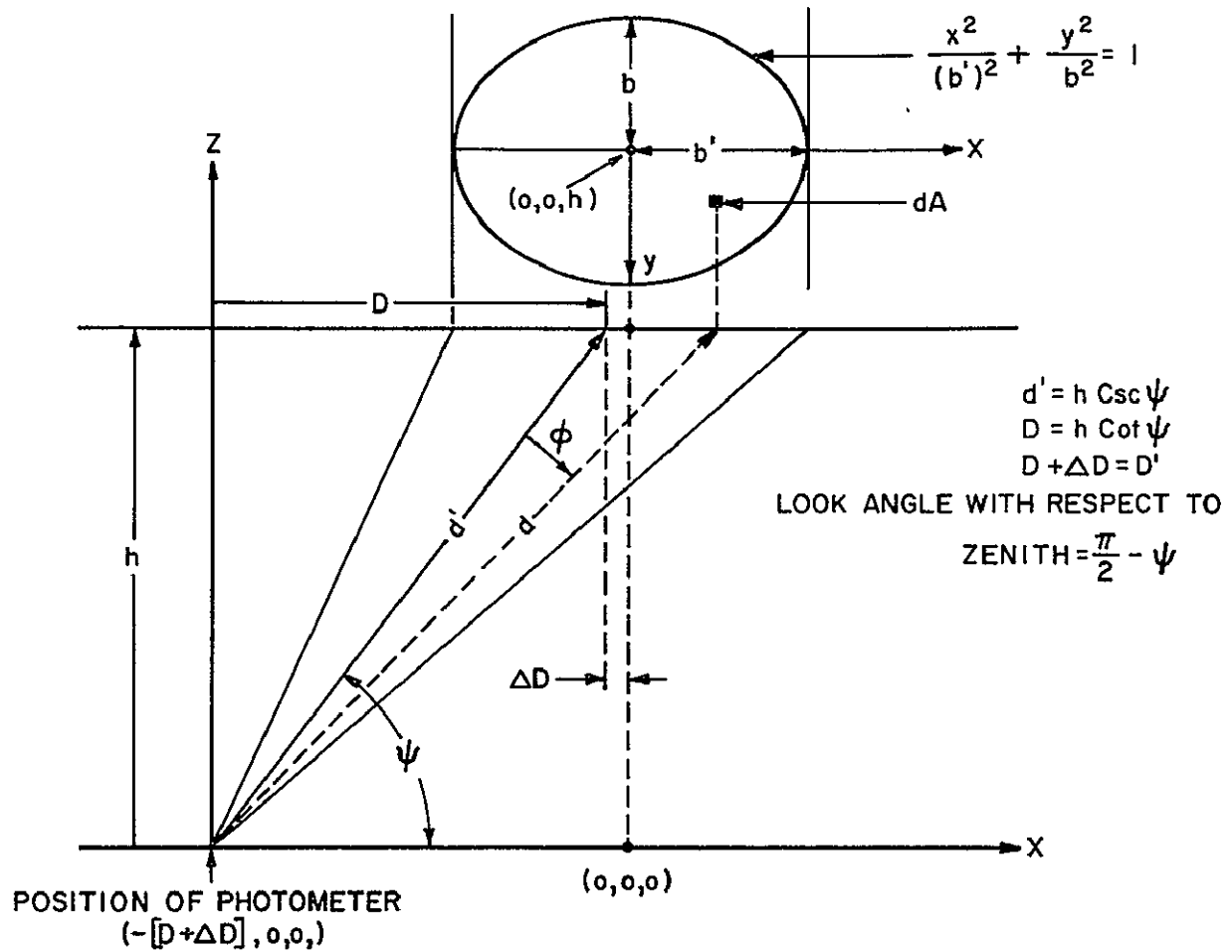


Figure 6.3 Look-angle of the photometer oblique to the emitting layer. two-dimensional geometry.

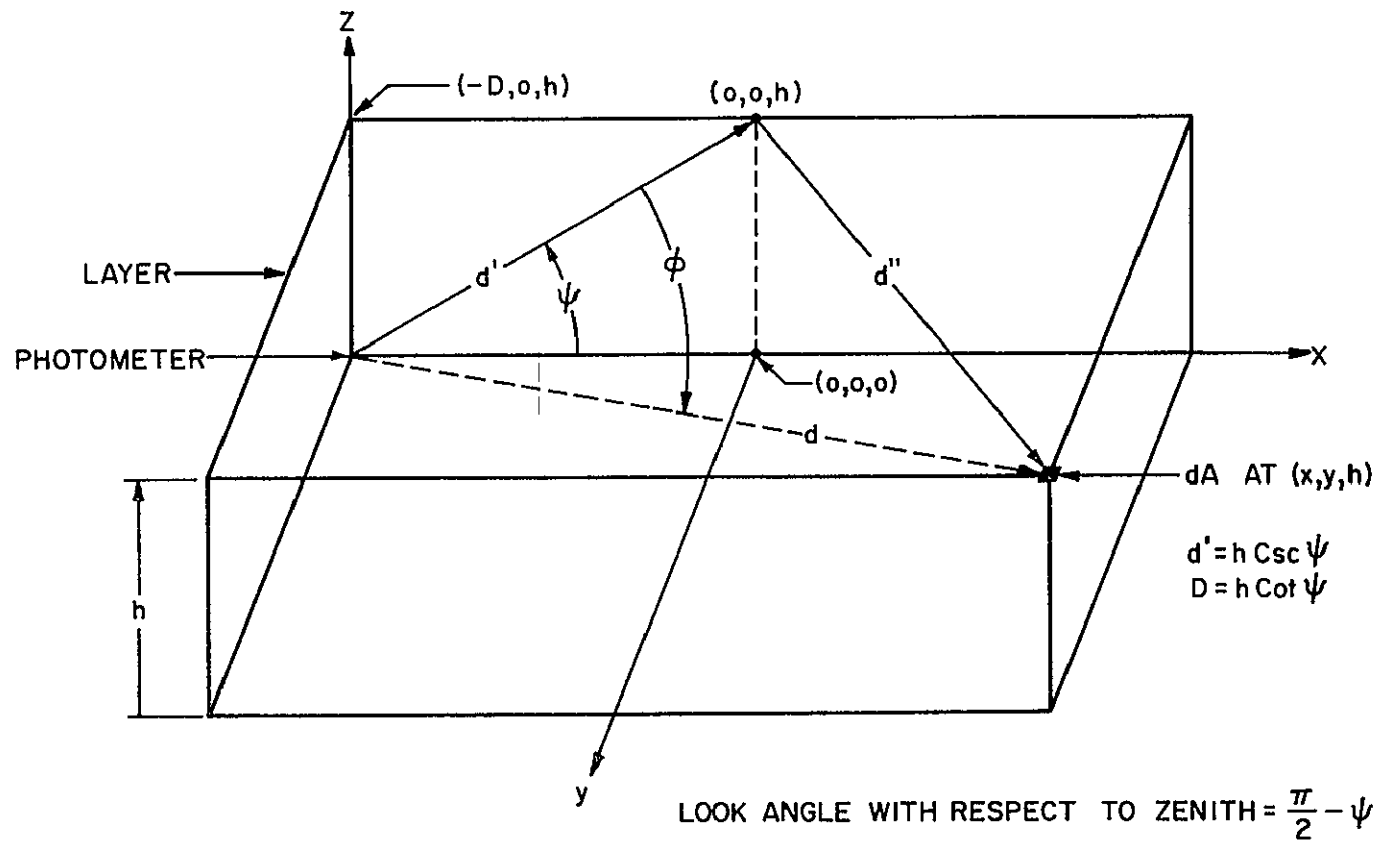


Figure 6.4 Look-angle of the photometer oblique to the emitting layer: three-dimensional geometry.

6.4 are carefully compared. One difference may be noted between the two figures: in Figure 6.4 the assumption has been made that

$$D' = D + \Delta D \cong D$$

An expression for D' may be derived with the aid of Figure 6.5. This effort will also yield an expression for b' of Figure 6.3.

All three angles in the triangle formed by the sides j , f , e in Figure 6.5 are known, as are the angles in the triangle formed by the sides e , g , f . One side of each triangle is also known:

$$f = d' \tan \theta$$

After some trigonometric manipulation, the following expressions are obtained from Figure 6.5:

$$e = d' \tan \theta \sin \psi \left[1 + \frac{\cot \psi}{\tan(\psi - \theta)} \right] \quad (6.3)$$

and

$$c = d' \frac{\sin \theta}{\sin(\psi + \theta)} \quad (6.4)$$

An expression for the center of the ellipse is as follows:

$$D' = D + \frac{e-c}{2} \quad (6.5)$$

And an expression for b' is as follows:

$$b' = \frac{e+c}{2} \quad (6.6)$$

The following approximation will be made:

$$b = d' \tan \theta \quad (6.7)$$

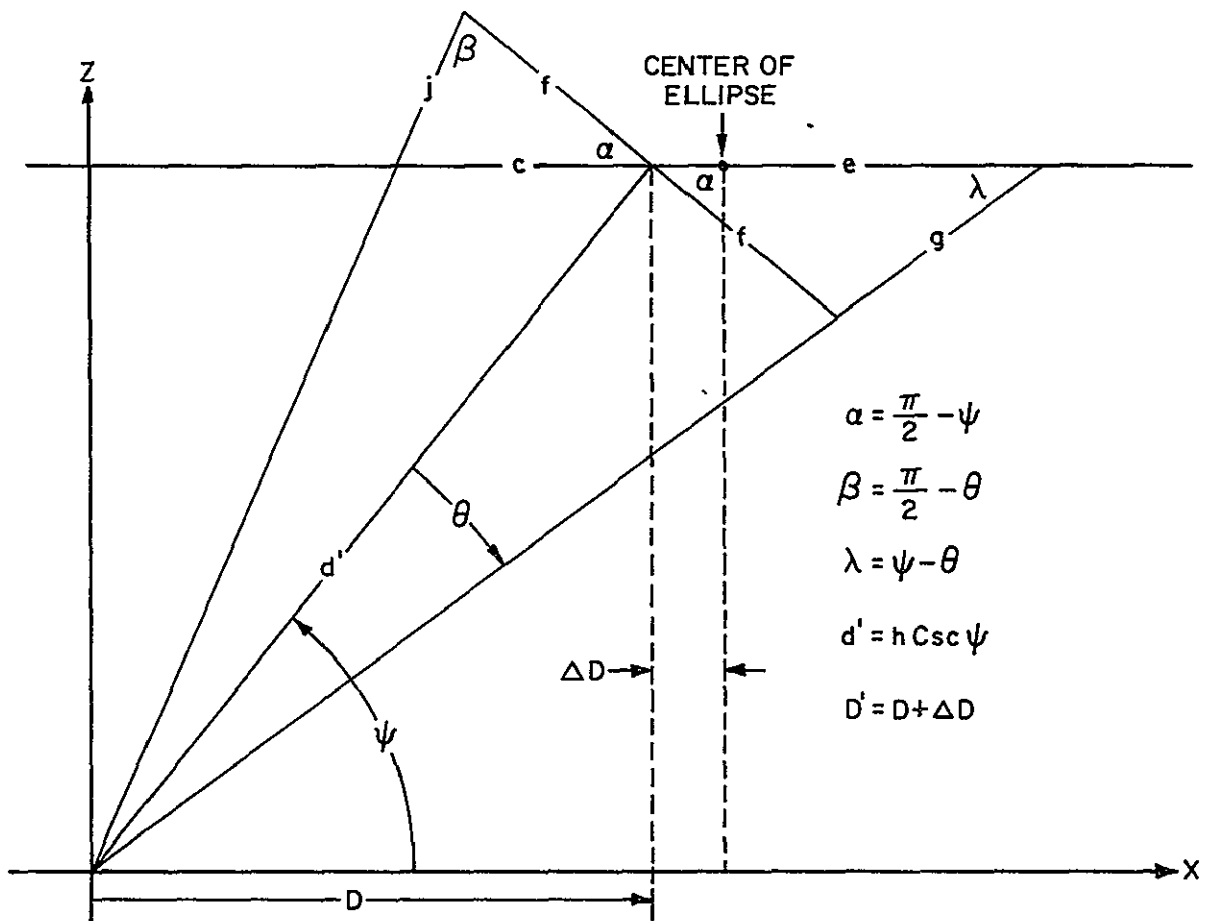


Figure 6.5 Illustration aiding the development of an expression for the center of the ellipse.

which is strictly the distance from the major axis to the outside edge of the ellipse in Figure 6.3 at values of $x = \pm \Delta D$.

In this particular photometer, the value of θ is 5° as specified in Chapter 4. The look-angle of the instrument with respect to the axis of the rocket (in the rocket-borne instrumentation system) is 45° . The maximum angle between zenith and the axis of the rocket is 15° , therefore the maximum angle between zenith and the look-angle of the photometer will be 60° . Therefore, the minimum value of ψ , which will maximize the value of ΔD , is 30° . Using $\theta = 5^\circ$, $\psi = 30^\circ$, equations (6.3), (6.4), (6.5) and the following equation

$$d' = D \sec \psi$$

The following expression for D' can be obtained:

$$D' = 1.03 D$$

Since the above expression is the maximum value of D' , the approximation that $D' = D$ seems a valid one to make.

By referring to Figure 6.4 the following relationships are noted:

$$d = [(D+x)^2 + y^2 + h^2]^{\frac{1}{2}}$$

$$d'' = [x^2 + y^2]^{\frac{1}{2}}$$

By the law of cosines:

$$\begin{aligned} \cos \phi &= \frac{(d')^2 + d^2 - (d'')^2}{2d'd} \\ &= \frac{(d')^2 + (D+x)^2 + h^2 - x^2}{2d'd} \end{aligned}$$

The total spherical surface area at a distance of d from the isotropically emitting elementary volume is

$$4\pi d^2$$

The effective collection area is $\alpha \cos \phi$ where α , as in Figure 6.1, is the collection area of the photometer determined by the size of the lens.

The emission rate collected by the photometer due to the emission from dA is

$$\begin{aligned} \frac{RdA \alpha \cos \phi}{4\pi d^2} &= \frac{Ra}{4\pi d^2} \frac{(d')^2 + (D+x)^2 + h^2 - x^2}{2d'd} dx dy \\ &= \frac{Ra}{8\pi d'} \frac{(d')^2 + D^2 + 2Dx + h^2}{(D^2 + 2Dx + x^2 + y^2 + h^2)^{3/2}} dx dy \end{aligned}$$

To obtain the total incident radiation rate of the photometer collection area when the entire emitting plane is considered, it is necessary to integrate over the elliptical area determined by the intersection of the cone of view and the emitting plane.

The range of x is from $-\frac{b'}{b} \sqrt{b^2 - y^2}$ to $+\frac{b'}{b} \sqrt{b^2 - y^2}$. The range of y is from $-b$ to $+b$. Therefore the total incident radiation rate of the photometer, P , is given by the following expression:

$$P = \frac{Ra}{8\pi d'} \int_{-b}^{b} \int_{-\frac{b'}{b} \sqrt{b^2 - y^2}}^{\frac{b'}{b} \sqrt{b^2 - y^2}} \frac{(d')^2 + D^2 + 2Dx + h^2}{(D^2 + 2Dx + x^2 + y^2 + h^2)^{3/2}} dx dy \quad (6.8)$$

where

P = incident radiation rate of the photometer in photons
per second

R = emission rate of the emitting layer in photons cm^{-2}
(column) sec^{-1}

a = collection area of the photometer

$b' = \frac{e+c}{2}$, e and c given by equations (6.3) and (6.4)

$b = d' \tan \theta$, equation (6.7)

$d' = h \csc \psi$

$D = h \cot \psi$

h = height of the layer above the photometer

ψ = look-angle of the photometer with respect to the horizontal

θ = half-angle of view of the photometer

Equation (6.8) has been evaluated numerically by the computer program in Appendix II.3. When the data card enters 0.0872665 for theta and 1.670796 for psi, the program will calculate P for angles of ψ equal to 1.5708, 1.4708, 1.3708, 1.2708, 1.1708, 1.0708, 0.9708, 0.8708, 0.7708, 0.6708, 0.5708, 0.4708, and 0.3708 radians; $\theta = 0.0872665$ radians (5°), $\alpha = 5.07 \text{ cm}^2$, $R = 10^6 \text{ photons cm}^{-2} \text{ sec}^{-1}$, and $h = 50, 75, 100, 125,$ and 150 km . The various values of h were used to verify that the photometer output will be independent of h even when the look-angle with respect to zenith is other than zero: for each value of ψ , the photometer output computed to be independent of h . The results are shown in Table 6.1. Also shown in Table 6.1, for comparison, are computed values of the following expression:

$$P = Ra \sin^2 \frac{\theta}{2} \csc \psi \quad (6.9)$$

The results are also shown in Figure 6.6.

As mentioned earlier, the minimum value of ψ in this particular application will be 30° , or 0.5236 radians. At an angle of 0.5708 radians, the result of equation (6.9) is 3.2% below that of equation (6.8). At an angle of 0.4708 radians, the result of equation (6.9) is

Table 6.1
Incident Radiation as a Function of ψ

ψ in radians	P computed using equation (6.8)	P computed using equation (6.9)
1.5708	9646	9646
1.4708	9696	9694
1.3708	9848	9842
1.2708	10110	10097
1.1708	10498	10473
1.0708	11036	10992
0.9708	11761	11687
0.8708	12732	12612
0.7708	14044	13845
0.6708	15854	15518
0.5708	18451	17853
0.4708	22428	21265
0.3708	29243	26620

ψ is the photometer look-angle with respect to the horizontal

P is the incident radiation rate of the photometer in photons per second

$$R = 10^6 \text{ photons cm}^{-2} \text{ sec}^{-1}, \theta = 5^\circ, a = 5.07 \text{ cm}^2$$

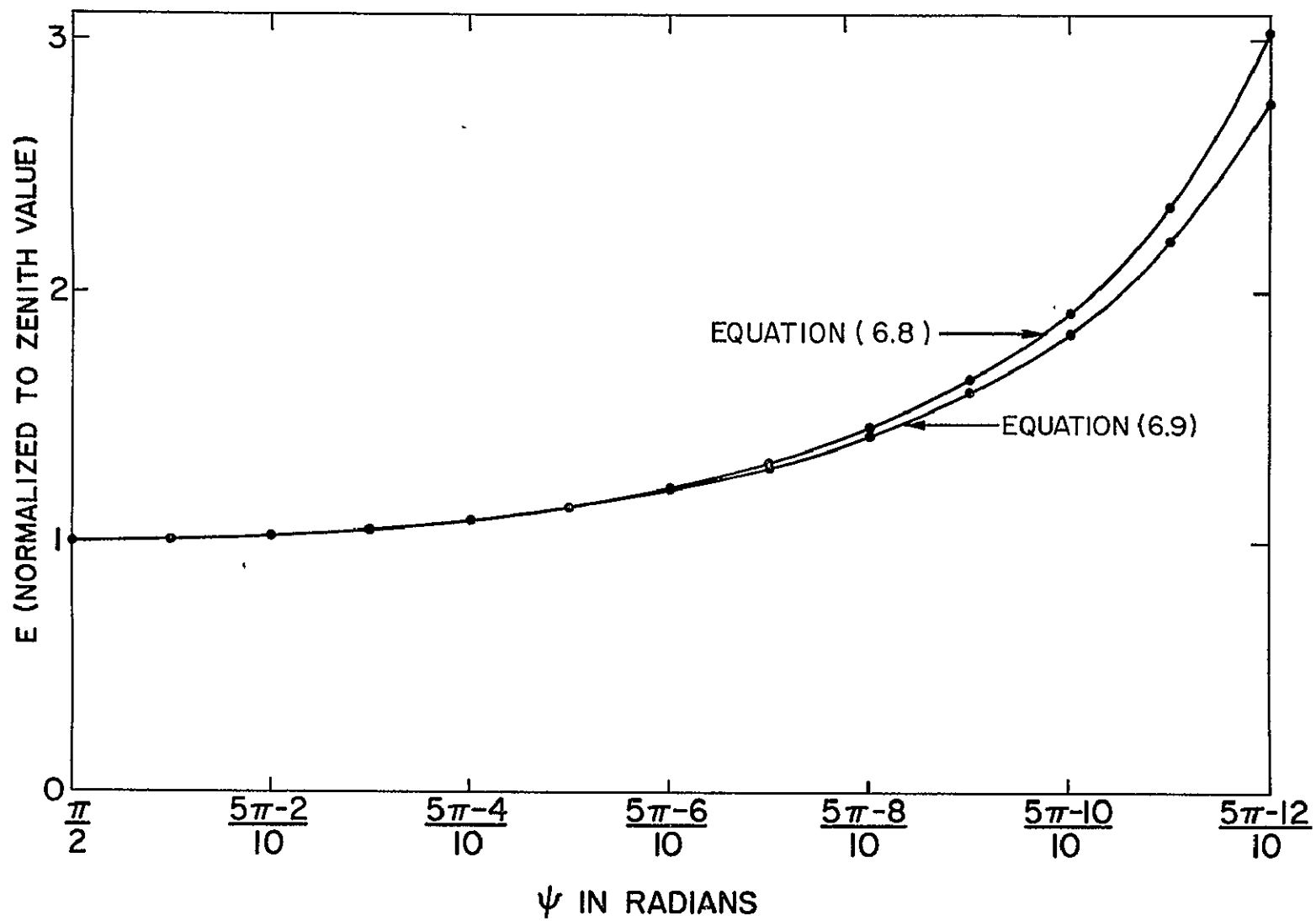


Figure 6.6 Incident radiation as a function of ψ .

5.2% below that of equation (6.8). Because of the simplicity of equation (6.9) compared with equation (6.8), and because of the relatively small error introduced by its use, equation (6.9) will be used as the expression for the incident radiation rate of the photometer.

6.4 Channel Multiplier Input as a Function of Filter Temperature

Equation (6.9) gives the incident radiation rate at the window of the photometer. This equation can be simplified for this particular photometer because $\alpha = 5.07 \text{ cm}^2$ and $\theta = 5^\circ$. Therefore,

$$P = 0.009646 R \csc \psi \quad (6.10)$$

where

P = incident radiation rate of the particular photometer of this report in photons s^{-1}

R = column emission rate of the emitting layer in photons $\text{cm}^{-2} \text{ s}^{-1}$

ψ = look-angle of the photometer with respect to the horizontal

According to the manufacturer, the typical value of transmission of the window at 391.4 nm is 83%. Therefore, the incident radiation rate at the optical filter of the photometer is 83% of equation (6.10), or

$$P' = 0.008006 R \csc \psi \quad (6.11)$$

We are assuming that the above relation is independent of wavelength over the narrow band of wavelengths of interest here. However, the output of the optical filter is highly dependent upon wavelength.

In order to proceed, we must assume that we accurately know the transmission characteristics of the optical filter in a converging, homogeneous beam. Usually, filter characteristics are provided by the manufacturer for collimated light. In a converging beam, the center

wavelength will shift to a shorter value and the bandwidth will become broader. The determining of the transmission characteristics in a converging beam is part of the physical calibration.

Let us assume a mathematical model of the transmission characteristics of an optical filter in a converging beam with a cone half angle of 5° as represented in equation (6.12). This is actually a mathematical model of the transmission characteristics of an optical filter in collimated light, at 25°C .

$$T = 0.191 \exp \left[-\frac{1}{2} \left(\frac{\lambda - 3916.4}{6.65} \right)^2 \right] + 0.02 \exp \left[-\frac{1}{2} \left(\frac{\lambda - 3930.0}{10} \right)^2 \right] \\ + 0.01 \exp \left[-\frac{1}{2} \left(\frac{\lambda - 3897.0}{8} \right)^2 \right] \quad (6.12)$$

A graph of equation (6.12) is shown in Figure 6.7.

At a given wavelength, the output radiation rate of the optical filter is equation (6.11) multiplied by the transmission of the filter at that wavelength. For example, at 391.66 nm, the output radiation rate of the optical filter is $0.001601 R \csc \psi$.

However, the emission that the photometer is to measure is not at one wavelength but includes many wavelengths in a narrow band. In order to compute the filter output radiation rate it is necessary to convolve the filter transmittance function with the emission spectrum.

The computer program in Appendix II.2 folds equation (6.12) with the discrete line spectra. It does it for spectra at the following vibrational and rotational temperatures: 200, 300, 500, 1000, 2000, and 5000 K. Also, since the center wavelength of the filter is temperature

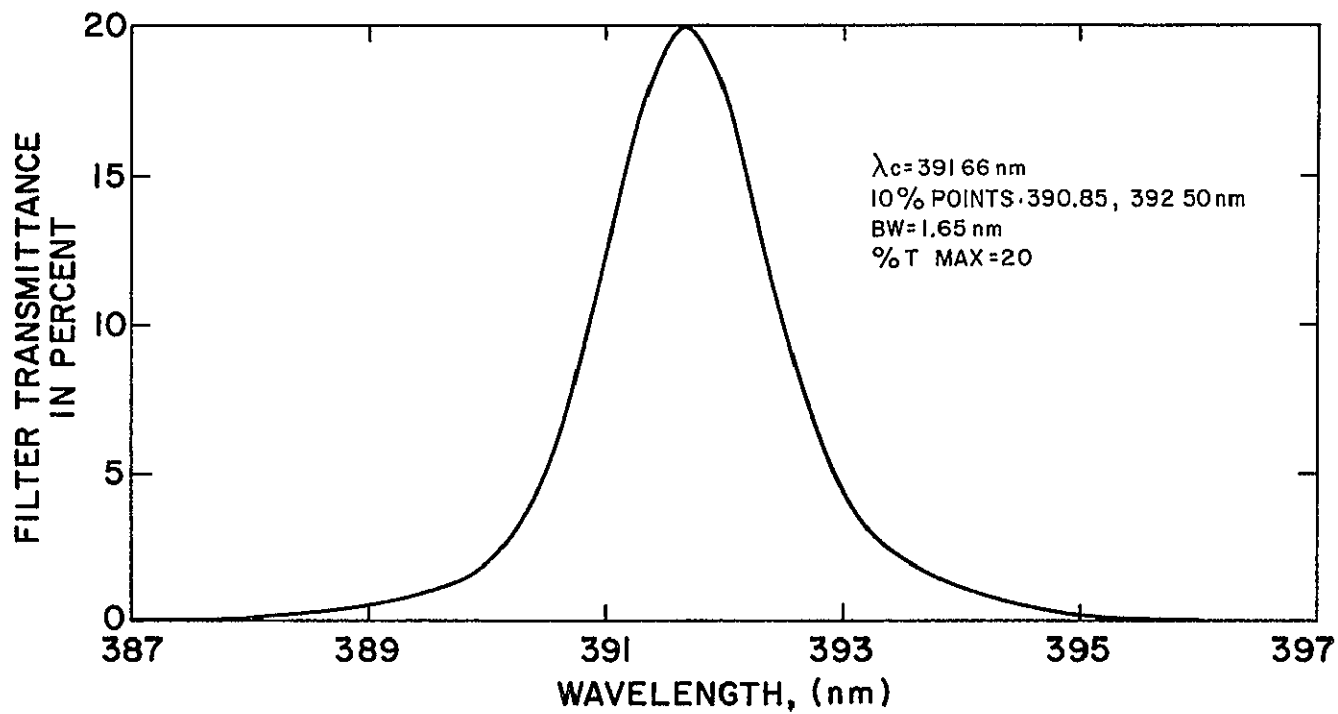


Figure 6.7 An optical filter transmittance versus wavelength curve (graph of equation (6.12)).

sensitive, the program folds the filter transmittance function for center wavelengths ranging from 391 to 392.5 nm in 0.1 nm steps. The results are shown in Figure 6.8.

Suppose that the vibrational and rotational temperatures of the layer are 1000 K, and that the filter center wavelength is 391.4 nm. Then the transmission of the filter (considering all wavelengths in the emission spectrum) would be 10.6%. Multiplying this by equation (6.11) results in an expression for the output of the optical filter: $849 \times 10^{-6} R \text{ csc } \psi$.

According to the manufacturer, the typical value of transmission of the lens at 391.4 nm is 90%. Therefore, the output of the lens (the input to the channel multiplier) is

$$P'' = 764 \times 10^{-6} R \text{ csc } \psi \quad (6.13)$$

The above expression is an example only. A general equation follows:

$$M = P T_W T_F' T_L \quad (6.14)$$

where

M = input radiation rate to the channel multiplier in photons per second

P = incident radiation rate of the photometer in photons per second, given by equation (6.8), (6.9), or (6.10)

T_W = transmission of the optical window at 391.4 nm

T_F' = effective transmission of the optical filter, taking into consideration the converging-beam transmission characteristics of the filter and the emission spectral characteristics

T_L = transmission of the lens at 391.4 nm

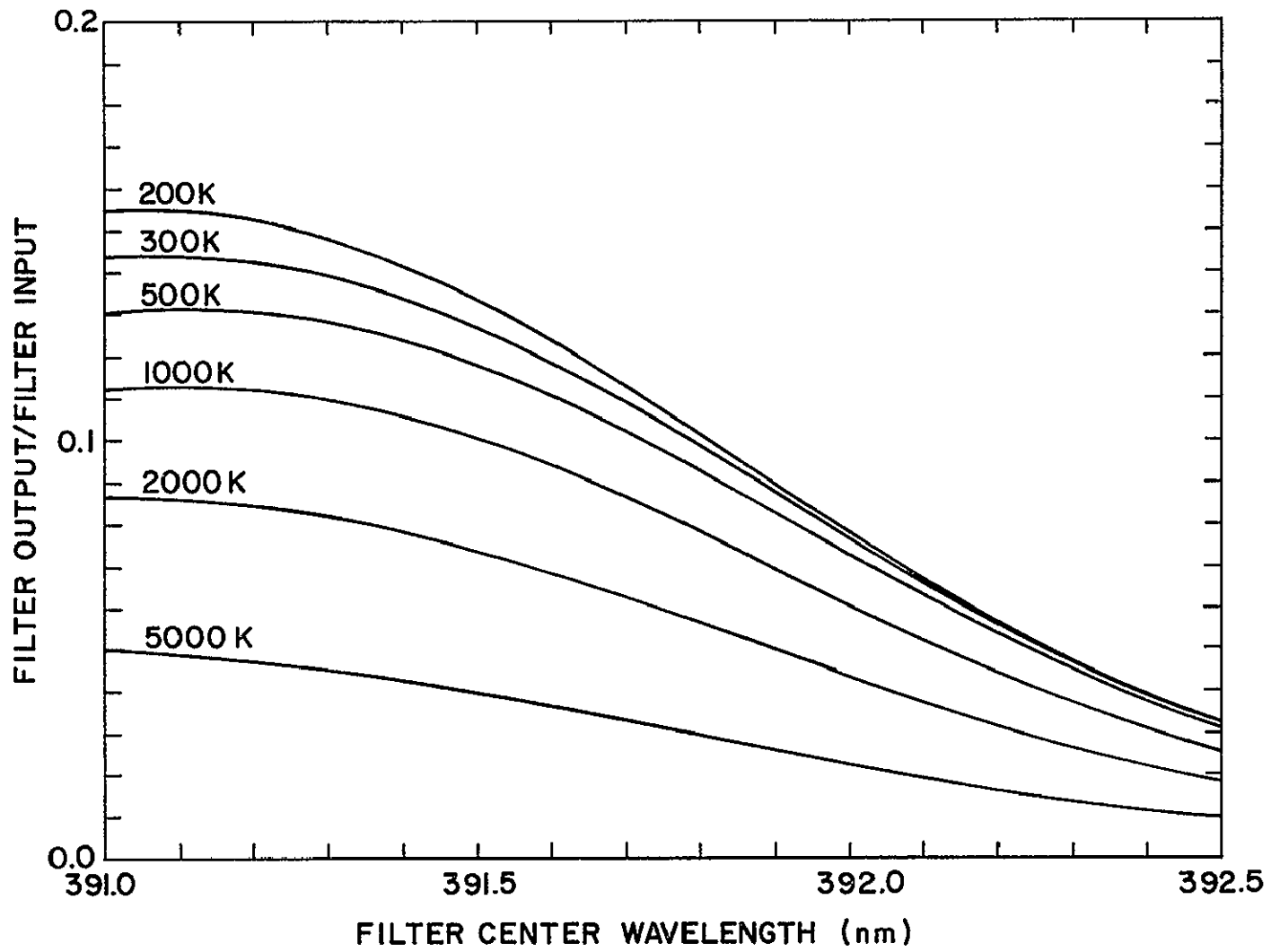


Figure 6.8 Convolution of equation (6.12) with discrete line spectra.

6.5 Instrument Sensitivity

In addition to equation (6.14), the only other thing necessary to arrive at the instrument sensitivity is the detectivity of the photometer electronics. This is essentially the same as the detectivity of the channel multiplier, since it is assumed that all of the output pulses of the channel multiplier are counted by the rest of the instrumentation system.

Because of the high speed and fast-overdrive-recovery of the electronics, compared to the rather low anticipated count rates, a phenomenon known as "dead-time" is not considered to be of any significance. Dead-time is the time interval following a pulse when the electronics is incapable of responding to a new pulse. The seriousness of this problem is related to the probability of a pulse occurring during the dead-time. If the count rate is low then the above-mentioned probability will be small. The problem of dead-time is common to all photon and particle counting electronics: "Some proportion of the events will not be counted, however low the mean count rate and however short the resolving time of the system. Accurate radiation measurement therefore depends on the use of detectors and systems capable of a far higher mean count rate than that under measurement" [*Herbst*, 1970].

The equation commonly used to correct for dead-time is [*Herbst*, 1970]

$$N_m = \frac{N_o}{1 - N_o \tau} \quad (6.15)$$

where N_m = "true" mean count rate
 N_o = observed count rate
 τ = dead-time

Suppose that the emission rate of the layer is 100 rayleighs and that equation (6.13) is an accurate expression for the input to the channel multiplier. Let ψ be 90° . Then the input to the channel multiplier is 76,400 photons per second. The channel multiplier in the serial number 1 photometer is serial number 203. Its detectivity is specified as 10.2%. Therefore the output pulse rate of the channel multiplier would be 7793 pulses per second. The dead-time of the electronics is determined primarily by the monostable multivibrator on the pulse processor board, and is approximately 90 ns. Solving equation (6.15) for N_o , and using 7793 as the true mean count rate and 90 ns as the dead time, N_o is found to be

$$\begin{aligned} N_o &= \frac{N_m}{1 + N_m \tau} \\ &= 7788 \\ &= 0.9993 N_m \end{aligned}$$

Therefore, as previously suggested, dead-time has an insignificant effect in this instrument.

The detectivity of the photometer electronics (including the channel multiplier) is then assumed to be essentially the same as the detectivity of the channel multiplier. Therefore, the sensitivity of the entire photometer may be expressed by the following equation:

$$I_o = P T_w T'_F T_L D_e$$

where I_o = instrument output in pulses per second

D_e = detectivity of the channel multiplier

P , T_w , T'_F , and T_L defined below equation (6.14)

Of course, what is really desired, is to observe an instrument output

count rate and be able from that to determine the layer emission rate (and from that determine the energetic electron flux). If we make use of equation (6.9), we may arrive at the following expression for the layer emission rate:

$$R = \frac{I_0 \sin \psi \csc^2 \frac{\theta}{2}}{\alpha T_w T_F' T_L D_e} \quad (6.16)$$

If we let $\psi = 90^\circ$, $\theta = 5^\circ$, $\alpha = 5.07 \text{ cm}^2$, $T_w = 0.83$, $T_F' = 0.106$, $T_L = 0.90$, and $D_e = 0.102$, then equation (6.16) simplifies to

$$\begin{aligned} R &= 12,835 I_0 \text{ (photons cm}^{-2} \text{ s}^{-1}\text{)} \\ &= 0.01284 I_0 \text{ (rayleighs)} \end{aligned}$$

which is valid only for $\psi = 90^\circ$ and for the value of T_F' which is presented for example only.

7. SUGGESTIONS FOR FUTURE WORK

This report has presented the design of a rocket-borne airglow photometer to measure the 391.4 nm emission of N_2^+ in the E region of the nighttime midlatitude ionosphere. From this measurement the energy flux of energetic electrons should be obtainable. Energetic electrons are believed to be a significant, and perhaps the principle, source of ionization in the nighttime E region at some midlatitude locations. As indicated in Chapter 6, the sensitivity of the instrument is inherently high and measurements of emission rates of less than one rayleigh are possible; the lower limit of the instrumentation system is determined by external factors: extraterrestrial light, other airglows, etc.

The problem of the measured emission being dependent upon vibrational and rotational temperatures deserves further attention. As shown in Chapters 2 and 6, the sensitivity of the instrument is dependent upon these temperatures. As far as reporting measured emission rates, an assumed temperature may be used but to properly arrive at energetic electron flux levels more information is needed. One possible solution would be to measure the temperature. This can be done by using two narrow-bandpass photometers: one used to measure the peak in the emission spectrum (see Figure 2.2) that occurs at approximately 391.4 nm, and the other one used to measure the peak in the emission spectrum that occurs at approximately 388.3 nm. The ratio of these two peaks, when the instruments are properly calibrated, can be used to measure the temperature.

As indicated in Chapter 6, ground-based measurements must take into consideration atmospheric absorption. During the first rocket

flight, the effects of atmospheric absorption and scattering between the earth's surface and the layer can be measured. This absorption and scattering data can then be up-dated by subsequent rocket flights to arrive at a realistic value. Having knowledge of the losses due to atmospheric absorption and scattering, ground-based measurements may prove to be useful for monitoring energetic electron flux and for indicating the state of the ionosphere (quiet, disturbed, etc.).

In this initial instrument both the optical filter temperature and instrument frame temperature are being monitored and telemetered to the ground receiving station. It may be that, during the calibration procedure, the detectivity of the photometer electronics will be found to be essentially independent of the frame temperature. If this results, then the frame temperature monitoring circuit can be eliminated. Or it may be found that the frame temperature is so well correlated with the optical filter temperature that the detectivity of the photometer-electronics can be calibrated as a function of the optical filter temperature, and again, the frame temperature monitoring circuit can be eliminated.

During the first flight, it may be discovered that the optical filter temperature does not change during the flight (a very desirable and anticipated result). If this is the result, then there will be no need to telemeter the filter temperature in future flights. All that will be necessary is to know the filter temperature just prior to the launch. It is also anticipated that the frame temperature will not change during the flight.

Having the proper center wavelength for the optical filter is very important. After some experience has been gained with the

instrument in actual launch operations, a good anticipated value for the actual operating temperature of the optical filter will be possible. Then, when optical filters are ordered after that, the optimum center wavelength can be specified at an accurate anticipated operating temperature.

The design of a rocket-borne 391.4 nm airglow photometer was undertaken to enhance the information on the role of energetic electrons in the midlatitude ionosphere. The successful completion of this experiment requires the calibration of the instrument, the launching of the rocket-borne instrument, and the analysis of the received data.

REFERENCES

- Bates, D. R. [1960], The airglow, *Physics of the Upper Atmosphere*, ed. J. A. Ratcliffe, Academic Press, New York, 219-260.
- Billings, B. H. [1971], Interference filter, optical, *McGraw-Hill Encyclopedia of Science and Technology*, 3rd ed., Vol. 7, McGraw-Hill Book Co., New York, 207-208.
- Chamberlain, J. W. [1961], *Physics of the Aurora and Airglow*, Academic Press, New York, 345-350.
- Degen, V. [1976], Generalized intensity formula for the N_2^+ first negative spectrum excited by electron impact, Geophys. Inst., unpublished, Univ. of Alaska.
- Geller, M. A., L. G. Smith and H. D. Voss [1975], Analysis of nighttime E-region winds and ionization production, *Radio Sci.* 10, 335-345.
- Gillet, F. C., W. F. Hugh, E. P. Ney and G. Cooper [1964], Photographic observations of the airglow layer, *J. Geophys. Res.* 69, 2827-2834.
- Glenn, J. H., Jr. and J. A. O'Keefe [1962], The Mercury-Atlas-6 space flight, *Science* 136, 1093-1099.
- Gray, D. E. [1957] (Ed.), *American Institute of Physics Handbook*, McGraw-Hill Book Co., New York, 6-45 to 6-50.
- Green, A. E. S. (ed.) and R. S. Stolarski [1966], Electron impact excitation of the ultraviolet, *The Middle Ultraviolet: Its Science and Technology*, John Wiley & Sons, Inc., New York, 165-176.
- Heavens, O. S. [1965], *Optical Properties of Thin Solid Films*, Dover Publications, Inc., New York, 227-238.
- Herbst, L. J. [1970] (Ed.), *Electronics for Nuclear Particle Analysis*, Oxford University Press, London, 5-6.
- Herzberg, G. [1950], *Molecular Spectra and Molecular Structure I. Spectra of Diatomic Molecules*, 2nd ed., D. Van Nostrand Co., Inc., Princeton, New Jersey, 466.

- Israelson, G. and J. R. Winckler [1975], Measurements of 3914 Å light production and electron scattering from electron beams artificially injected into the ionosphere, *J. Geophys. Res.* 80, 3709-3712.
- Krassovsky, V. I., N. N. Shefov and V. I. Yarin [1962], Atlas of the airglow spectrum 3000-12400 Å, *Planet Space Sci.* 9, 883-915.
- Lipson, S. G. and H. Lipson [1969], *Optical Physics*, Cambridge University Press, New York, 201-204.
- Macleod, H. A. [1969], *Thin-Film Optical Filters*, American Elsevier Publishing Co., New York, 88-96, 157-197, 306-307.
- Mitra, S. K. [1952], *The Upper Atmosphere*, 2nd ed., The Asiatic Society, Calcutta, India, 485-548.
- Muntz, E. P. [1962], Static temperature measurements in a flowing gas, *Phys. Fluids* 5, 80-90.
- O'Brien, B. J., F. R. Allum and H. C. Goldwire [1965], Rocket measurement of midlatitude airglow and particle precipitation, *J. Geophys. Res.* 70, 161-175.
- Packer, D. M. [1964], A manual on night airglow photometry, Sounding Rocket Research Techniques, *IQSY Instruction Manual No. 9*, IQSY Secretariat, London.
- Paulikas, G. A. [1975], Precipitation of particles at low and middle latitudes, *Rev. Geophys. Space Phys.* 13, 709, 734.
- Potemra, T. A. and A. J. Zmuda [1972], Nightglow evidence of precipitating energetic electrons in the midlatitude nighttime D region, *Radio Sci.* 7, 63-66.
- Rees, M. H. [1963], Auroral ionization and excitation by incident energetic electrons, *Planet. Space Sci.* 11, 1209-1218.
- Roach, F. E. [1964], The light of the night sky: astronomical, interplanetary and geophysical, *Space Sci. Rev.* 3, 512-540.

- Seward, F. D. [1973], The geographical distribution of ~ 100 keV electrons above the earth's atmosphere, *Rep. UCRL-51456*, Univ. of California, Lawrence Livermore Lab., Livermore.
- Smith, L. G., M. A. Geller and H. D. Voss [1974], Energetic electrons in the midlatitude nighttime *E* region, *J. Atmos. Terr. Phys.* 36, 1601-1612.
- Smith, L. G. and H. D. Voss [1976], Ionization by energetic electrons in the midlatitude nighttime *E* region, *Space Research XVII*, 427-432.
- Strobel, D. F., D. M. Hunten and M. B. McElroy [1970], Production and diffusion of nitric oxide, *J. Geophys. Res.* 75, 4310.
- Strobel, D. F., T. R. Young, R. R. Meier, T. P. Coffey and A. W. Ali [1974], The nighttime ionosphere: *E* region and lower *F* region, *J. Geophys. Res.* 79, 3171-3178.
- Swider, W. [1972], E-region model parameters, *J. Atmos. Terr. Phys.* 34, 1615-1626.
- Tohmatsu, T. [1970], The hydrogen and helium ultraviolet glow, its origins and aeronomical significance, *Space Research X*, 608-622.
- Voss, H. D. and L. G. Smith [1974], Design and calibration of a rocket-borne electron spectrometer for investigation of particle ionization in the nighttime midlatitude *E* region, *Aeron. Rep. No. 62*, Aeronomy Lab, Dept. of Elec. Eng., Univ. Ill., Urbana-Champaign.
- Weast, R. C. [1971] (Ed.), *Handbook of Chemistry and Physics*, 52nd ed., The Chemical Rubber Co., Cleveland, Ohio, E-94.
- Whitten, R. C. and I. G. Poppoff [1971], *Fundamentals of Aeronomy*, John Wiley & Sons, Inc., New York.
- Young, J. M., B. E. Troy, Jr., C. Y. Johnson and J. C. Holmes [1975], Ionizing nightglow: sources, intensity, and spatial distribution, *Radio Sci.* 10, 297-304.

APPENDIX I

NIKE APACHE PAYLOAD VIBRATION AND SHOCK TESTS

The following vibration levels are measured at the vibration table, upon which the payload is fastened in a vertical orientation.

1. Swept sinusoid vibration. Sweep-rate: 4 octaves per minute.

Axis	Frequency Range (Hz)	Level (g, 0-to-peak)	Duration (min.)
Thrust <i>z-z</i>	10-13	3.0	2.06
	13-120	3.0	
	120-300	7.0	
	300-400	10.0	
	400-2000	5.0	
Lateral <i>x-x</i> and <i>y-y</i>	7-11	0.40"DA	2.06/axis
	11-40	2.0 g	
	40-120	0.024"DA	
	120-2000	5.0 g	

DA = Double Amplitude

$g = 0.0514 F^2 DA$, F in Hz, DA in inches

2. Random vibration.

Axis	Frequency Range (Hz)	Test Duration (sec)	PSD Level (g^2/Hz)	Accel. (g-rms)
Thrust <i>z-z</i>	20-2000	10	0.20	20.0
Lateral <i>x-x</i> and <i>y-y</i>	20-2000	10	0.20	20.0

PSD = Power Spectral Density, in g^2/Hz

Accel. = $\sqrt{PSD \times FBW}$ = Acceleration, in g-rms

FBW = Frequency Bandwidth = 2000-20 = 1980 Hz

3. Ignition transient.

36 g at 136 Hz

APPENDIX II
COMPUTER PROGRAMS

The programs in APPENDICES II.1 and II.2 are written in the programming language BASIC, and were specifically written for use on a Hewlett-Packard model 9830A calculator connected to an hp 9866A printer and an hp 9862A calculator plotter.

The program in APPENDIX II.3 was written by Rudolph Fillinger, in FORTRAN IV, G level, and contains the function subprograms DCADRE and DSQUAN. DCADRE is a program of International Mathematical and Statistical Libraries, Inc. (IMSL), Houston, Texas. DSQUAN is a program in the Local Fortran Library of the Computing Services Office of the University of Illinois (FORTUOI), Urbana-Champaign.

APPENDIX II.1

FOLDING OF GAUSSIAN-WINDOW FILTERS WITH
DISCRETE LINE SPECTRUM

```
2 REM      GRAPH LABELING PROGRAM FOR
4 REM      GAUSSIAN-SHAPED FILTER TRANSMISSION
6 REM      FUNCTIONS FOLDED WITH THE 1000K
8 REM      DISCRETE LINE SPECTRUM
10 SCALE 3872,3924,-0.15,1.225
20 XAXIS 0,10,3880,3920
30 YAXIS 3880,0.1,0,1
40 FOR L=3880 TO 3920 STEP 10
50 PLOT L,0,1
60 LABEL (*,1.2,2,0,0.8)
70 CPLOT -2.8,-1.3
80 LABEL (*,1.2,2,0,0.8)L
100 NEXT L
110 FOR J=0.1 TO 1 STEP 0.1
120 PLOT 3880,J,1
130 LABEL (170,1,2,0,0.8)
140 CPLOT -6,0.5
150 LABEL (170,1,2,0,0.8)J
170 FORMAT 2F4.1
180 NEXT J
190 PLOT 3876,0.5,1
195 LABEL (*,1.2,2,0,0.8)
200 CPLOT 0,-9
210 LABEL (*,1.5,2,PI/2,0.8)"FILTER OUTPUT / FILTER INPUT"
220 PLOT 3900,0,1
230 CPLOT -5,12
240 LABEL (*,1.5,2,0)"FILTER CENTER-WAVELENGTH, IN ANGSTROMS"
250 PLOT 3897,1,1
260 CPLOT -22,2
270 LABEL (*)"FILTER INPUT IS INCIDENT EMISSION IN 3914A BAND, 1000K"
280 PLOT 3900,1,1
290 CPLOT -15,1
300 LABEL (*)"FILTER PEAK TRANSMITTANCE = 1.0"
310 PLOT 3900,1,1
320 CPLOT -19,0
330 LABEL (*)"V=5A HALF-PEAK-TRANSMITTANCE BANDWIDTH"
340 PLOT 3900,1,1
350 CPLOT -13,-1
360 LABEL (*)"W=10A, X=20A, Y=30A, Z=40A"
370 PLOT 3900,1,1
380 CPLOT -26,-2
390 LABEL (*)"FILTER TRANSMITTANCE VS. WAVELENGTH ASSUMED GAUSSIAN"
400 END
```

```

2 REM      PROGRAM FOR FOLDING GAUSSIAN-SHAPED FILTER
4 REM      TRANSMISSION FUNCTIONS WITH THE 1000K
6 REM      DISCRETE LINE SPECTRUM AND
8 REM      PLOTTING THE RESULTS
10 SCALE 3872,3924,-0.15,1.225
20 DIM AS[149,2],BS[149,2],CS[149,2],DS[149,2]
30 LOAD DATA 5,A
40 LOAD DATA 6,B
50 LOAD DATA 7,C
60 LOAD DATA 8,D
61 FOR I=1 TO 5
62 GOTO 350
63 REM      I DETERMINES THE VALUE OF N,
64 REM      WHICH DETERMINES THE BANDWIDTH OF THE FILTER
65 PLOT 3880,0.2,1
70 FOR C=3880 TO 3920 STEP 0.5
75 REM      C IS THE CENTER WAVELENGTH OF THE FILTER
80 M=0
90 FOR J=1 TO 4
100 FOR K=1 TO 149
110 IF J=1 THEN 150
120 IF J=2 THEN 170
130 IF J=3 THEN 190
140 IF J=4 THEN 210
150 W=A[K,1]
155 X=A[K,2]
160 GOTO 220
170 W=B[K,1]
175 X=B[K,2]
180 GOTO 220
190 W=C[K,1]
195 X=C[K,2]
200 GOTO 220
210 W=D[K,1]
215 X=D[K,2]
217 REM      F IS THE FILTER TRANSMITTANCE AT WAVELENGTH W
220 E=((W-C)/N)^2
230 G=-0.5*E
235 IF G<-195 THEN 260
240 F=EXP(G)
242 REM      X IS THE RELATIVE PROBABILITY OF A PHOTON
243 REM      AT WAVELENGTH W
245 M1=F*X
247 REM      M1 IS THE RELATIVE PROBABILITY OF A PHOTON
249 REM      AT THE OUTPUT OF THE FILTER AT WAVELENGTH W
250 M=M+M1
255 REM      M IS THE TOTAL RELATIVE PROBABILITY OF A PHOTON
257 REM      AT THE OUTPUT OF THE FILTER
260 NEXT K
270 NEXT J
280 M2=M/0.211408504
285 REM      M2 IS NORMALIZED TO A TOTAL INPUT
287 REM      PROBABILITY OF 1
288 REM      I.E. THE TOTAL RELATIVE PROBABILITY OF A PHOTON
289 REM      OCCURRING IN THE SPECTRUM IS 0.211408504

```

```
290 PRINT C,M2
300 PLOT C,M2,2
310 PEN
320 NEXT C
325 NEXT I
330 GOTO 490
350 IF I=1 THEN 390
360 IF I=2 THEN 410
370 IF I=3 THEN 430
372 IF I=4 THEN 450
376 IF I=5 THEN 470
390 N=2.12
400 GOTO 65
410 N=4.25
420 GOTO 65
430 N=8.49
440 GOTO 65
450 N=12.74
460 GOTO 65
470 N=16.99
480 GOTO 65
490 END
```

APPENDIX II.2

FOLDING OF FILTER TRANSMISSION FUNCTIONS WITH DISCRETE
LINE SPECTRUM AT VARIOUS TEMPERATURES

```

10 REM      THIS PROGRAM LABELS THE GRAPH
20 REM      FOR THE CONVOLUTION OF EQUATION (6.12)
30 REM      WITH THE DISCRETE LINE SPECTRA
40 SCALE 3907,3927,-0.03,0.245
50 XAXIS 0,1,3910,3925
60 YAXIS 3910,0.01,0,0.2
70 FOR L=3910 TO 3925 STEP 5
80 PLOT L,0,1
90 LABEL (*,1.2,2,0,0.8)
100 CPLOT -2.8,-1.3
110 LABEL (*,1.2,2,0,0.8)L
120 NEXT L
130 FOR J=0.1 TO 0.2 STEP 0.1
140 PLOT 3910,J,1
150 LABEL (170,1,2,0,0.8)
160 CPLOT -6,0.5
170 LABEL (170,1,2,0,0.8)J
180 FORMAT 2F4.1
190 NEXT J
200 END

```

ORIGINAL PAGE IS
OF POOR QUALITY

```

10 REM      THIS PROGRAM PRODUCES THE CURVES
20 REM      SHOWN IN FIGURE 6.8, AND IS SPECIFICALLY FOR
30 REM      EQUATION (6.12). BY CHANGING THE
40 REM      EQUATIONS IN STATEMENTS 250 THROUGH 300
50 REM      THE PROGRAM MAY BE USED FOR OTHER
60 REM      FILTER TRANSMISSION FUNCTIONS.
62 SCALE 3907,3927,-0.03,0.245
64 DIM AS[149,2],BS[149,2],CS[149,2],DS[149,2]
66 REM      H SELECTS THE TEMPERATURE OF
68 REM      THE NITROGEN. H=1 IS 200K, H=2 IS 300K,
70 REM      . . . H=6 IS 5000K.
72 FOR H=1 TO 6
74 IF H=1 THEN 415
76 IF H=2 THEN 460
78 IF H=3 THEN 520
80 IF H=4 THEN 571
82 IF H=5 THEN 580
84 IF H=6 THEN 680
85 PLOT 3910,0.1,1
86 REM      C DETERMINES THE FILTER CENTER WAVELENGTH
88 FOR C=3910 TO 3925 STEP 1
90 N=C-3910
94 M=0
96 REM      J DETERMINES THE DATA MATRIX
98 FOR J=1 TO 4
100 REM      K STEPS THROUGH THE 149 DATA-PAIRS IN EACH MATRIX
110 FOR K=1 TO 149
115 IF J=1 THEN 150
120 IF J=2 THEN 170
125 IF J=3 THEN 190
130 IF J=4 THEN 210

```

```
135 REM      W IS THE WAVELENGTH
140 REM      X IS THE PROBABILITY OF OCCURANCE
150 W=A[K,1]
155 X=A[K,2]
160 GOTO 250
170 W=B[K,1]
175 X=B[K,2]
180 GOTO 250
190 W=C[K,1]
195 X=C[K,2]
200 GOTO 250
210 W=D[K,1]
215 X=D[K,2]
220 REM      STATEMENTS 250 TRHOUGH 300 CALCULATE
230 REM      THE FILTER TRANSMITTANCE
250 E=((W-3909.8-N)/6.65)^2
260 G=-0.5*E
265 REM      STATEMENTS 270, 293, 297, AND 300
267 REM      PREVENT UNDERFLOW ERROR.
270 IF G<-195 THEN 335
272 F=0.191*EXP(G)
291 E1=((W-3923.4-N)/10)^2
292 G1=-0.5*E1
293 IF G1<-195 THEN 345
294 F1=0.02*EXP(G1)
295 E2=((W-3890.4-N)/8)^2
296 G2=-0.5*E2
297 IF G2<-195 THEN 355
298 F2=0.01*EXP(G2)
300 IF (F+F1+F2)<10^(-55) THEN 772
302 M1=X*(F+F1+F2)
304 REM      M IS THE RUNNING TOTAL FOR ALL
305 REM      DATA AT A GIVEN TEMPERATURE.
307 M=M+M1
310 NEXT K
315 NEXT J
317 REM      STATEMENT 320 NORMALIZES TO AN INPUT
318 REM      PROBABILITY OF 1.
320 M2=M/S
325 REM      M2 IS THE PROBABILITY OF AN
326 REM      OUTPUT PHOTON.
328 PRINT C,M2
329 PLOT C,M2,2
330 PEN
331 NEXT C
332 NEXT H
333 GOTO 780
335 F=0
340 GOTO 291
345 F1=0
350 GOTO 295
355 F2=0
360 GOTO 300
```

```
390 REM      STATEMENTS 415 THROUGH 430 LOADS
400 REM      THE 200K DATA.
415 LOAD DATA 13,A
420 LOAD DATA 14,B
425 LOAD DATA 15,C
430 LOAD DATA 16,D
432 REM      STATEMENTS 438 THROUGH 447 DETERMINES THE
434 REM      TOTAL PROBABILITY OF AN INPUT PHOTON
435 REM      AT 200K, TO PROPERLY NORMALIZE
436 REM      FOLLOWING CALCULATIONS.
438 S=0
440 FOR I=1 TO 149
442 S1=A[I,2]+B[I,2]+C[I,2]+D[I,2]
445 S=S+S1
447 NEXT I
450 GOTO 85
460 LOAD DATA 33,A
470 LOAD DATA 34,B
480 LOAD DATA 35,C
490 LOAD DATA 36,D
500 S=0.216312498
510 GOTO 85
520 LOAD DATA 45,A
530 LOAD DATA 46,B
540 LOAD DATA 47,C
550 LOAD DATA 48,D
560 S=0.21596545
570 GOTO 85
571 LOAD DATA 5,A
572 LOAD DATA 6,B
573 LOAD DATA 7,C
574 LOAD DATA 4,D
575 S=0.211408504
576 GOTO 85
580 LOAD DATA 61,A
590 LOAD DATA 62,B
600 LOAD DATA 9,C
610 LOAD DATA 52,D
620 S=0
630 FOR Q=1 TO 149
640 S1=A[Q,2]+B[Q,2]+C[Q,2]+D[Q,2]
650 S=S+S1
660 NEXT Q
670 GOTO 85
680 LOAD DATA 50,A
690 LOAD DATA 49,B
700 LOAD DATA 10,C
710 LOAD DATA 11,D
720 S=0
730 FOR R=1 TO 149
740 S1=A[R,2]+B[R,2]+C[R,2]+D[R,2]
750 S=S+S1
760 NEXT R
```

ORIGINAL PAGE IS
OF POOR QUALITY

```
770 GOTO 85  
772 M1=0  
773 GOTO 307  
780 END
```

APPENDIX II.3

ANALYSIS OF INCIDENT RADIATION DEPENDENCE
UPON ANGLE WITH RESPECT TO ZENITH

C THIS PROGRAM IS DESIGNED TO INTEGRATE A FUNCTION
 C F(X,Y), WHERE THE FUNCTION F(X,Y) IS TO BE SPECIFIED. IN THIS
 C PARTICULAR CASE THE FUNCTION F(X,Y) HAS BEEN SPECIFIED BY
 C L. D. PAARMANN. THE PROGRAM CONSISTS OF A MAIN PROGRAM AND
 C TWO FUNCTION SUBPROGRAMS (IE. FOUTR AND FINNR). THE INTEGRATION
 C IS PERFORMED IN TWO STEPS BY THE FUNCTION SUBPROGRAMS DCADRE
 C AND DSQUAN (IMSL, 1975; FORTUOI, 1976). THE OUTER OR SECOND
 C INTEGRATION IS PERFORMED BY DCADRE, WHICH UTILIZES
 C THE FUNCTION SUBPROGRAM FOUTR. FOUTR IS A FUNCTION SUBPROGRAM
 C WHICH PERFORMS THE INNER OR FIRST INTEGRATION. FOUTR
 C UTILIZES THE FUNCTION SUBPROGRAM FINNR.
 C FINNR IS A FUNCTION SUBPROGRAM WHICH CONTAINS THE ACTUAL
 C ANALYTICAL EXPRESSION FOR F(X,Y).
 C
 C

```

      IMPLICIT REAL*8(A-H,O-Z)
      EXTERNAL FOUTR
      REAL*8 LOWER
      COMMON H, THETA, PSI, YVAL, DPRI, UPPER, A
      NAMELIST/PRAMS/THETA,PSI
      AERR=1.0D-04
      RERR=1.0D-04
      READ(5,PRAMS)
      WRITE(6,80)THETA, PSI
80    FORMAT(' ', 'THETA=', F10.8, ' INTIAL PSI=', F10.8)
      DO 600 N=1,13
      PSI=PSI-0.10D0
      H=25.0D0
      DO 600 L=1,5
      H=H+25.0D0
      DPRI=H/DSIN(PSI)
      UPPER=DPRI*DTAN(THETA)
      LOWER=-UPPER
      ANS=DCADRE(FOUTR, LOWER, UPPER, AERR, RERR, ERROR, IER)
      ANS=ANS*5.07D06/(25.13274123D0*DPRI)
      WRITE(6,100)
100   FORMAT(1X, 'PRAMETERS:  H,THETA,PSI')
      WRITE(6,101)H, THETA, PSI
101   FORMAT(3(5X, D20.5))
      WRITE(6,102)UPPER, LOWER, AERR, ERROR, IER
102   FORMAT(1H0, 'LIMITS:  ', 2D20.5, 5X, 'ERROR:  ', 2D20.5, 5X, 'IER=', I10)
      WRITE(6,103) ANS
103   FORMAT(1H0, 'ANSWER=', D20.8)
600   CONTINUE
      STOP
      END
  
```

ORIGINAL PAGE IS
OF POOR QUALITY

```

FUNCTION FOUTR(Y)
IMPLICIT REAL*8(A-H,O-Z)
EXTERNAL FINNR
REAL*8 LOW
COMMON H, THETA, PSI, YVAL, DPRI, UPPER, A
AER=1.0D-04
YVAL=Y
CHI=PSI-THETA
A=DPRI*DTAN(THETA)*DSIN(PSI)*(1.0D0+DCOTAN(PSI)/DTAN(CHI))
E=DPRI*DSIN(THETA)/DSIN(THETA+PSI)
G=(A+E)/2.0D0
UP=G/UPPER*DSQRT(UPPER*UPPER-Y*Y)
LOW=-UP
IF(LOW.EQ.UP)GO TO 46
FOUTR=DSQUAN(LOW,UP,AER,FIFTH,RUM,NO,FINNR)
RETURN
46 FOUTR=0.0D0
RETURN
END

```

```

FUNCTION FINNR(X)
IMPLICIT REAL*8(A-H,O-Z)
REAL*8 NUM
COMMON H, THETA, PSI, YVAL, DPRI, UPPER, A
APRI=DPRI*DSIN(THETA)/DSIN(THETA+PSI)
DUP=H*DCOTAN(PSI)
NUM=DPRI*DPRI+DUP*DUP+2.0D0*DUP*X+H*H
DEM=DSQRT((DUP*DUP+2.0D0*DUP*X+X*X+YVAL*YVAL+H*H)**3)
FINNR=NUM/DEM
RETURN
END

```